

# Robust Soft-Matter Robotic Materials

Eric J. Markvicka

July 12, 2018

CMU-RI-TR-18-38

The Robotics Institute  
Carnegie Mellon University  
Pittsburgh, PA 15213

**Thesis Committee:**

Professor Carmel Majidi, Chair  
Professor Chris Atkeson  
Professor Scott Hudson  
Professor Metin Sitti, Max Planck Institute

*Submitted in partial fulfillment of the requirements  
for the degree of Doctor of Philosophy.*

Copyright © 2018 by Eric Markvicka



# *Abstract*

Emerging applications in wearable computing, human-machine interaction, and soft robotics will increasingly rely on new soft-matter technologies. These soft-matter technologies are considered *inherently safe* as they are primarily composed of *intrinsically soft materials*—elastomers, gels, and fluids. These materials provide a method for creating soft-matter counterparts to traditionally rigid devices that exhibit the mechanical compliance and versatility of natural, biological systems. However, these soft-matter counterparts often rely on power and data communication tethers, limiting their use outside of a controlled laboratory environment. Furthermore, these soft-matter counterparts are increasingly susceptible (as compared to their rigid counterparts) to varying forms of mechanical damage such as cutting, tearing, or puncture that can result in operational failure. This thesis presents two new rapid (<3 hrs) fabrication methods that addresses current challenges of integrating surface mount microelectronics for signal processing, wireless communication, and power with soft and stretchable circuit interconnects. In addition, a new material architecture is introduced for creating soft and highly deformable circuit interconnects that are capable of autonomous electrical self-healing to maintain electrical functionality when damage occurs. Finally, this material architecture can be used as an artificial nervous tissue to electrically detect, localize, and respond to detrimental damage events within soft-matter inflatable structures and robotic systems.

To enable soft-matter technologies to be useful outside of a controlled laboratory environment, the necessary circuit components for signal processing, wireless communication, and power must be integrated. Systems integration raises unique challenges in materials compatibility, multi-scale fabrication, and electrical and mechanical interfacing. Here, a unifying, deterministic adhesive transfer approach was developed, enabling precision multi-layer assembly of conductive and insulating thin films with surface mount integrated circuits (Chapter 2). This method was demonstrated by fabricating two highly customizable wearable devices that directly adhere to the skin. In addition, an anisotropic, Z-axis conductive film was developed for interfacing liquid-phase interconnects with surface mount components (Chapter 3).

A major obstacle to the adaption of soft-matter technologies in more complex, natural environments outside laboratories is their fragility. Whereas natural biological tissue can quickly detect and adapt to injuries, current soft-matter technologies often cannot circumvent even minor damage. Here, we introduce a material architecture and framework for creating soft, stretchable circuit interconnects that are electrically stable under typical operational loading conditions but capable of instantaneous electrical self-healing under multiple, extreme damage events (Chapter 4). Circuits produced with this hybrid composite remain fully and continuously operational even when the traces are severed, torn, punctured, or the material is completely removed.

The ability of biological organisms to autonomously detect, communicate, and respond to damage of soft tissue presents an intriguing opportunity for compliant, engineered systems. Here, an artificial nervous tissue has been developed for detecting and localizing mechanical damage events (Chapter 5). When coupled with computation, communication, and actuation, this soft and highly deformable biomimetic composite

presents new opportunities to autonomously identify damage, calculate severity, and respond to prevent failure within robotic systems.

# *Acknowledgments*

I would like to thank my advisor Prof. Carmel Majidi from whom I have learned a tremendous amount of knowledge on this journey to obtaining a Ph.D. and becoming a faculty member myself. Thank you for your never ending support, scientific freedom and guidance, selfless availability, and encouragement to find scientific depth within my work. It has been a great pleasure to work with you over the last four years! Thank you for all your help!

I would like to express my gratitude to my thesis committee, Prof. Chris Atkeson, Prof. Scott Hudson, and Prof. Metin Sitti. Thank you for your perspective and guidance.

It has been a great pleasure to belong to the Soft Machines Lab (SML). Thank you to both past and present members for your support, countless discussions, and last minute help with projects. I will greatly miss the lab lunches at Sichuan Gourmet, Chinese hot pot, and Korean BBQ. Xiaonan Huang thank you for generously hosting! I would like to thank the brave souls (Dr. Navid Kazem, Steven Rich, Tess Hellebrekers, Houriyeh Majditehran, Yunsik Ohm, and Daniel Green) who sacrificed their footwear, socks, and bare feet for LMEE! Thank you to the many co-authors over the last four years including Prof. Carmel Majidi, Prof. Michael Bartlett, Dr. Andrew Fassler, Dr. Tong Lu, Dr. Navid Kazem, Dr. Kitty Kumar, Steven Rich, Xiaonan Huang, Chengfeng Pan, Jiahe Liao, Hesham Zaini, and Yichu Jin. Without you this work would have not been possible. Finally, I would like to thank Prof. Michael Bartlett who made major contributions to the research in this thesis. It was a great privilege to work with you during my first two years of graduate school. You are truly a great mentor and friend! Stacie and I both greatly miss spending time with the Bartlett's! Pittsburgh has not been the same.

I would like to thank Prof. Shane Farritor (University of Nebraska—Lincoln). Undergraduate research was a life-changing experience. Thank you for inspiring me to pursue graduate school.

I am also grateful for the many friends who have made our time in Pittsburgh more enjoyable, including Joe and Katie; Nate and Caitlin; James and Chelsea; and Luke and Samantha. Thank you!

I cannot express sufficient gratitude to my parents, Roy and Sandy, for their endless love, support, and advice. I could not have achieved this without your help and many sacrifices that you have made. Thank you for encouraging me to pursue my dreams. I am forever grateful. I thank my siblings, Kyle and Jesi, for their support, patience, and encouragement. Thank you for the many distractions to allow my mind wander and help me recharge. I thank my Grandparents, for their constant encouragement and support. I also want to thank Stacie's family for their support and encouragement.

Lastly, I would like thank my wife Stacie, for your never ending love, encouragement, and support on this journey. Thank you for the many sacrifices you have made to allow me to pursue my dreams including putting your own career and dreams on hold. This would have not been possible without your unwavering strength and support! I am forever grateful. Thank you for your patience and understanding throughout this journey and belief that we would "eventually" be moving back home. I'm greatly saddened to be leaving the Steel City but beyond excited to start the next journey!



## *Funding*

This thesis contains work supported by National Science Foundation Graduate Research Fellowship; Center for Machine Learning and Health Fellowship; NASA Early Career Faculty Award (NNX14AO49G; Research Collaborator: Dr. Bill Bluethmann); AFOSR Multidisciplinary University Research Initiative (FA95501810566; Program Manager: Dr. Ken Goretta); and Disruptive Health Technology Institute Award. Sensor and mechanical characterization was performed on equipment supported through an Office of Naval Research (ONR) Defense University Research Instrumentation Program (DURIP) (N00014140778; Bioinspired Autonomous Systems; PM: Dr. Tom McKenna).



# Contents

1	<i>Introduction</i>	17
1.1	<i>Stretchable electronic circuits</i>	19
1.2	<i>Electrically self-healing soft-matter robotics and electronics</i>	20
1.3	<i>Damage sensing soft-matter composite</i>	21
1.4	<i>Contributions of this Thesis</i>	22
1.5	<i>Dissertation Structure</i>	25
2	<i>Precision Assembly of Multi-Layer Stretchable Electronic Circuits</i>	27
2.1	<i>Background</i>	27
2.2	<i>Fabrication Methodology</i>	29
2.3	<i>Soft Transfer Printing Characterization</i>	30
2.4	<i>Soft Sensor Characterization</i>	32
2.5	<i>Integrated Sensor Skin Experiments</i>	33
2.6	<i>Skin Mountable Pulse Oximeter Device Experiments</i>	35
2.7	<i>STEAM Outreach</i>	37
2.8	<i>Outlook</i>	37
3	<i>Stretchable Electronic Circuits with Liquid Metal Interconnects</i>	39
3.1	<i>Background</i>	40
3.2	<i>Fabrication Methodology</i>	40
3.3	<i>Discussion</i>	45
3.4	<i>Outlook</i>	48

4	<i>Autonomously Self-Healing Soft-Matter Electronics and Robotics</i>	51
4.1	<i>Background</i>	51
4.2	<i>Fabrication Methodology</i>	52
4.3	<i>Liquid Metal-Elastomer Composite</i>	54
4.4	<i>Trace Patterning</i>	55
4.5	<i>Electromechanical Characterization</i>	55
4.6	<i>Material Encapsulation</i>	57
4.7	<i>Damage Response</i>	58
4.8	<i>Soft Robotics Demonstration</i>	60
4.9	<i>Outlook</i>	61
5	<i>Damage Sensing Soft-Matter Composite</i>	63
5.1	<i>Background</i>	63
5.2	<i>Fabrication Methodology</i>	65
5.3	<i>Mechanical Characterization</i>	66
5.4	<i>Formation of Electrical Networks</i>	67
5.5	<i>Integration with Host Substrates</i>	68
5.6	<i>Detection and Localization of Damage</i>	69
5.7	<i>Ballistic Puncture</i>	72
5.8	<i>Soft Robotics Demonstration</i>	72
5.9	<i>Outlook</i>	73
6	<i>Conclusion and Future Outlook</i>	75
6.1	<i>Closing Remarks</i>	75
6.2	<i>Future Outlook</i>	77
6.2.1	<i>Clinical Translation</i>	77
6.2.2	<i>Robotics Translation</i>	79
6.2.3	<i>Next Generation Materials</i>	80

7	<i>Appendix</i>	101	
7.1	<i>Experimental: Precision Assembly of Multi-Layer Stretchable Electronic Circuits</i>	101	101
7.2	<i>Experimental: Stretchable Electronics with Liquid Metal Interconnects</i>	107	
7.3	<i>Experimental: Autonomously Self-Healing Soft-Matter Electronics</i>	111	
7.4	<i>Experimental: Damage Sensing Soft-Matter Composite</i>	117	



## List of Figures

1.1	Young's modulus of biological tissue and common materials	17
1.2	Original flex circuit patten (British Patent 4,681, issued 1903)	18
1.3	Flex circuit assembly of circa 1991 Olympus MJU I Infinity Stylus $\mu$	18
1.4	Stretchable electronic circuits	23
1.5	Self healing soft matter composite	24
1.6	SEM image of coated/patterned and uncoated/unablated zPDMS	24
1.7	Future outlook	25
2.1	Illustration of stretchable electronics assembly	29
2.2	CO <sub>2</sub> Laser alignment system	30
2.3	Deterministic adhesive transfer characterization	31
2.4	CO <sub>2</sub> laser impingement	32
2.5	Soft strain sensor characterization	33
2.6	Wearable integrated sensing skin	34
2.7	Wearable pulse oximeter and characterization	36
2.8	Illustration of STEAM workshop on wearable computing	37
3.1	Liquid-metal soft-matter electronics	41
3.2	Fabrication process with UV laser micromachining	42
3.3	Samples of UV laser-patterned EGaIn features	43
3.4	SEM image of coated/patterned and uncoated/unablated zPDMS	44
3.5	UV laser micromachined planar components	45
3.6	Cross section photographs of zPDMS	46
3.7	Soft-matter printed circuit board	47
4.1	Self healing soft matter composite	53
4.2	Schematic of damage mitigation strategies	54
4.3	Self-healing of close-neighboring traces	54
4.4	Particle size analysis of LMEE composite	55
4.5	LMEE trace dimensions	55
4.6	Electrical and mechanical strain limits	56
4.7	Extended cyclic loading up to 1 million cycles	56
4.8	Electrical and mechanical characterization	57
4.9	Activation pressure as a function of composite thickness	58

4.10 Autonomous self-healing response	59
4.11 Autonomously self-healing soft robot	60
5.1 Response to mechanical damage	64
5.2 Active detection of damage (fracture)	65
5.3 Mechanical and electrical characterization	66
5.4 Active detection of damage (knife)	67
5.5 Stress-strain of coated fabric	67
5.6 Damage detection substrate versatility	68
5.7 Damage detection and 2D localization	69
5.8 Bounds of damage detection and localization	70
5.9 Detection and localization of ballistic puncture	71
5.10 Illustration of an inflatable humanoid structure	72
5.11 Autonomous damage detection for pressure regulation	73
5.12 Change in pressure of the inflatable humanoid structure	74
6.1 Soft-matter wearable pulse oximeter	75
6.2 Electrically self-healing soft-matter electronics	76
6.3 Damage sensing soft-matter electronics	77
6.4 Illustration of personalized medical monitoring	78
6.5 Algorithms for general-purpose physiological monitoring	78
6.6 Wireless multi-modal tactile sensor	80
6.7 Soft robot capable of mechanically and electrically self-healing	81
7.1 Configuration of the interdigitated capacitor	109
7.2 Soft-matter printed circuit board schematic	109
7.3 Scoring Stylus mounted in X-Y plotter	111
7.4 Single lap shear	113
7.5 Abrasive shear force	113
7.6 Spherical indenter with tangential shear force	114
7.7 Soft robot construction	115
7.8 Particle analysis of LM-elastomer composites	119
7.9 Particle analysis histograms	119
7.10 Applied compressive force and resistance as a function of time	120
7.11 Photograph of the projectile exit.	120
7.12 Soft robot mimic construction	120
7.13 Damage detection and localization in 1D	121

## *List of Tables*

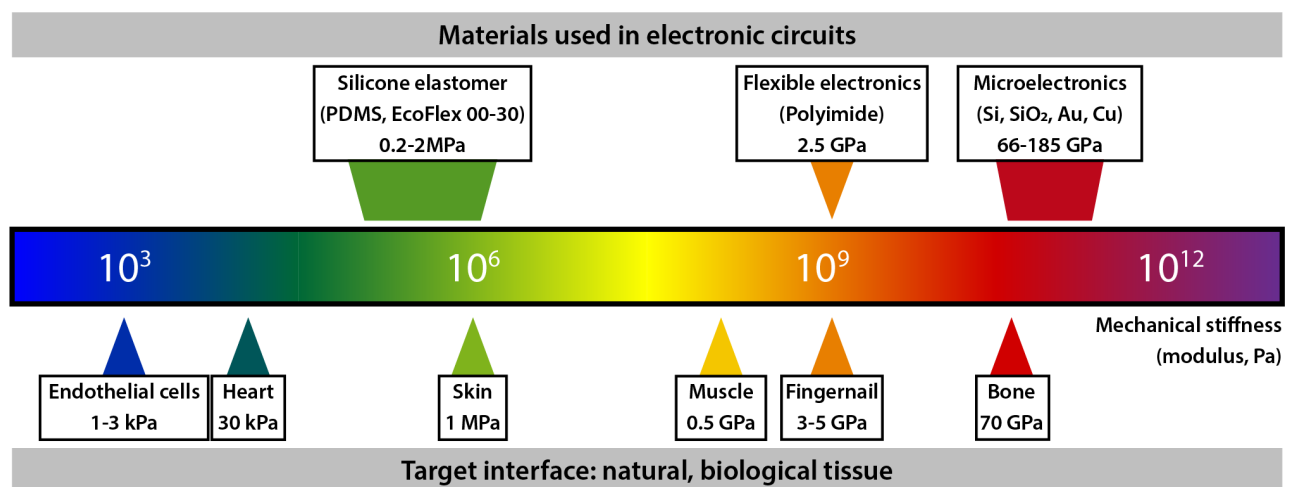
7.1	CO <sub>2</sub> fabrication conditions	102
7.2	UV fabrication conditions	104



# 1

## Introduction

In modern life, electronic circuits—individual electronic components connected by conductive traces—are ubiquitous. Electronic circuits are central to many of the devices we interact with and are responsible for providing *electric power* for lighting, to run electric motors, or recharge batteries; to *generate heat* for cooking, to melt materials, or to warm buildings; to *monitor conditions* for an alarm system, data storage, or health monitoring; or to *generate signals* for wired/wireless communication or to run electric cars, robots, or machines. These traditional electronics and machines are typically composed of intrinsically rigid and brittle materials that have limited deformability or resistance to bending, stretching, and impact loading. In contrast, the human body is composed of natural, biological tissue that is soft and highly deformable. Consequently, devices composed of traditional, rigid materials have limited interactions with humans (Figure 1.1). Conventional



robots and machines are primarily found in factories, surrounded by barriers to limit/prevent interactions with humans. Whereas, wearable

Figure 1.1: Young's modulus (stiffness) of natural, biological tissue and commonly used materials for commercially available wearable devices and methods proposed within this dissertation.

electronics (e.g. smart watch/band) are confined to areas of low movement/flexibility that do not interfere with the dynamic motion of the human body<sup>[38]</sup>. Devices that overcome this fundamental mismatch in mechanical compliance will enable applications that are impossible to achieve with the rigid, boxy, and bulky devices that exist today.

Interestingly, many industries have been using soft and flexible materials for decades. Flexible circuits—flat, flexible metal conductors patterned on a thin, pliable dielectric substrate—were envisioned at the turn of the 20th century. The invention was first patented in 1903 by Albert Hanson (British Patent 4,681), who clearly described the multilayer, through hole circuit architecture that is prevalent throughout the electronics industry today<sup>[42]</sup> (Figure 1.2). Hanson also realized that to build the most practical and versatile circuit wiring it was critical that the circuit was composed of materials that were soft and flexible, allowing the circuit wiring to conform to a desired shape or to flex or bend during use. Flexible circuitry provides many benefits over traditional rigid printed circuit boards or wiring including weight, size, and cost resulting in greater design freedom and higher circuit-density and has enabled a vast number of industries including transportation, computers, space exploration, and the Internet. While this technology is used in most electronic goods, it is almost completely *invisible*. These fragile and vulnerable circuits (as compared to their rigid counterparts) are routed within hinges or hidden deep inside hard case packaging to prevent external interactions, a likely cause for damage and ultimately failure (Figure 1.3).

In this dissertation, we work towards removing the hard case and developing soft machines and electronics that exhibit the extraordinary robustness of soft materials that is currently only found within nature. These soft machines and electronics are considered inherently safe for contact with the human body, as they are primarily composed of intrinsically soft materials—elastomers, gels, and fluids. These materials provide a method for creating soft-matter counterparts of existing traditionally rigid machines and enable intimate interactions with the human body that were previously not possible. We introduce a new material architecture for soft and highly deformable circuit interconnects that exhibits uncompromising resilience to mechanical damage without manual intervention. Finally, this new material architecture can be used to detect and electrically self-report damage. The ability of soft materials to withstand general wear and tear and to autonomously (without human intervention) adapt, sense, and respond to detrimental damage events will be critical for commercialization and life outside of hard case packaging or a controlled laboratory environment.

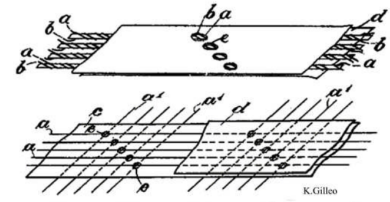


Figure 1.2: Original flex circuit pattern filled 1902, issued 1903 (British Patent 4,681). Image illustrates the multilayer, through hole circuit architecture that is prevalent throughout the electronics industry today. Image adapted from<sup>[42]</sup>.



Figure 1.3: Olympus MJU I Infinity Stylus  $\mu$  (A) Popular circa 1991 fully automatic compact camera made by Olympus. (B) Rigid exterior (hard case) is removed to expose the flexible circuit assembly that is wrapped around the camera body.

### 1.1 Stretchable electronic circuits

Recent advances in mechanics and materials have made it possible to produce soft and deformable electronic circuits that exhibit the electrical properties of conventional, rigid printed circuit boards but match the mechanical properties of soft, natural biological tissue<sup>[49,162,174]</sup>. Efforts to create soft and deformable (stretchable) circuits began in the mid-1990s and include so-called “deterministic architectures” in which mechanical compliance is introduced through geometry – e.g. PANI or Ag-Ni alloy coated on a woven fabric<sup>[48,31,117,76]</sup>, thin metal interconnects with serpentine<sup>[70,71]</sup>, or pre-buckled wavy<sup>[69,137,149]</sup> geometries. Because the conductive materials are intrinsically rigid (elastic modulus  $\geq 1$  GPa) and inextensible, stretchable functionality must be engineered through microscale geometric design and cleanroom fabrication.

Another popular approach is to use conductive polymers and composites that are intrinsically soft and deformable. Polyurethanes (PU), polydimethylsiloxane (PDMS), polyacrylates, fluoropolymers, and styrene ethylene butylene styrene copolymer (SEBS) are typically used as the carrier medium. In order to be conductive, they are typically embedded with percolating networks of rigid metallic nano/microparticles<sup>[2,103]</sup> or carbon allotropes (e.g. MWCNT, graphene)<sup>[23,81,119,12,89]</sup> or grafted with polyaniline, ionomers (e.g. PEDOT:PSS), and other conductive polymer groups<sup>[172,147]</sup>. While promising for low-load/moderate-strain applications, these composites are typically more rigid and less elastic than homogenous elastomers, stretchable elastene fabrics, or natural biological tissue. Nonetheless, they have adequate mechanical properties for electronic skin applications and can be patterned using a variety of rapid fabrication methods.<sup>[22,91,116,165]</sup>

Alternatively, liquid-phase circuit interconnects represent a versatile alternative for stretchable electronics that bypass some of the limitations of deterministic architectures and polymer composites<sup>[62,59,16,27,67,21]</sup>. One popular approach is to introduce conductive fluids into gels. These gels provide many advantages including exceptional mechanical properties (low modulus and high extensibility and toughness), high visible light transmittance (99%), and are intrinsically biocompatible<sup>[64,68]</sup>. However, these ionically conductive gels rapidly dehydrate, unless coated with elastomer sealing layer<sup>[178]</sup>, have a fairly low electrical conductivity ( $\sim 0.2 \text{ S}\cdot\text{cm}^{-1}$ ; as compared to copper:  $5.96 \times 10^5 \text{ S}\cdot\text{cm}^{-1}$ ), and require specialized AC electrical circuitry to prevent electrolysis or polarization of the conductor making them difficult to integrate with common DC electronic circuits or used for DC power transmission.

Alternatively, Ga-based LM alloys like Ga-In eutectic (EGaIn; 75% Ga and 25% In, by wt.) or Ga-In-Sn (Galinstan; 68% Ga, 22% In,

10% Sn) are particularly attractive because of their low viscosity (2 mPa·s), high electrical conductivity ( $3.4 \times 10^4 \text{ S}\cdot\text{cm}^{-1}$ ), low melting point ( $-19^\circ\text{C}$  for Galinstan), low toxicity, and negligible vapor pressure<sup>[62,29,59]</sup>. When encapsulated in a soft elastomer (e.g. PDMS), liquid-phase traces of Ga-based alloy can provide highly robust electrical connectivity between solid state elements within a circuit and enable extreme elastic deformability. Another feature of Ga-based LM alloys is that, in O<sub>2</sub>-rich environments like air, they form a self-passivating surface layer of Ga<sub>2</sub>O<sub>3</sub> (thickness  $\sim 1\text{-}3 \text{ nm}$ ) that dramatically reduces surface tension and allows patterned traces to hold their shape<sup>[17,93,30]</sup>. This oxidation and moldability has enabled EGaln to be patterned with a variety of techniques<sup>[59,67]</sup> based on stencil lithography<sup>[55,57]</sup>, selective wetting<sup>[79,82,123]</sup>, reductive patterning<sup>[66]</sup>, micro-contact printing<sup>[150,47,30,161]</sup>, jetting<sup>[83]</sup>, direct laser writing<sup>[126]</sup>, and 3D direct-write printing<sup>[80,180,9,36]</sup>. Since the mid-2000s, EGaln microfluidic systems have been engineered for a broad range of applications.<sup>[16,27]</sup> In the last couple of years, this includes continued efforts in sensing and electromechanical transducers<sup>[157,110,122,74,60,19,112,104]</sup>, force characterization for medical endoscopy<sup>[24,50]</sup>, reconfigurable metamaterials<sup>[92,88]</sup>, electrochemical actuators<sup>[142]</sup> and mechanical switches<sup>[158,169]</sup>, and radio antennae that exhibit tunable operating frequency and enhanced range.<sup>[51,46,78,170,144,160,72,108]</sup>

Despite extraordinary potential, progress in soft and stretchable electronics is currently limited by the lack of integration of critical components to enable operation outside of a controlled laboratory environment. New unifying fabrication methods are needed that address unique challenges in material compatibility, multi-scale fabrication, and electrical and mechanical interfacing, while integrating common solid-state electronic components.

## 1.2 *Electrically self-healing soft-matter robotics and electronics*

These advances in mechanics and materials have resulted in highly flexible, stretchable, and conformable electronics that function as artificial skin and nervous tissue in a broad range of emerging applications, from “second-skin” wearable computing<sup>[49,1,20]</sup> to bio-inspired soft robotics<sup>[141,135]</sup>. However, the soft elastic materials typically used for these circuits and applications are susceptible to tearing, puncturing, and other forms of mechanical failure that lead to loss in electrical functionality. This limitation greatly prohibits the use of soft electronics in applications such as remote teleoperation, autonomous field robotics, or medical implants where repair is challenging or impossible. While rigid substrates and packaging can be used to mitigate damaging stress concentrations in traditional electronics, such

encapsulation will interfere with the elasticity of soft circuits. Instead, further advancements within these emerging fields depends on new classes of soft electronic materials that, like natural skin or nervous tissue, are self-healing and remain functional even as material is torn, ruptured, or removed.

Natural, biological systems exhibit remarkable adaptation and robustness in widely changing environments. Mimicking this level of robust functionality in soft-matter machines and electronics has the potential to create products with increased safety and longevity, while reducing material consumption. In the context of this thesis, I will primarily concentrate on materials that are capable of maintaining or restoring electrical conductivity when damage occurs. Polymers that are targeted to restore mechanical functionality after damage are quite different and are covered within Chapter 6. Recently, there has been exciting progress in the development of soft electronics that are capable of self-healing or that can be repaired when damaged to restore electrical functionality. These include semiconducting polymers<sup>[120]</sup>, conductive polymer networks<sup>[151,168,179]</sup>, ionic hydrogels<sup>[13]</sup>, LM microcapsules patterned on gold lines<sup>[8]</sup>, and LM microfluidics<sup>[125,83]</sup>. Although promising, these existing methods have at least one of several limitations: (i) extended period of functional loss during self-repair, (ii) need for manual reassembly, (iii) dependency on external or redundant electronics for damage detection and circuit restoration, (iv) need for external energy sources such as heat, light, or mechanical energy, and (v) dependency on non-ambient conditions such as increased relative humidity or temperature. Overcoming these limitations has the potential to dramatically improve longevity, performance, and functionality of deformable electronic materials.

### 1.3 *Damage sensing soft-matter composite*

As the performance and complexity of these systems continue to increase, continuous monitoring of the integrity of individual soft material components becomes increasingly important. This requires the ability to track material and structural health through the detection of damage and propagation of flaws and defects (self-reporting). Typically, this is accomplished through a variety of non-destructive evaluation (NDE) techniques, which can include ultrasonics, X-radiography, Eddy currents, magnetic techniques, and visual inspection<sup>[14]</sup>. However, these systems are often bulky and are more suited for periodic monitoring of components. This has inspired a variety of thin-film approaches that utilize visual inspection or ultrasonic techniques. Examples includes the use of dye penetrates or mechanically-induced color change through the use of specific chemical functional groups that un-

dergo mechanochemical reactions<sup>[127,26,131,136]</sup>. These techniques often result in a limited visual signal and can require controlled lighting conditions to increase reliability<sup>[85]</sup>. Micro-capsule techniques have recently demonstrated enhanced contrast with permanent color change<sup>[85]</sup>. However, visual inspection is best suited for line of sight applications, can be tedious and time consuming, and potentially unreliable, which limits their use in autonomous and deployable systems<sup>[155]</sup>. Compact piezoelectric or resistive systems can monitor damage remotely<sup>[111,143]</sup>. However, these systems are typically composed of stiff (modulus  $> 1$  GPa) and relatively brittle (strain  $< 10\%$ ) materials such as lead-zirconate-titanate (PZT) or polyvinylidene difluoride (PVDF), making them incompatible with soft and highly deformable materials and structures<sup>[65,114]</sup>.

In the case of monitoring damage in soft materials, where emerging applications take advantage of their soft and highly deformable nature, damage detection schemes must be mechanically compatible. Human nervous tissue provides an example of a soft material system that is capable of detecting, communicating, and responding to harmful external stimuli. This interconnected response in biological systems has inspired a wide range of stimuli-responsive materials that adapt or respond to environmental changes including temperature, mechanical or physical, optical, and chemical<sup>[148,140,154,75]</sup>. However, these systems often lack the ability to communicate these environmental changes with other existing technologies, as these responses often occur at a molecular level.

Integrated soft materials provide a path forward to enable intelligent, programmable interactions between external stimuli and dynamic material properties<sup>[105]</sup>. Recently, autonomy has been incorporated in soft-matter systems through intelligent mechanical design with preplanned tasks and on-board actuation, power, and computation<sup>[164,34,121,97,7,138]</sup>. While promising, these systems lack the necessary hardware and sensing to provide critical runtime feedback to modify the preplanned task. The comprehensive systems-level integration of components to enable soft-matter robotic materials to be fully self-aware of their current state still remains a significant challenge.

#### 1.4 *Contributions of this Thesis*

In this dissertation, I contribute to the development of a unifying framework for creating mechanically robust stretchable electronic circuits by integrating surface mount microelectronics with soft and stretchable liquid- or solid-phase circuit interconnects. To improve the robust-

ness of soft-matter electronics and robotics, a new material architecture and framework was developed that mimics the ability of soft, biological tissue to autonomously adapt, report, and respond to mechanical damage events.

**Systems-level integration:** I developed two novel fabrication methods for integrating surface mount microelectronics for signal processing, wireless communication, and power with soft and stretchable, solid-state/liquid-phase circuit interconnects. Specifically, I focused on advanced solid-state technologies with sub-millimeter-scale pins (Figure 1.4). Furthermore, these methods are compatible with conventional printed circuit board (PCB) manufacturing, enable reliable interfacing between the terminals of soft and stretchable circuit interconnects and I/O pins of packaged microelectronics, and allow for planar circuit features with dimensions below  $100\ \mu\text{m}$ . I demonstrate these unifying, multi-scale frameworks by fabricating a wearable pulse oximeter for health monitoring and a sensorized skin for gesture recognition.

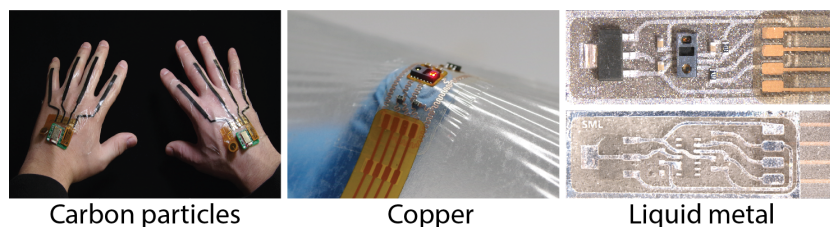


Figure 1.4: Stretchable electronic circuits created with chopped carbon particles, wavy copper, and liquid metal interconnects.

**Robust soft-matter electronics and robotics:** I introduce a new material architecture and framework for creating circuit interconnects that are capable of autonomous, electrical self-healing. The soft and highly deformable material is composed of droplets of Ga-based liquid metal (LM) alloy (gallium-indium, eutectic; EGaIn) embedded in a soft, silicone elastomer. In its natural (original) state following synthesis, this composite is electrically insulating, even for high LM volume fractions ( $\phi \geq 50\%$ ). However, application of extreme local pressure causes the LM droplets to rupture and coalesce to form locally conductive pathways with high electrical conductivity ( $\sigma = 1.37 \times 10^3\ \text{S}\cdot\text{cm}^{-1}$ , Figure 1.5). This mechanically-controlled response enables circuits to both be created and subsequently reconfigured when damage is induced, through the autonomous, in-situ formation of new electrical pathways. Since self-healing occurs spontaneously, this material does not require manual repair or external heat. I demonstrate this unprecedented electronic robustness in a self-repairing digital counter

and self-healing soft robotic quadruped that continue to function after significant damage.

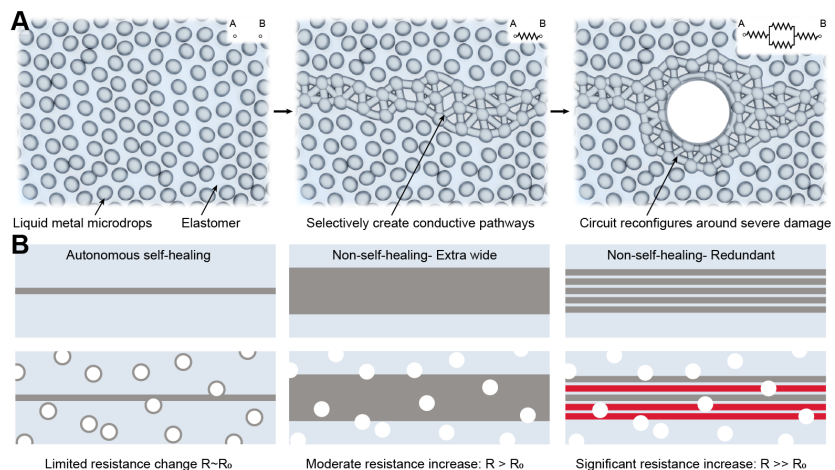


Figure 1.5: Self healing soft matter composite. (A) Schematic illustration of the self-healing mechanism where an initially insulating composite is selectively compressed to create electrically conductive LM traces. Upon damage, the LM trace autonomously reconfigures and maintains electrical conductivity. (inset) Equivalent electrical circuit schematic. (B) Schematic of different damage mitigation strategies. From left to right: (i) the new autonomous self-healing damage mitigation strategy presented here. (ii) A non-self-healing trace that is significantly wider than the expected damage size to prevent failure. (iii) Redundant non-self-healing traces to reduce the possibility of complete loss in conductivity.

**Soft-matter damage sensing composite:** The previously described LM-elastomer composite can also be used to detect and localize mechanical damage events. In response to mechanical damage—compression, fracture, or puncture—local conductive pathways between neighboring droplets are formed. This damage initiated change in electrical conductivity can be actively detected and localized using conductive electrodes patterned on the material, as indicated by the illumination of the LEDs as a notch propagates through the specimen (Figure 1.6). The electrical communication of damage enables direct integration with existing control systems, providing a method for soft-matter robotic systems to initiate an algorithmic response to adapt or recover from a detrimental, external event before reaching an irrecoverable state. To demonstrate the ability to detect, communicate, and respond to a potentially detrimental event, we use this material as an artificial nervous tissue in an inflatable soft humanoid structure, where multiple puncture events are rapidly detected, computed, and utilized in a control loop to prevent deflation and loss of functionality.

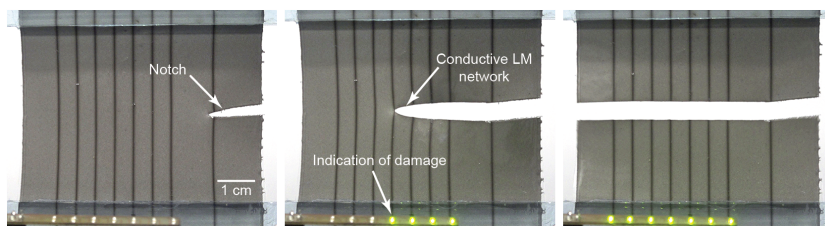


Figure 1.6: Photograph sequence of a notched sample that is strained until mechanical failure. The propagation of the notch creates a conductive network that is actively detected, as indicated by the illumination of the green LEDs.

**Future outlook:** I conclude this dissertation by extrapolation of clinical and robotic translations of the current work and next generation materials (Figure 1.7). For clinical translations, I explore how advanced integrated circuits can be directly integrated with custom fit 3D printed elastomer housings. For robotic translations, I investigate how stretchable electronics can be used to augment everyday objects and existing robotic systems. Finally, I explore next generation materials that are not only capable of electrical self-healing but also exhibit intrinsic mechanical self-healing characteristics.

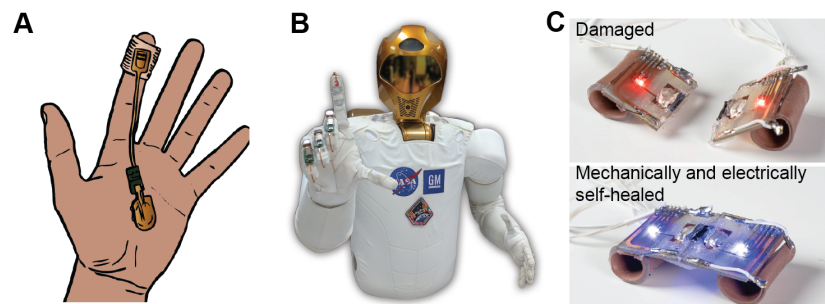


Figure 1.7: Future outlook and extrapolation of (A) clinical and (B) robotic translations of the current work and (C) next generation materials. (A) was drawn by Dr. Sara Abdollahi.

## 1.5 Dissertation Structure

I provide an overview of the related research within Chapter 1. I then dedicate one chapter to each topic: precision assembly of multi-layer stretchable electronic circuits (Chapter 2), stretchable electronic circuits with liquid-metal interconnects (Chapter 3), autonomously self-healing soft-matter electronics and robotics (Chapter 4), and damage sensing soft-matter composite (Chapter 5). I conclude this dissertation with a discussion of the future outlook on stretchable electronic circuits and self-healing electrical interconnects (Chapter 6).



## *Precision Assembly of Multi-Layer Stretchable Electronic Circuits*

**E.J. Markvicka, M.D. Bartlett, et al., *Advanced Functional Materials*, 2016<sup>[100]</sup>**

As mentioned in the introduction, emerging applications in soft robotics, wearable biomonitors, and physical human-machine interaction will increasingly rely on soft-matter technologies. To enable these soft-matter technologies to be useful outside of a controlled laboratory environment, the necessary circuit components for signal processing, wireless communication, and power must be integrated. Systems integration raises unique challenges in materials compatibility, multi-scale fabrication, and electrical and mechanical interfacing. In collaboration with Prof. Michael Bartlett, I present a unifying, deterministic adhesive transfer approach, to rapidly and efficiently create highly customizable stretchable electronic circuits. Precision laser micromachining is used to pattern individual conductive and insulating thin films, which are assembled into a multi-layer structure by controlling the interfacial adhesion of the substrate. Furthermore, this approach enables transfer and integration of rigid, surface mount microelectronics. This technique is demonstrated using commercially available materials and components to create thin, lightweight, and highly customizable sensor skins in under an hour. These fully integrated wireless, soft-matter devices conformably bond to the hand using a medical grade adhesive and are successfully used for monitoring hand gestures, pulse rate, and blood oxygenation.

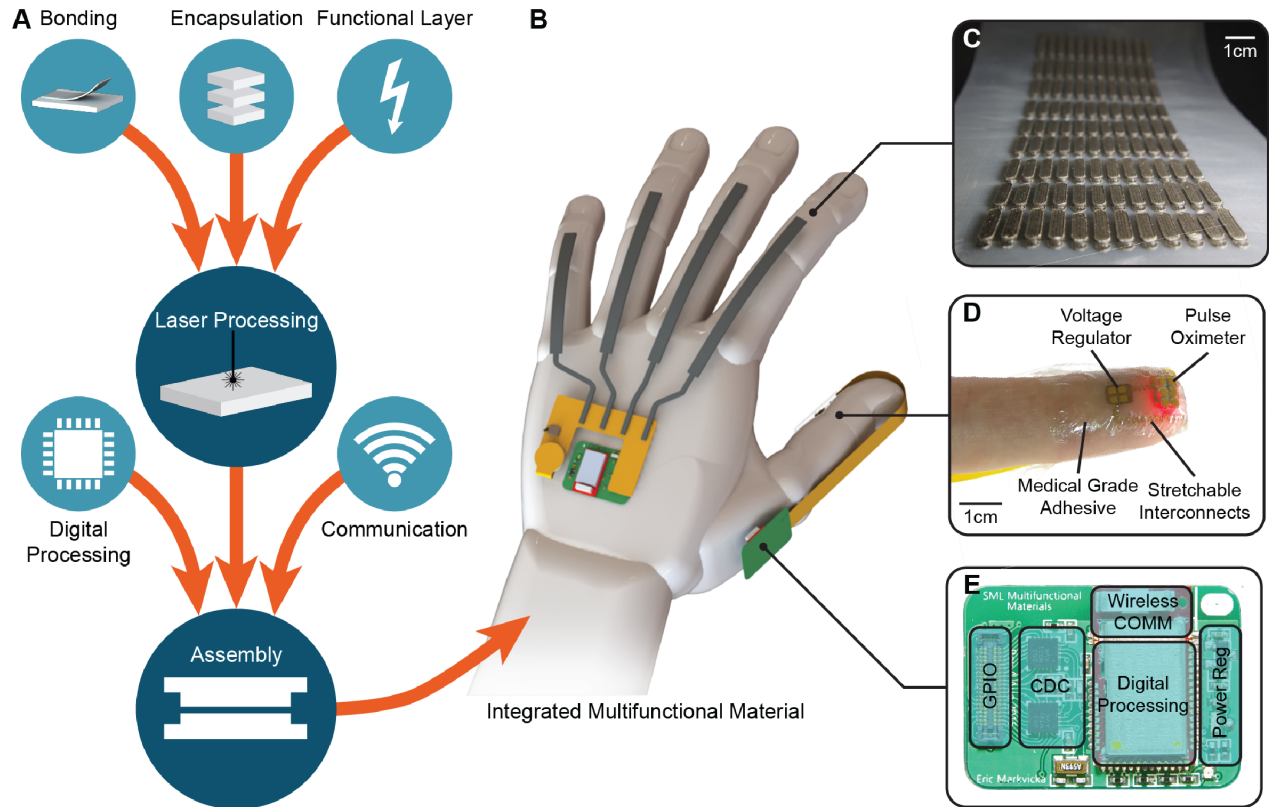
This work was completed in collaboration with Prof. Michael Bartlett (equal contribution), under the supervision of Prof. Carmel Majidi.

### *2.1 Background*

Robust integration of soft materials into wearable computing and biomonitors systems requires a comprehensive fabrication approach that allows for a broad range of electronic materials, substrates, circuit architectures, and surface-mounted technologies. This includes reliable methods for patterning, precision alignment, bonding, encap-

sulation, and electrical interfacing. The latter is particularly essential for local computation and communication<sup>[54]</sup>, energy-efficient wireless networks<sup>[45,176]</sup>, and connecting to external leads for power or signal processing<sup>[105]</sup>. Advances in rapid prototyping techniques, such as 3D printing and laser machining of soft materials, provide paths forward to achieve these objectives while accelerating design cycles and commercial development<sup>[129,91,22,94]</sup>. Recent work has shown how these approaches can enable the fabrication of multiple sensors at once with soft materials<sup>[129,94]</sup>. However, methods like 3D printing are limited in the mechanical and electrical performance of their build materials and do not support automated integration of IC components, which are necessary for fast, energy efficient, and miniaturized signal processing and communication<sup>[90]</sup>. This is especially limiting for applications in wearable physiological sensing and bio-monitoring that rely on packaged microchips for biosignal acquisition and processing. Of particular importance is the integration of photonic biosensing chips for photoplethysmography (PPG), which is used to measure vitals like heart rate and peripheral capillary oxygen saturation (SpO<sub>2</sub>). Therefore, the complete, sequential integration of numerous soft sensors with crucial components for communication, encapsulation, bonding or attachment layers, and stretchable electrical interconnects for power or signal processing still remains a significant challenge.

Here, I show the fabrication and evaluation of numerous, completely functional wearable electronics assembled on commercially available elastic films through rapid prototyping and assembly techniques that integrate multiple soft material layers and rigid elements in a single process (Figure 2.1A). I use a readily available CO<sub>2</sub> laser outfitted with a simple alignment system to allow for the precise assembly of sensors through deterministic, adhesion controlled soft transfer printing techniques. Assembly of the patterned material is controlled by modifying either the adhesion energy of the silicone substrate or by adjusting the laser processing conditions. The sensors do not require curing, surface modification, or additional chemical reactions and are bonded together through the inherent adhesion of the soft layers. This enables rapid fabrication that is not dependent on cure kinetics. The materials are characterized for stretchable strain sensing to over twice their original length and are shown to be stable, show little hysteresis upon cyclic loading, and are capable of being loaded over numerous cycles. This technique is extended to a UV laser system, which expands the choice of allowable materials (including thin metal film) and enables the rapid fabrication of custom stretchable electronics through deterministic architectures. I demonstrate the practical applicability of this approach with a soft, thin, and lightweight circuit that adheres to the skin and has on-board processing, power, and wireless communi-



ation for remote gesture monitoring and pulse oximetry (Figure 2.1B-E).

## 2.2 Fabrication Methodology

Rapid fabrication of soft functional materials is accomplished by using a combination of laser cutting with alignment control to create the individual layers and assembly of layers through the development of a soft transfer printing technique (Figure 2.3). The materials must satisfy criteria such as i) low effective elastic modulus, ii) high extensibility, iii) processable by laser cutting, and iv) bonding compatibility. To fulfill these criteria, I chose off-the-shelf materials including insulating (VHB 4905, 3M, thickness = 0.5 mm, surface resistivity  $> 10^{16} \Omega \cdot \text{sq}^{-1}$ ) and conducting (eCAP 7850, 3M, thickness = 0.15 mm, surface resistivity =  $10 \Omega \cdot \text{sq}^{-1}$ ) acrylic tapes. These materials are soft and highly extensible and due to their inherent adhesive characteristics provide robust adhesion upon lamination under light pressure without additional treatment. Additionally, these materials are readily available in roll form and thus offer the advantage of being easily accessible, avail-

Figure 2.1: Multifunctional biomonitors and assembly. (A) Scheme for fabricating and assembling multiple functional components into an integrated system for wearable biomonitors. (B) Schematic illustration of integrated multifunctional material on a hand model. (C) Photograph of an array of 108 soft strain sensors created through the rapid fabrication process. (D) Soft pulse oximeter mounted on a finger for wearable heart rate and peripheral oxygen saturation ( $\text{SpO}_2$ ) monitoring. (E) Analog and digital sensor data is collected, processed, and transmitted wirelessly through a modular, multifunctional Bluetooth Smart module.

able in large quantities, and amenable to scalable production.

To control alignment during cutting and subsequent assembly, I developed a simple alignment fixture that can be placed into a CO<sub>2</sub> laser cutter (30 Watt VLS3.50; Universal Laser Systems). The fixture has six degrees of freedom (DOF) to provide corrections in orientation and position for uniform cutting conditions across the substrate and repeatable alignment within the laser in XYZ for subsequent polydimethylsiloxane (PDMS) substrates (Figure 2.2). Alignment is provided by mating holes and slots in the PDMS substrate with corresponding pins on the alignment fixture during cutting and on a machine table for assembly. This provides low-cost, kinematically-constrained alignment with sub-millimeter precision<sup>[25]</sup>.

PDMS substrates (stamps) are placed on the fixture with a supporting backing featuring a machined hole and slot. The functional material to be patterned is laminated on the stamp and a custom planar design is cut. Excess material is removed from the stamp after cutting and subsequent layers are then laminated onto different stamps and laser patterned. Once the patterning (cutting) is complete, the individual layers are assembled through the deterministic soft material transfer printing process using a pair of locating pins on a machine table (Figure 2.3A). This process allows for efficient, parallel fabrication of numerous sensors simultaneously. I demonstrate this technique by creating a batch of 108 cm-scale strain sensors in under 45 minutes with 100% yield (Figure 2.3B). Further electrical characterization reveals that the sensors are nearly identical, with an average value of  $7.6 \pm 0.1$  pF across the array of sensors, a variance of less than 2% (Figure 2.3C).

### 2.3 Soft Transfer Printing Characterization

The assembly of both rigid and soft components through an adhesion based transfer printing process is challenging due to the varying material stiffness, viscoelastic response, and interfacial properties. Previous work with transfer printing soft elastomer layers includes decal transfer lithography, which involves chemical bonding treatments and multiple steps to transfer a single layer<sup>[18]</sup>. Kinetic controlled transfer printing can be used without chemical treatments but relies on rate dependent adhesion<sup>[107]</sup>, which can be challenging with multiple rate dependent components in the system. To overcome these challenges, I accomplish material assembly by controlling the substrate adhesion energy by modifying their viscoelastic response through PDMS mixing ratio and by using laser cutting to tune adhesion response. This enables deterministic material construction in multi-dimensional (2D/3D) layouts. To characterize the adhesion transfer process, 90°

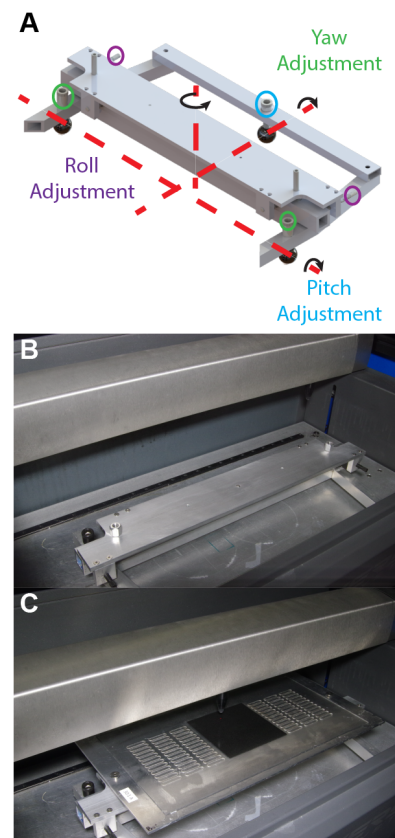
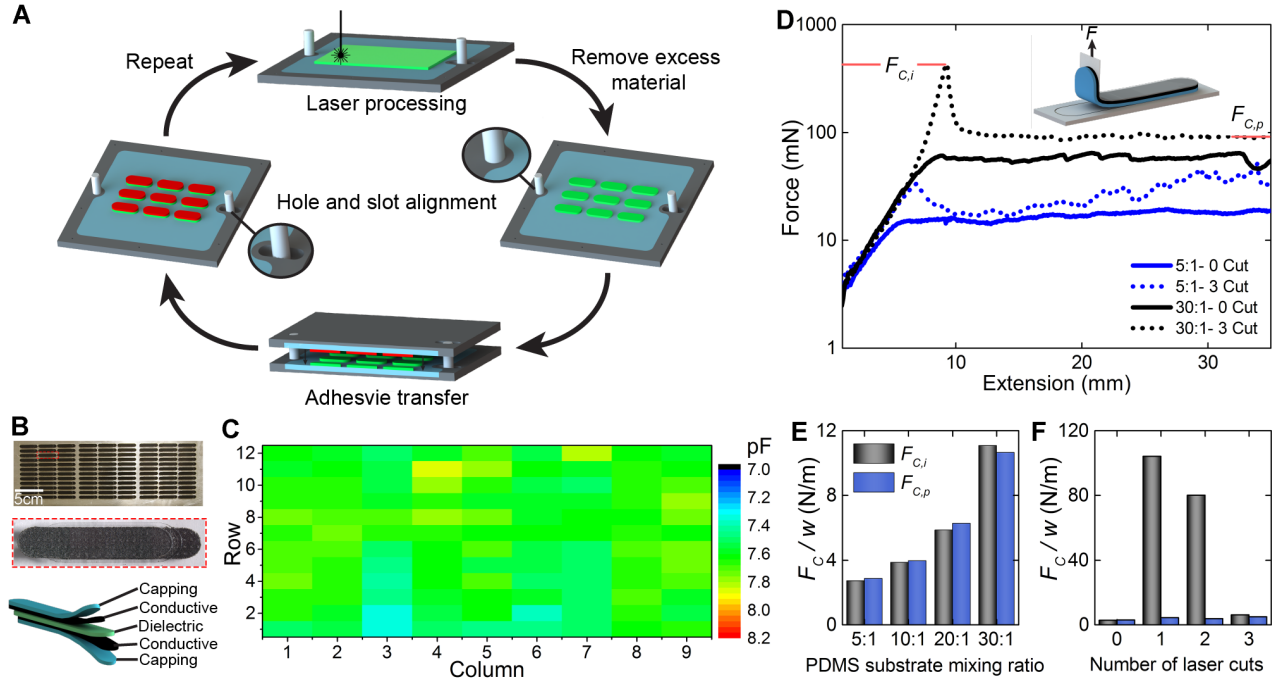


Figure 2.2: CO<sub>2</sub> Laser alignment system. (A) Schematic illustration of the laser alignment system with the ability to adjust orientation and position to optimize cutting across the entire surface. (B) Laser alignment system placed within the 30 Watt CO<sub>2</sub> Laser (VLS 3.50; Universal Laser Systems). (C) Image showing the PDMS substrate and sensor layer mounted in the laser on the alignment platform.



peel experiments are conducted. The samples are prepared in the same manner as the transfer process and after removing excess sensor material, an inextensible film was adhered to the sensor and then loaded into a peel setup. Representative peel adhesion curves for 5:1 and 30:1 (oligomer-to-curing agent ratio) substrates are presented in Figure 2.3D, where the force increases until crack initiation,  $F_{C,i}$ , and then drops as the crack begins to propagate at a constant force,  $F_{C,p}$ . Both the substrate choice and laser cutting conditions control the adhesion behavior and it should be noted that the y-axis is plotted on a log scale to capture the significant differences in adhesion force for the different conditions. Specifically, after three laser cuts the 30:1 substrate has an initiation force that is over  $10\times$  higher than the 5:1 substrate. This difference enables the samples to be controllably transferred from the 5:1 substrate to the 30:1 substrate.

This mechanism for adhesion control was investigated further by varying the substrate mixing ratio from 5:1 to 30:1 and the laser cutting was varied from 0 to 4 passes on the same location on the substrate. For the case where sensors are laminated onto the substrates with no laser cutting, there is an increase in peel adhesion force as the mixing ratio of the substrates increases (Figure 2.3E). This can be attributed to the increasing viscoelastic response of the materials as the mixing ratio increases due to greater dissipation near the crack tip<sup>[41]</sup>. Laser cut-

Figure 2.3: Deterministic adhesive assembly and characterization. (A) Scheme for rapid assembly of multilayered electronics using deterministic adhesive transfer. (B) Photograph of the 108 strain sensor array, a close up of an individual sensor, and a schematic showing the multilayered construction. (C) Contour plot of the capacitance values of the sensor array as a function of location across the entire sheet. (D) Force versus extension plot for a  $90^\circ$  peel experiment for two different substrates and laser processing conditions (note the y-axis is log scale). (E) Normalized peel force for different mixing ratios of PDMS substrates without laser processing. (F) Normalized peel force as a function of the number of laser cutting cycles on the 5:1 PDMS substrate.

ting also acts as a significant control parameter in this transfer process. As shown in Figure 2.3F, the peel initiation force increases by nearly  $40\times$  when a sensor is laser cut on the 5:1 substrate compared to just laminating the sensor onto the substrate. As subsequent cuts are made this initiation force decreases and on the third pass the force nearly returns to the laminated value. Optical microscopy images show that the sensor layers become impinged into the PDMS substrate upon laser cutting, which results in a greater force to separate the materials at the contact edge (Figure 2.4). This effect is reduced upon subsequent cutting as the already formed cut line in the PDMS reduces the interaction between the sensor layers and the substrate. This result allows the substrates to be used over many fabrication cycles, because the laser cutting effects diminish upon subsequent cutting and the substrate adhesion energy then dominates the transfer process. The stamp can also be preconditioned by running the laser cutter over the stamp at a reduced power and speed before the material is laminated to the stamp to diminish the impinging effect of laser cutting. This is especially important if transfer of the material (ink) is desired.

#### 2.4 Soft Sensor Characterization

Sensor characterization is performed under tensile loading to evaluate material performance. To investigate the transient effects of these sensors I first examine the influence of strain rate. Varying the loading rate from  $5 - 50 \text{ mm}\cdot\text{min}^{-1}$ , plots of the relative capacitance  $C/C_0$  versus strain all fall on the same line with all rates having a strain detection range over 100% strain (Figure 2.5A). In the case of the  $5 \text{ mm}\cdot\text{min}^{-1}$  loaded sample, reliable capacitance measurements are obtained for up to 150% strain (Figure 2.5A) with a gauge factor of 0.9. As the capacitance depends on the relative permittivity of the dielectric and the geometry of the sample, this result shows that the kinematics of the deformation are independent of loading rate. The capping layers (as seen in Figure 2.5B) are also found to have an influence on the maximum strain detection range that can be reliably measured. Referring to Figure 2.5B, the sensor range is observed to increase with the capping thickness. This response is attributed to a more uniform strain distribution induced by the thicker capping layer. Extended use of the sensors is characterized by performing cyclic loading up to 100% strain for 100 cycles at a frequency of 0.01 Hz. After an initial break-in period, the signal stabilizes and is repeatable for the remaining cycles (Figure 2.5C). Further cyclic testing was also performed at a higher rate (5 Hz) up to 25 000 cycles. The data shows that the sensor response slightly decreases after 1 000 cycles but is still functional at the end of the experiment showing the potential for long term use. Hysteresis

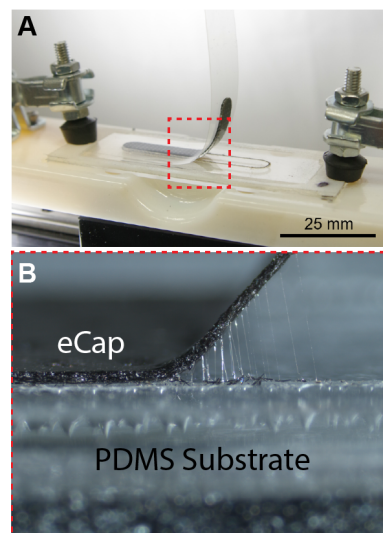


Figure 2.4: CO<sub>2</sub> laser impingement. (A) Test setup for the 90° peel adhesion experiment. (B) Optical microscopy of the sensor layer becoming impinged into the PDMS substrate upon laser cutting.

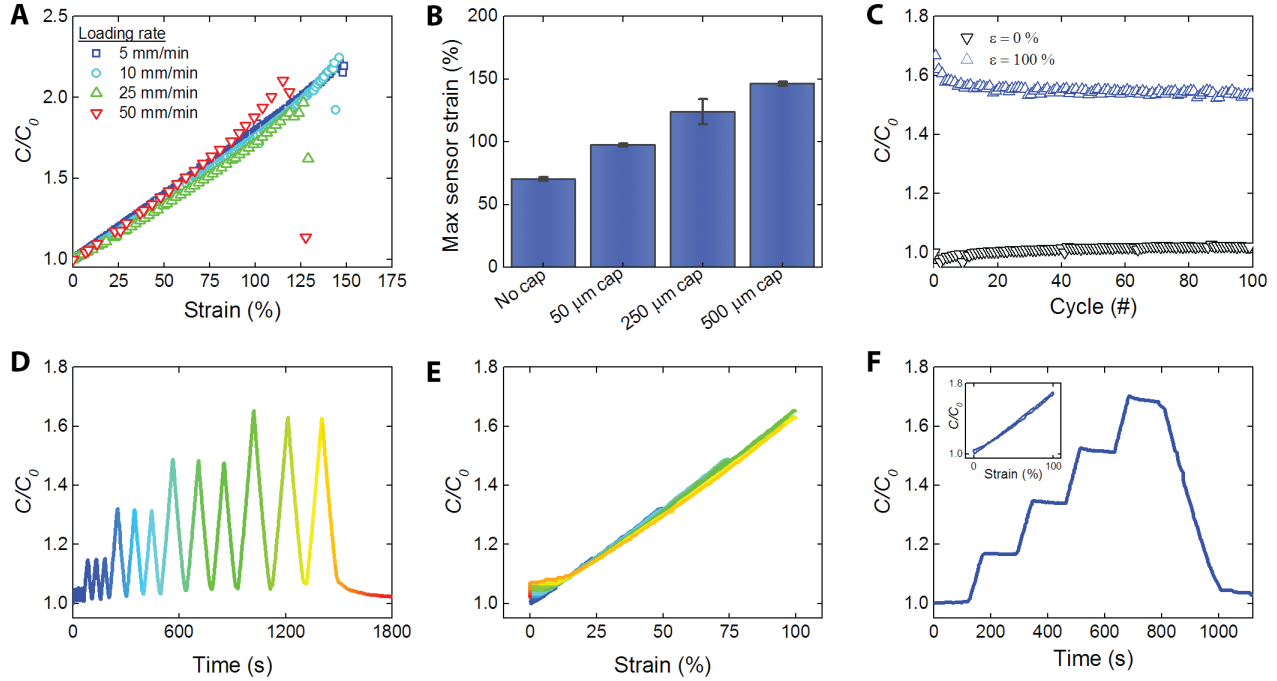


Figure 2.5: Soft strain sensor characterization. (A) Normalized capacitance versus strain under uniaxial deformation for four different loading rates. (B) The maximum strain measured by the soft sensors can be tuned by varying the thickness of supporting layers, errors bars are  $\pm 1$  s.d. ( $n = 3$ ). (C) The sensors are capable of undergoing multiple loading cycles, the data points correspond to the normalized capacitance values measured at 0 and 100% strain for each loading cycle. The x-axis is plotted on a log scale after 100 cycles. (D) Cyclic loading to increasing strains (10, 25, 50, 75, and 100%) plotted as a function of time and as a function of strain (E), where the cooler and warmer colors represent earlier and later times respectively. (F) Sensors are subjected to a strain and hold deformation profile (25, 50, 75, and 100% strain) and display minimal drift under constant loading. The inset shows the data as a function of strain. Plots in D, E, and F are smoothed with a 5-point median filter to improve data display.

is examined by performing cyclic loading experiments. The sensor is strained for three cycles at increasing levels of strain, from 10, 25, 50, 75, and 100% strain (Figure 2.5D). When plotting this data as a function of strain, the loading and unloading curves are indistinguishable, showing that the sensors have a very low hysteresis upon cyclic loading (Figure 2.5E). Lastly, the sensors are strained and then held for 120 s at increasing strains of 25, 50, 75, and 100%. When held in a strained state the sensors show little signal creep. This is an advantage of capacitive sensing over resistive sensors, which can display larger degrees of signal creep (Figure 3f)<sup>[116]</sup> When looking at this data as a function of strain (Figure 2.5F inset), the drops in capacitance are on the order of the hysteresis of the signal and thus do not contribute any more than cyclic loading. Additionally, I find insignificant capacitive artifacts from a human hand relative to the signal generated from deformation of the sensor. These experiments show the robust performance of the sensors over large deformations and many loading cycles.

## 2.5 Integrated Sensor Skin Experiments

Body mounted electronics that are designed to naturally interface with the human skin can provide inherent advantages and superior sen-

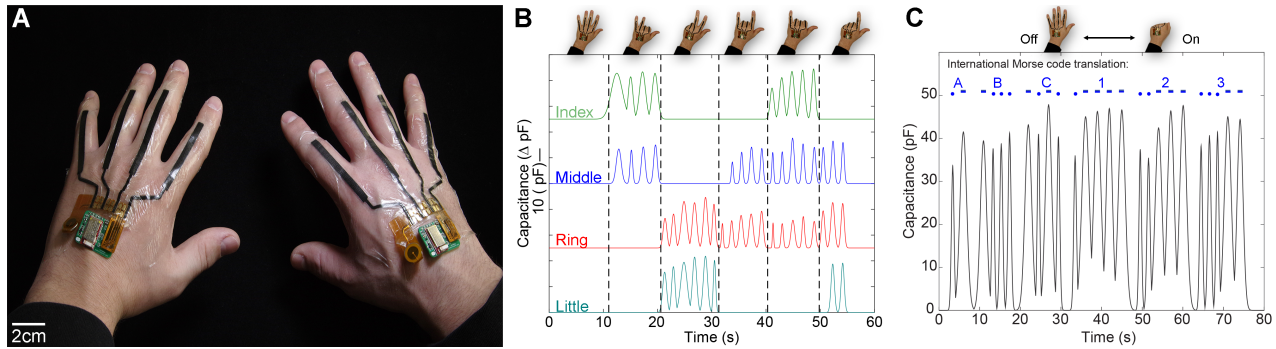


Figure 2.6: Wearable integrated sensing skin. (A) Photograph of sensing skin mounted on the hands, where the black material is the active sensor region which extends over the metacarpophalangeal and proximal interphalangeal joints of each finger. (B) Posture recognition of six different gestures on the hand. The photographs are the posture for each region. (C) Communication of Morse code through the opening and closing of the hand at different time intervals to represent dots and dashes. The Morse code translation of the signal is A-B-C-1-2-3. All data in the figure is transmitted wirelessly through the Bluetooth Low Energy (BLE) protocol.

sitivity for health monitoring compared to devices made from rigid materials<sup>[145,163]</sup>. To demonstrate the practical capabilities of the fabrication process, I produce two customizable integrated sensor skins in under an hour that adhere to the hand and monitor hand gestures. The skin contains four capacitive strain sensors that extend over the metacarpophalangeal and proximal interphalangeal joints of each finger. Stretchable circuit interconnects are used to connect the sensor elements to a flexible printed circuit (FPC) board that contains a Bluetooth transceiver and is powered with a coin cell battery (Figure 2.6A). As with the capacitive sensor electrodes, the interconnects are composed of laser-patterned eCAP 7850, which bonds to the terminals of the FPC. The fabrication of the soft integrated skin follows the methodology described in Section 2.2 with the added capability of transferring the FPC interface board onto the integrated sensing skin during the processing to ensure proper alignment. The integrated skin adheres to the hand using a medical grade, highly breathable adhesive dressing (Tegaderm, 3M). The wearable system is lightweight (less than 5 grams) and thin enough to fit under an examination glove.

The functionality of the integrated skin is shown by a series of hand gestures. As shown in Figure 2.6B, a variety of gestures are recognized by the integrated sensing skin. In these experiments, the fingers are cycled through different multifinger gestures, where capacitance of the individual strain sensors is measured at a frequency of 10 Hz. The signals are wirelessly transmitted to a host computer through the BLE protocol. The signals are then post-processed in MATLAB (R2015b). Alpha-numeric data communication is also possible through the integrated sensing skin, where Morse code can be generated by opening and closing the hand at different frequencies to generate the three communication states: dot, dash, and silence. This is demonstrated in Figure 2.6C, where A- B- C- 1- 2- 3 is transmitted and is interpreted through software to automatically identify the pattern of dots and dashes. Throughout the integrated sensing skin testing, 444 finger

states were recorded (finger open or finger closed). Of these, 96% of the finger states were correctly identified. The interface between the sensors and the FPC was also evaluated under cycling bending loading. After 25 000 cycles, the interconnects were still functional and showed a decrease in resistance over time, showing the electrical and mechanical robustness of the integrated sensor skin created through our rapid fabrication process. The ability to rapidly generate wearable integrated sensing skins without the need for pattern masks enables faster design cycles and flexibility in creating custom wearables for multiple users.

## 2.6 *Skin Mountable Pulse Oximeter Device Experiments*

To extend this fabrication methodology to a wider variety of materials, I utilize a UV laser micromachining system (ProtoLaser U3; LPKF), which is capable of patterning metals in addition to polymeric materials. Instead of an alignment platform, the laser micromachining system is equipped with a fiducial recognition camera. Material assembly follows the same principals as the CO<sub>2</sub> laser fabrication, where alignment pegs control layer alignment, and deterministic adhesion transfer printing is used to assemble each layer into a multilayer construction. I take advantage of the additional material capabilities by laser patterning serpentine architectures of stretchable interconnects out of 70  $\mu\text{m}$  thick flexible copper-clad (FR7031 DuPont) to create a wearable pulse oximeter (Figure 2.7A). This soft device is capable of bending and stretching (Figure 2.7C, D) and consists of a combination of soft materials and rigid components that are all sequentially assembled through the laser patterning and adhesion assembly process. During assembly of the rigid components the PDMS substrate thickness was chosen so that the lateral dimension of the rigid component was no more than twice the substrate thickness to avoid adhesion effects from substrate confinement<sup>[3,4]</sup>. The multilayer composite consists of a medical grade adhesive for bonding to the skin, laser patterned flexible copper-clad interconnects, and a through thickness conductive adhesive layer (ECATT 9703, 3M, thickness = 0.05 mm, contact resistance < 0.3  $\Omega$ ). The ECATT serves to electrically and adhesively connect the interconnects to the active and passive electrical components while preventing shorting within the plane of the circuit (Figure 2.7B). I take advantage of the parallel processing capabilities of the assembly process to simultaneously assemble four fully functional wearable pulse oximeter devices in under an hour. The integration of the soft and rigid elements is robust and maintains functionality after 25 000 bend cycles to a radius of 5 mm. The ability to assemble planar as well as three dimensional components of both soft and rigid elements in

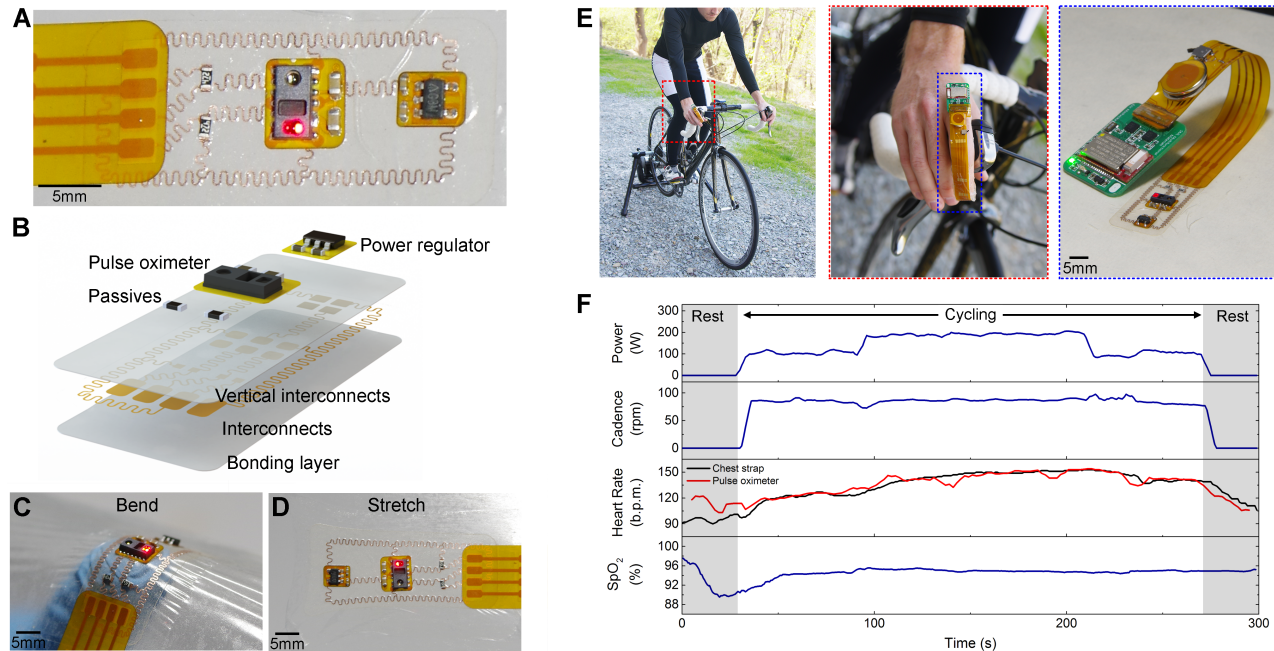


Figure 2.7: Wearable pulse oximeter and characterization. (A) Photograph of the wearable pulse oximeter, with the red LED illuminated. (B) Schematic of the device in (A) showing the different layers and component layout. (C) The pulse oximeter is capable of undergoing bending and (D) stretching. (E) The wearable pulse oximeter mounted on the index finger of a cyclist on a stationary bicycle. (F) Data as a function of time for a graded cycling test, where power output is stepped up and down and heart rate and SpO<sub>2</sub> are measured with the wearable pulse oximeter.

a parallel manner provides versatility to create a variety of functional wearable devices.

The functionality of the wearable pulse oximeter device is investigated while cycling on a stationary bicycle (Figure 2.7E). The pulse oximeter data is collected at a frequency of 200 Hz and transmitted wirelessly using the BLE protocol at 15 Hz. The pulse oximeter is attached to the index finger of a human subject during a graded-load exercise test in which cycling power is stepped up from 0 W at 30 s to 100 W for 60 s, increased to 200 W for 180 s, stepped back to 100 W for 60 s, and then 0 W for 30 s (Figure 2.7F). During this protocol heart rate and peripheral oxygen saturation (SpO<sub>2</sub>) are continuously measured through the pulse oximeter while power and cadence are measured externally through the bicycle hub and an additional heart rate signal is captured through a chest strap. As shown in Figure 2.7F, heart rate increases as the power output increases, and the heart rate measured from the wearable pulse oximeter is in good agreement with the chest strap. Additionally, blood oxygen is found to vary as the subject steps cycling power up and down, as is commonly observed during exercise [139].

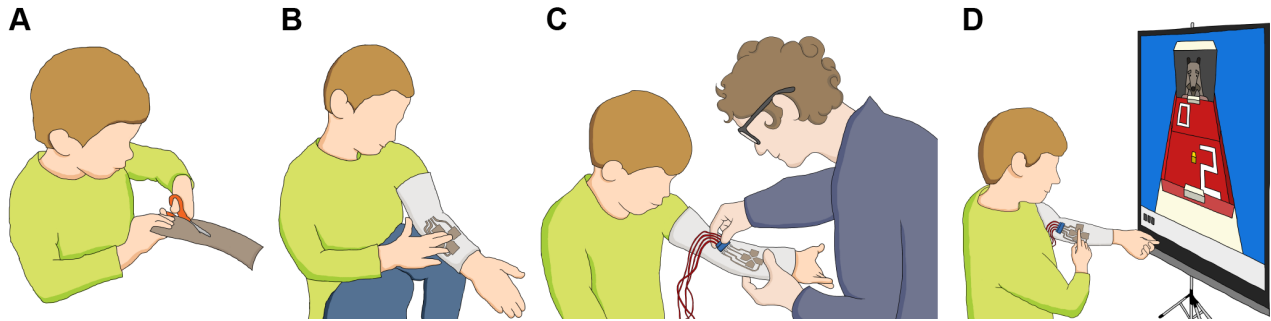


Figure 2.8: Illustration of the primary segments of the STEAM workshop on wearable computing. (A) Students fabricate a wearable human-interface device out of conductive fabric tape. (B) The conductive tape touch sensors are adhesively bonded to an arm sleeve. (C) The wearable device emulates a USB keyboard and is interfaced to a computer using open-source hardware. (D) The device can be used to control a computer program or game.

## 2.7 STEAM Outreach

There has been growing popularity in do-it yourself (DIY) electronics for wearable computing and human-machine interaction. This has introduced exciting opportunities to promote science, technology, engineering, art, and mathematics (STEAM) education that highlights the intersection of electronics, materials, and artistic expression. An outreach program for middle school students (grades 7-9) that builds upon our previous work in wearable electronics. In collaboration with Steven Rich, Jiahe Liao, and Hesham Zaini, I present an outreach program that integrates engineering and arts to create a wearable human-computer interface device (Figure 2.8). In this workshop, students learn the scientific principles underlying touch sensing and apply these lessons to design and build a device that is both functional and aesthetic. Our design leverages inexpensive, commercially available materials, basic craft skills, and open-source hardware and software to emulate a USB keyboard that students can use to control a computer program or game. Illustrations of primary segments of the STEAM outreach workshop is shown in Figure 2.8. Ref. [99] reports the essential resources to develop new outreach efforts based around wearable technologies to complement or enhance existing educational programs and curricula.

## 2.8 Outlook

Here, in collaboration with Prof. Michael Bartlett, I introduced a rapid fabrication process for soft multilayered electronics that allows for the seamless incorporation of rigid components with soft materials, enabling fully integrated, multifunctional devices for applications in soft robotics, wearable computing, and human-machine interaction. I demonstrate our efficient, highly customizable, and readily accessible process on two different laser micromachining systems at the sub-mm to cm scale. More than ten different materials (integrated circuits, dis-

crete electrical components, and insulating and conductive soft films) are transferred using this deterministic adhesive transfer approach with varying shapes (2D/3D), sizes (0.01 to 100 cm<sup>2</sup>), and materials properties (Young's modulus from  $\sim 100$  kPa to 100 GPa). Adhesion-controlled transfer was influenced by the choice of substrate (peel initiation force increases greater than  $10\times$ ) and laser cutting conditions (peel initiation force increases by nearly  $40\times$ ). I demonstrate the efficiency of this technique by creating a batch of 108 cm-scale strain sensors in under 45 minutes with 100% yield that show low signal hysteresis and signal creep during stretching. Such versatility allowed the realization of wireless, low-power, biomonitoring devices that adhere to the skin. These include a highly customizable soft integrated skin with strain sensors for gesture monitoring and a wearable pulse oximeter circuit with deterministically-patterned stretchable copper interconnects. Both devices are fabricated in under 1 hour, demonstrate reliable operation for greater than 4 hours, and are functional weeks after initial testing. This fabrication method is applicable to a wide range of material sets (filled elastomer composites and flexible, thin-film serpentine interconnects), making it compatible with many materials currently used for stretchable and flexible electronics.

While this fabrication methodology provides a path forward for the design and optimization of a wide range of devices for diverse applications, these material sets are limited to moderate strains ( $\sim 50\%$  strain). Furthermore, particle-filled elastomers have a low volumetric conductivity ( $< 10^3$  S $\cdot$ cm<sup>-3</sup>), exhibit electrical hysteresis, and experience rapid increases in trace resistance when stretched. The theoretical prediction using Ohm's law for an incompressible solid with fixed volumetric resistivity often significantly underpredicts this extreme rise in resistance, which is undesirable for most circuit applications. An alternative approach, explored in the following chapters is to use a liquid-phase metal alloy, which has a high volumetric conductivity ( $3.4 \times 10^6$  S $\cdot$ m<sup>-1</sup>), low viscosity (2 mPa $\cdot$ s), and negligible toxicity<sup>[29]</sup>.

### 3

## *Stretchable Electronic Circuits with Liquid Metal Interconnects*

**T. Lu, E.J. Markvicka, et al., ACS applied materials & interfaces, 2017<sup>[96]</sup>**

Ga-based, room temperature liquid metal (LM) alloys have become an increasingly popular material choice for conductors and soft sensors in stretchable electronic circuits<sup>[28]</sup>. Specifically, eutectic Ga-In (EGaIn) and Ga-In-Sn (Galinstan) alloys have gained significant attention because of their high electrical and thermal conductivity, low viscosity, negligible toxicity (as compared to Hg), and ability to wet a variety of host substrates. Furthermore, these liquid-phase metals can introduce unique intrinsic material properties (electrical, mechanical, or thermal), while preserving the properties of the host elastomer matrix.

This work was primarily completed by Dr. Tong Lu. I contributed to the intellectual conception of the research and supported the development and analysis of the soft-matter PCB implementations. Here, in collaboration with Dr. Tong Lu and Yichu Jin, I present a unique layout for soft-matter electronics in which traces of liquid-phase eutectic Ga-In (EGaIn) are patterned with UV laser micromachining (UVLM). An anisotropic, z-axis conductive elastomer is developed to electrically and mechanically interface the liquid-phase circuit interconnects with the pads of surface-mount devices (SMD). The processing technique is compatible with conventional UVLM printed circuit board (PCB) prototyping and exploits the photophysical ablation of EGaIn on an elastomer substrate. Potential applications to wearable computing and biosensing are demonstrated with functional implementations in which photoplethysmogram (PPG) signals are collected using a soft-matter PCB.

This work was completed in collaboration with Dr. Tong Lu and Yichu Jin, under the supervision of Prof. Carmel Majidi. This project was primarily completed and lead by Dr. Tong Lu. I contributed to the intellectual conception of the research and supported the development and analysis of the soft-matter PCB implementations.

### 3.1 Background

Despite their extraordinary potential, progress in LM electronics is currently limited by methods for integration with MOSFETs, microprocessors, chipsets, cable adapters, and other solid-state technologies (SSTs). Recent efforts with so-called dual-trans printing<sup>[161]</sup> and z-axis conductive elastomer<sup>[95]</sup> have successfully addressed integration but only with millimeter-scale pins and traces. Successful integration of LM-based circuits and micro-scale SSTs requires processing techniques that are (i) compatible with conventional PCB manufacturing, (ii) enable reliable interfacing between the terminals of the LM circuit and I/O pins of packaged electronics, and (iii) allow for planar circuit features with dimensions below 100  $\mu\text{m}$ .

### 3.2 Fabrication Methodology

Here, a unique layout for LM-based soft-matter electronics is reported that simultaneously addresses challenges in multi-scale fabrication and electrical and mechanical interfacing between liquid-phase interconnects and solid-state microelectronics (Figure 3.1A). As in conventional PCB prototyping, a UV laser micromachining (UVLM) system (Protolaser U<sub>3</sub>; LPKF) is used to pattern a  $\sim 20$   $\mu\text{m}$  thick coating of LM on a polymer substrate. The Protolaser U<sub>3</sub> is a Nd:YAG laser with 355 nm wavelength, 200 kHz pulse rate, and 15  $\mu\text{m}$  diameter beam that is capable of direct photophysical ablation of metal. Using a 1W beam power, the liquid metal features can be reliably patterned with planar dimensions of 50  $\mu\text{m}$ . In contrast, previous attempts at EGaIn patterning with a CO<sub>2</sub> laser require indirect material expulsion through vapor recoil force that limits the minimum feature size to  $\sim 250$   $\mu\text{m}$ <sup>[94]</sup>. I also show that UVLM-patterned EGaIn circuits can interface with surface-mounted SSTs using an anisotropically conductive “z-axis film” composed of vertically-aligned columns of EGaIn-coated Ag-Fe<sub>2</sub>O<sub>3</sub>  $\mu$ -spheres embedded in a PDMS matrix (Figure 3.1B). In contrast to conventional z-axis films with “dry” ferromagnetic microparticles<sup>[95]</sup>, the LM-coating allows for electrical connectivity even as the rigid  $\mu$ -spheres separate under mechanical deformations induced by circuit bending, compression, stretching, or twisting.

As with EGaIn stencil lithography and additive manufacturing, the ability to laser-pattern EGaIn on an elastomeric substrate depends on the formation of a self-passivating, nanometer-thin Ga<sub>2</sub>O<sub>3</sub> “skin.” The oxide skin that allows the patterned liquid metal to hold its shape after laser ablation (Figure 3.1C) and during deposition of an elastomer seal. This feature of liquid moldability is critical for extending conventional UVLM PCB prototyping to Ga-based LM alloys. Combining UVLM

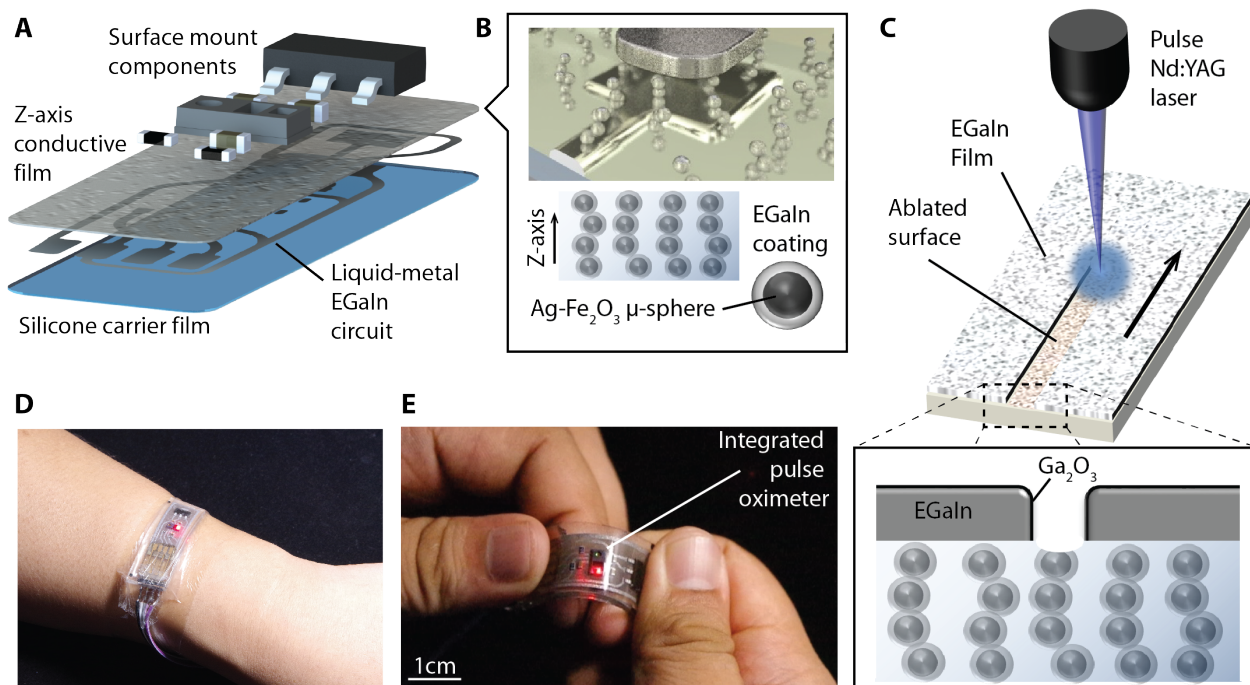


Figure 3.1: Liquid-metal soft-matter electronics. (A) Illustration of soft-matter bioelectronic skin. (B) Vertically aligned columns of Ag-Fe<sub>2</sub>O<sub>3</sub> microparticles coated in EGaIn act as z-axis interconnects between LM trace terminals and surface-mounted components. (C) Illustration of EGaIn patterned using UVLM. During patterning within an oxygen-rich environment, the growth of Ga<sub>2</sub>O<sub>3</sub> is necessary to hold the shape of the LM circuit (see inset). (D) Soft-matter bioelectronic skin with integrated pulse oximeter that can be worn as a wrist band and (E) support mechanical deformation during operation.

processing with liquid metal and z-axis connectivity allows for a versatile method to produce elastically deformable electronics that are mechanically robust and compatible with natural human tissue. Referring to Figs. 3.1D-E, potential applications include an elastomeric band that contains a surface-mounted pulse oximetry unit for reflective photoplethysmogram (PPG) recordings. The PPG waveforms can be used to non-invasively measure blood oxygenation saturation and heart rate, which in turn can be used for tracking physical activity and monitoring a broad range of health conditions<sup>[109]</sup>. As with other recent photonic bioelectronic devices<sup>[37,175]</sup>, the circuit is naturally soft and flexible and can conform to the skin without requiring significant attachment forces.

Soft-matter PCBs with embedded LM wiring are produced using the fabrication steps presented in Figure 3.2, details of which are presented in Section 7.2. The steps presented in Figure 3.2A-C involve embedding SST chips inside a layer of PDMS (Sylgard 184; 10:1 base-to-curing agent ratio; Dow Corning) such that the board side of the chips are exposed and flush with the elastomer surface. As shown in Figure 3.2D, the exposed chips are covered with an uncured layer of zPDMS that is composed of the following: 35 wt% of 40  $\mu\text{m}$  diameter Ag-coated Fe<sub>2</sub>O<sub>3</sub> particles (20% Ag by wt.; SM40P20, Potters Industries LLC), 15 wt% of EGaIn (75 wt% Ga and 25 wt% In; Gallium

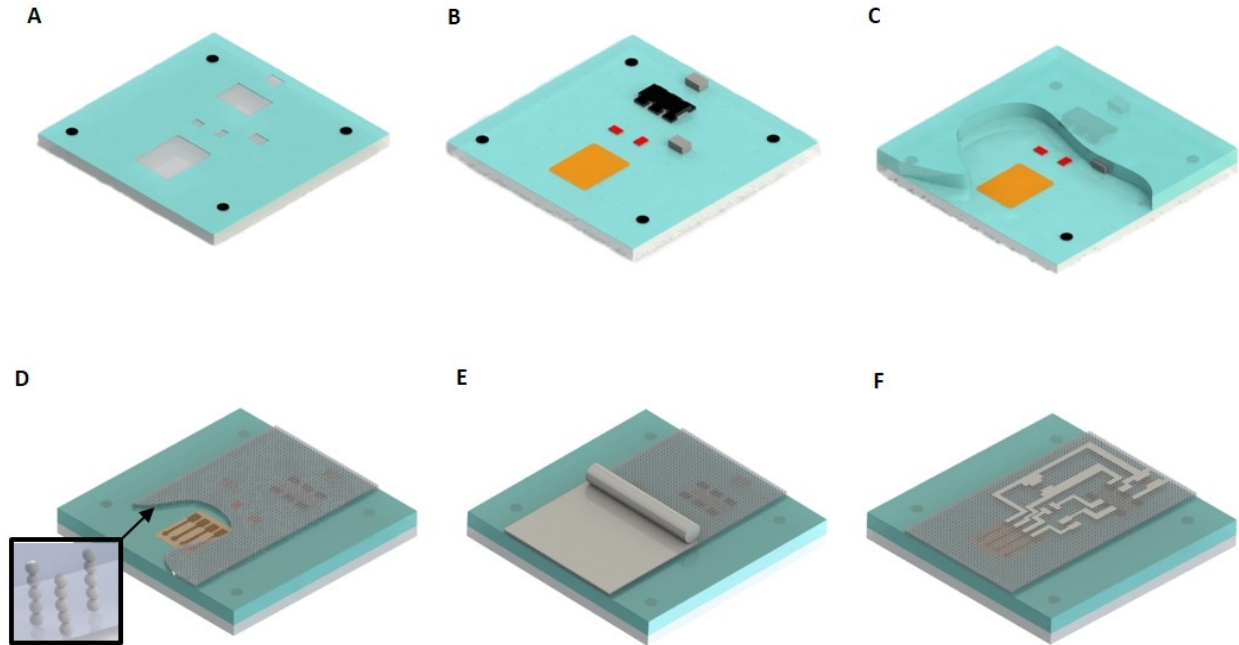


Figure 3.2: Fabrication process with UVLM. (A) A PDMS substrate is applied onto a glass plate. Placement openings and fiducials are patterned with UV laser for placing surface mount components and laser alignment, respectively. (B) Surface mount electronic components are placed into the openings with PVA as a bonding agent. (C) The components are then sealed in PDMS. (D) The chip-embedded elastomer is peeled from the glass plate, flipped over, and coated with a layer of zPDMS. (E) A film of EGaln is applied on the zPDMS with a PDMS roller and then (F) patterned with a UVLM system. Lastly, the LM circuit is sealed in PDMS and released from the glass substrate.

Source), and 50 wt% of PDMS. Before adding PDMS, the Ag-Fe<sub>2</sub>O<sub>3</sub> and EGaln are mixed together so that the ferromagnetic microspheres have a LM coating, as illustrated in Figure 3.1B. Next, the zPDMS layer is deposited on top of the exposed SSTs with a spin coater (1500 RPM for 10s; KW-4A, SPI) and is then cured in an oven (100°C for 20 min) while the entire sample is placed on top of a flat magnet (~1448 Gauss, 2"×2"×1/4" NdFeB; K&J Magnetics, Inc.). As the elastomer cures, the applied magnetic field causes the EGaln-coated ferromagnetic particles to assemble into vertically-aligned columns. After the zPDMS layer is cured, it is coated with a ~20 μm-thick film of EGaln that is then patterned using UVLM. Laser ablation is performed with a beam power of 1W and marking speed of 150 mm·s<sup>-1</sup>.

Referring to Figure 3.3A, a film of EGaln on zPDMS can be patterned into features with dimensions as small as 50 μm. The widths of the traces are 500, 200, 100, and 50 μm and the diameters of the circles are 1000, 500, 200, and 100 μm, respectively. For the selected laser settings (1W power, 150 mm·s<sup>-1</sup> mark speed), the trace width and spacing are limited to 50 and 100 μm, respectively, which is consistent with conventional PCB manufacturing. If narrower than 50 μm, there becomes a significant likelihood that the traces can be non-conductive due to poor localized wetting or excessive removal of EGaln. Likewise, for minimum line spacings below 100 μm, residue from unablated EGaln or the presence of EGaln-coated ferromagnetic particles

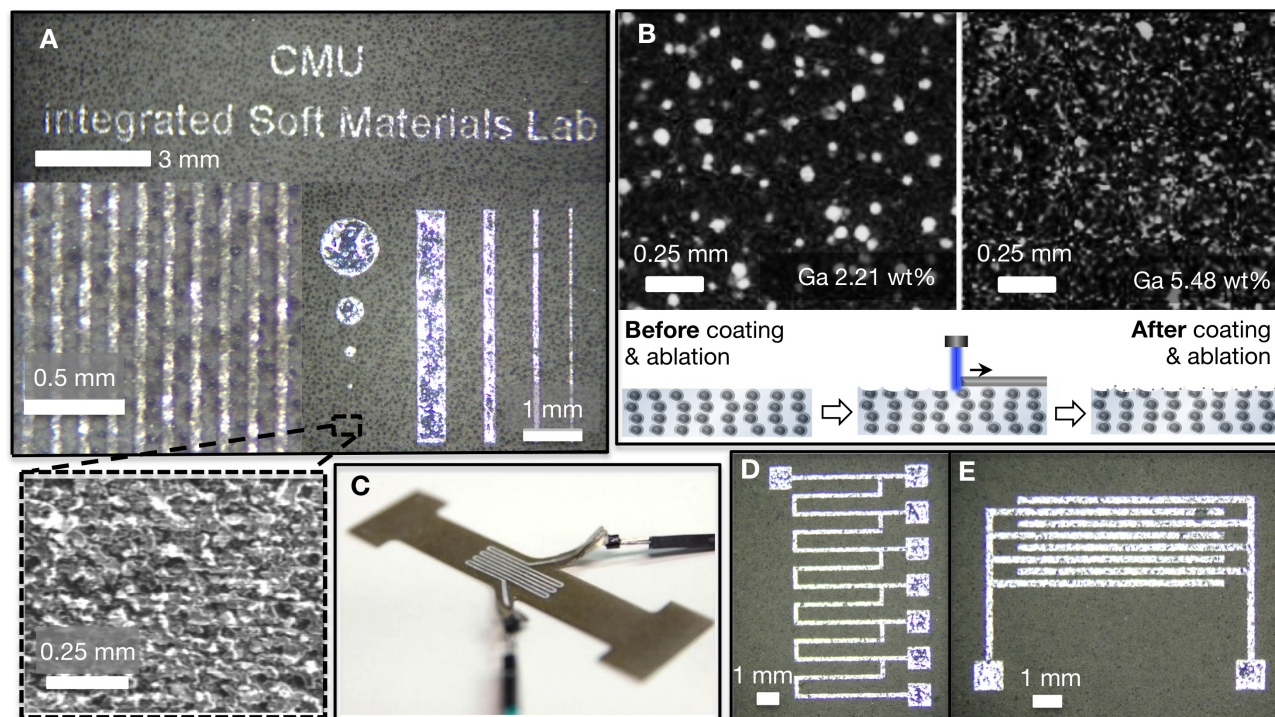


Figure 3.3: Samples of UV laser-patterned EGaIn features. (A) The planar dimensions of patterned traces can be as small as  $50\ \mu\text{m}$ . The SEM image in the inset shows the rough surface of zPDMS after laser ablation. (B) The EDS image of elemental distribution of Ga before and after EGaIn coating and laser ablation. (C) Serpentine circuit used to measure electrical resistance during stretch. (D) EGaIn circuit with multiple terminals for measuring the influence of trace length on resistance. (E) Interdigitated capacitor for measuring the influence of trace length on capacitance.

could lead to in-plane electrical shorting.

As shown by the scanning electron microscopy (SEM) scan (FEI Quanta 600) in the Figure 3.3A inset, the laser not only removes EGaIn but will also textures the zPDMS substrate. The effect of laser ablation on EGaIn removal is further examined by comparing Ga content on the surface of a zPDMS substrate before and after coating and ablation (Figure 3.3B) using energy dispersive spectroscopy (EDS). For uncoated and unablated zPDMS, Ga is mostly observed on the surface of the ferromagnetic particles that support z-axis conductivity in the zPDMS. After an EGaIn coating is applied and removed by UVLM, the substrate is found to be covered in a uniform coating of Ga residue. Moreover, coating and ablation results in an increase in Ga weight fraction (from 2.21 to 5.48 wt%) as shown in Figure 3.3B, which suggests that not all of the EGaIn coating is ablated. Similar results are observed with EDS analysis of In content (weight fraction increases from 0.51 to 1.27 wt%), as shown in Figure 3.4. The laser fume extraction system evacuates any of the ablated particles that become airborne (CSA626, Quarto Air Technologies Inc.). In conventional UVLM-based PCB fabrication, this same exhaust system is used to remove  $120\ \mu\text{m} \times 20\ \text{mm}$  strips of copper from a copper clad substrate.

The electrical and electromechanical properties of UV laser-patterned EGaIn traces are examined using a variety of circuit designs (Figs. 3.3C-

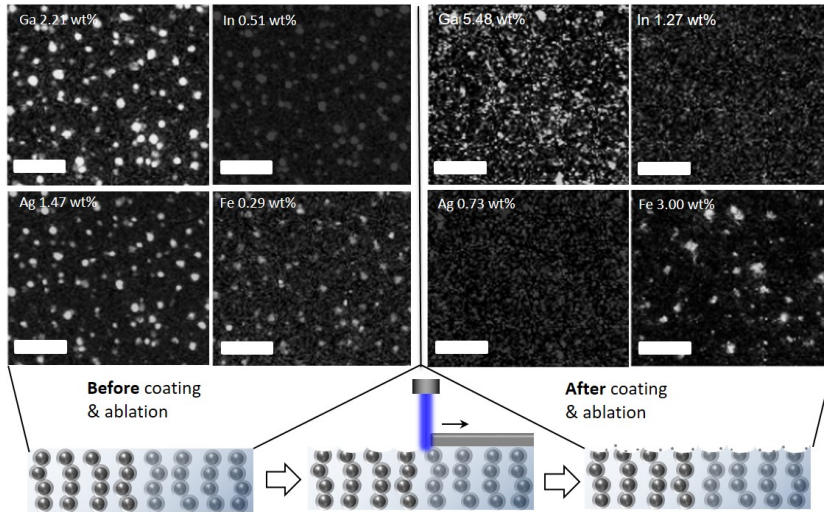


Figure 3.4: SEM image of coated/patterned and uncoated/unablated zPDMS. The EDS test results for Ga, In, Ag, and Fe content on the surface of zPDMS before (left) and after (right) coating and ablation. It is shown that the contents of both Ga and In increase after coating and ablation. The observed content of  $\text{Fe}_2\text{O}_3$  also increases because the outer coating of Ag on the particles is ablated during UV laser ablation and the cores are exposed. Scale bars:  $250 \mu\text{m}$

E & 3.5A-C). A serpentine EGaIn trace is used to measure electrical resistance as a function of stretch (Figure 3.5A). The serpentine part of the EGaIn trace is 120 mm long and 0.5 mm wide and stretched to 60% strain (in increments of 5%). Resistance versus stretch is fitted using the following Ohm's Law formulation:  $R = R_0 + R_1\lambda^2$ , where  $R_0 = 3.7\Omega$  is the resistance of the leads and  $R_1 = 4.3\Omega$  is the initial resistance of the unstretched serpentine trace. Stretch,  $\lambda$ , is defined as the final length of the sample divided by its initial length. Beyond 60% strain, the sample fails mechanically (as further discussed below). However, UVLM-patterned LM traces on a soft polyacrylate substrate (VHB tape, 3M) can be stretched to beyond 225% before failing (Figure 3.5A inset). Ohm's Law is also used to predict the linear influence of trace length on electrical resistance for EGaIn traces of widths 100 and  $200 \mu\text{m}$  (Figure 3.5B;  $R^2 > 0.96$ ).

Capacitance is measured with interdigitated electrodes of  $250 \mu\text{m}$  width,  $150 \mu\text{m}$  spacing, and varying overlap length (Figure 3.5C). As expected from electrostatic field theory (see Section 7.2 and Figure 7.1), the dependence of capacitance on overlap length is approximately linear ( $R^2 > 0.9$ ). The laser-processed method was compared to stencil lithography and is statistically similar (Figure 3.5D). Lastly, a soft-matter printed circuit board with three  $331\Omega$  surface mount resistors oriented at 0, 45, and 90 degrees was characterized under tensile loading to evaluate performance. The sample was loaded at  $10 \text{ mm}\cdot\text{min}^{-1}$  and only a modest increases in resistance ( $<10\%$ ) was recorded until mechanical failure occurred at slightly over 60% strain (Figure 3.5E-F). This suggests that tensile loading had only negligible influence on the contact resistance between the chip pins, zPDMS, and LM leads.

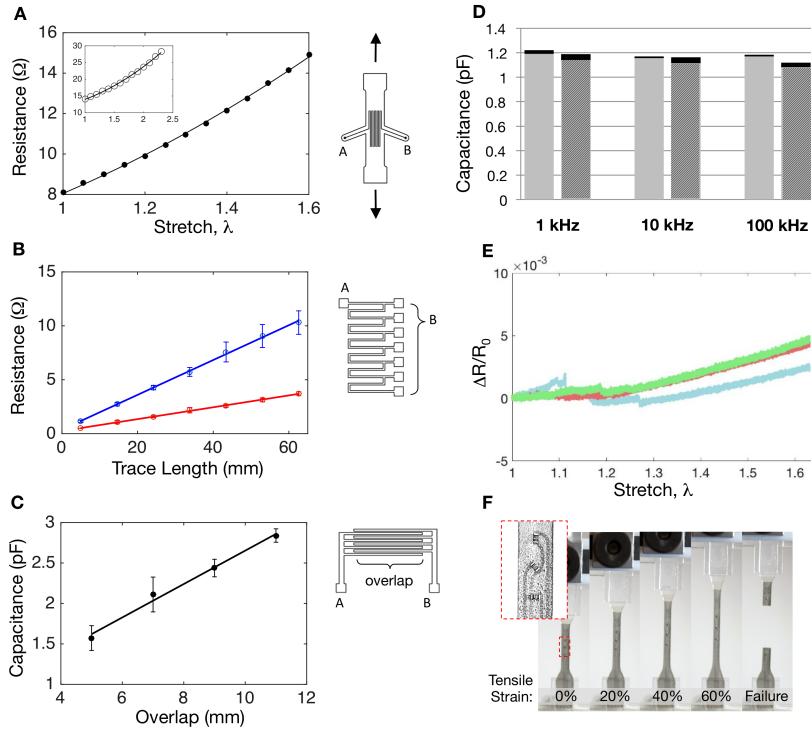


Figure 3.5: UVLM patterned planar resistors and capacitors. (A) Experimental measurements (markers) and theoretical fit (curve) for electrical resistance versus stretch for serpentine LM trace (120 mm length, 0.5 mm width); inset: measurement of laser-patterned LM trace on a soft polyacrylate substrate (VHB tape; 3M). (B) Resistance versus trace length for 100 (red) and 200- $\mu\text{m}$  wide (blue) traces. Markers and curves correspond to experimental measurements and theoretical fit, respectively. (C) Experimental measurements (markers) and theoretical fit (curve) for capacitance versus overlap length of interdigitated LM traces (250  $\mu\text{m}$  width, 150  $\mu\text{m}$  spacing). (D) Average capacitance of comb capacitors patterned with (gray) UVLM and (hatched gray) stencil lithography for various testing frequencies. The black bars are the standard deviation ( $N = 9$ ). (E) Plot of change in electrical resistance versus stretch for surface mount resistors oriented at 0 degrees (blue), 45 degrees (red) and 90 degrees (green). (F) Photographs of sample when strained (0%, 20%, 40%, and 60%) and after failure. *Inset*: Close up of sample showing placement of resistors.

### 3.3 Discussion

With the method presented in Figure 3.2, packaged SST chips can be embedded in elastomer and wired together with EGaIn interconnects that share dimensions similar to those of conventional copper PCB traces ( $\geq 50 \mu\text{m}$  (2 mil) width,  $\geq 100 \mu\text{m}$  (4 mil) spacing). The experimental results reported above show that the UV laser-patterned EGaIn traces exhibit properties that are consistent with classical predictions for electrical resistance and capacitance. However, as noted, the patterning resolution of EGaIn with UVLM is limited by excess liquid metal that remains on the surface after laser processing. This condition is confirmed by comparing SEM and EDS scans of bare zPDMS and surfaces that have been coated with EGaIn and then ablated. In particular, Dr. Lu observed a scattering of droplets with dimensions  $\sim 1\text{-}10 \mu\text{m}$  that are rich in Ga and In. Although diffusely scattered, the likelihood that these droplets induce in-plane shorting becomes significant when the spacing between circuit features is below  $100 \mu\text{m}$ .

Based on the electrical resistance measurements presented in Figs. 3.5A&B and the known resistivity of EGaIn, Ohm's Law was used to infer trace thickness. For a volumetric resistivity of  $29.4 \times 10^{-8} \Omega \cdot \text{m}$ <sup>[29]</sup>, the nominal thicknesses was measured and ranged from 16.3 to 27.1

$\mu\text{m}$  with no correlation to trace width or pattern geometry. This is roughly consistent with the  $17.8 \mu\text{m}$  average thickness measured for an EGaln-coated sample that was frozen with liquid nitrogen and then shattered to expose its cross-section for image analysis Figure 3.6. The variation in film thickness is attributed to the non-uniform thickness of the EGaln film prior to UVLM patterning. While not a critical factor for circuit functionality, the deposition method could be improved to ensure a more uniform distribution and tighter control on EGaln film thickness. One possible solution is to adopt the atomized spraying technique introduced by Jeong, Hjort, & Wu in which LM alloy is deposited using an airbrush and pressure regulator<sup>[57]</sup>.

From the slope of the fitted curve in Figure 3.5C, the effective relative permittivity of the zPDMS substrate can be approximated as  $\epsilon_r \approx 5.6$ . This calculation is based on a theoretical prediction for the capacitance of interdigitated electrodes introduced by Gevorgian et al.<sup>[39]</sup> (see Section 7.2). This relatively large permittivity is likely a result of the EGaln-coated ferromagnetic  $\mu$ -spheres, which induce an “artificial dielectric” effect<sup>[106]</sup> within the elastomeric matrix.

As shown in Figure 3.5D, capacitance measured with electrodes deposited using stencil lithography ( $1.13 \pm 0.05 \text{ pF}$ ;  $N = 9$ ) is statistically similar to that for the laser-processed electrodes ( $1.19 \pm 0.03 \text{ pF}$ ;  $N = 9$ ). The small discrepancy could be related to additional contributions to the artificial dielectric effect from EGaln residue that remains after laser ablation. Regardless, such a dielectric enhancement will not influence circuit functionality since the composite remains as an electrical insulator within the plane. This is confirmed by the low dielectric loss tangent, which remains well below 0.1 for the 1 and 10 kHz measurements. It should also be noted that unlike in typical circuits, the substrate on which the LM is patterned is electrically anisotropic, with enhanced permittivity in the plane and conductivity through the thickness.

As shown in Figure 3.5E, the soft-matter PCB is capable of being stretched with a tensile strain of greater than 60%. The device fails at 62.7% strain due to mechanical failure within the center of the sample. During the experiment, all three resistors experience less than 0.6% change in resistance. It is significant to note that the strain limit is governed by mechanical rather than electrical failure. This suggests that a higher strain limit may be possible by selecting a more elastic substrate, such as VHB tape (see Figure 3.5A inset).

The layout and fabrication process presented in Figure 3.2 is used to produce several representative circuits that integrate UVLM-patterned traces of EGaln with packaged SSTs (Figure 3.7). This includes an array of surface mounted LED and  $331\Omega$  resistor chips (Figure 3.7A; Figure 7.2). A soft-matter bioelectronic circuit was also fabricated for

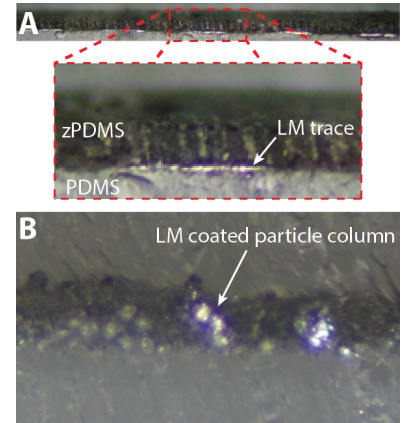
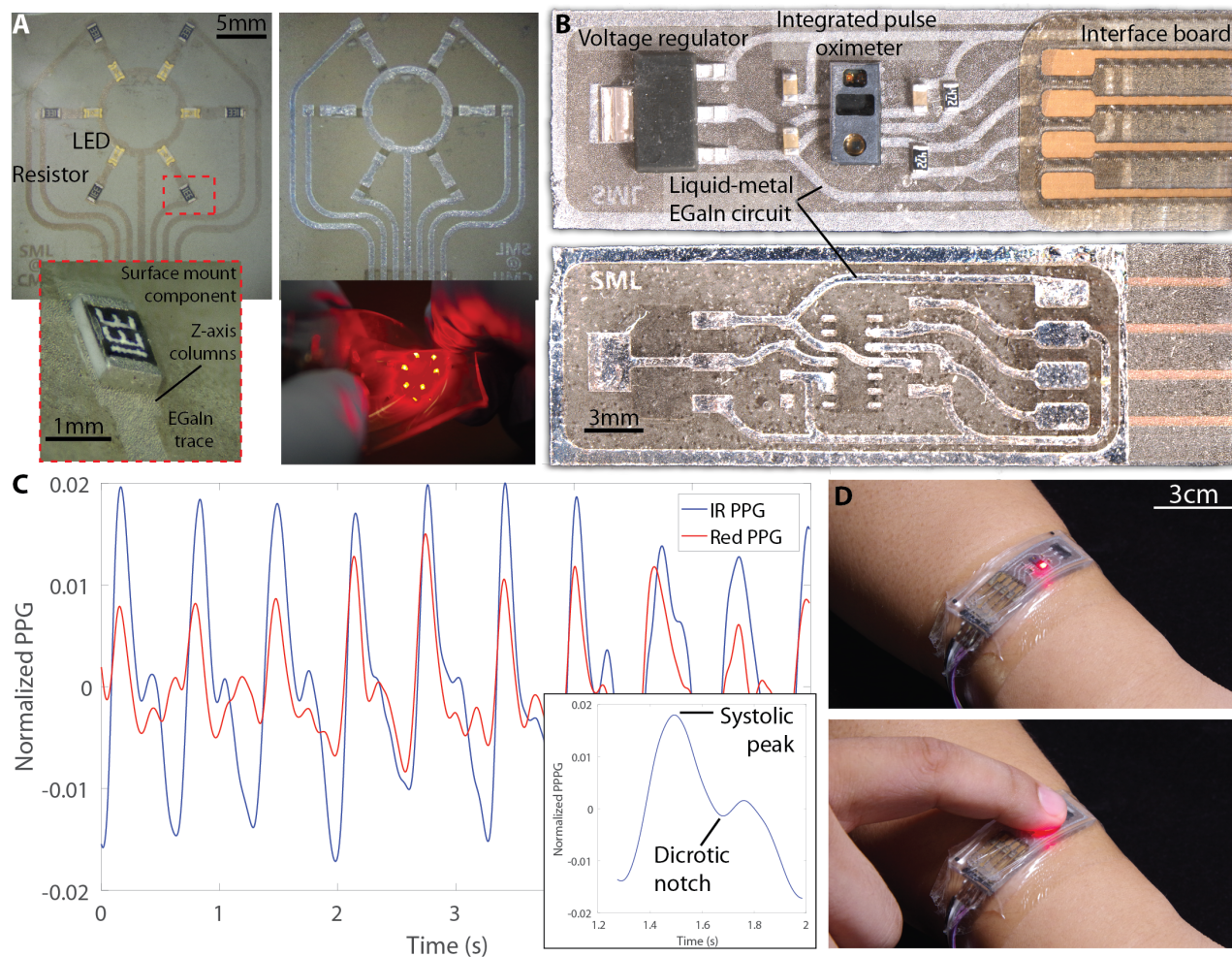


Figure 3.6: Cross section photographs. (A) The reflecting white regions represent EGaln traces and the dark region represents the zPDMS layer. The image analysis algorithm classifies different materials based on RGB and HSV values, counts the number of pixels labeled as EGaln, calculates average number of pixels in trace thickness, and converts the average thickness into metric unit. The average EGaln thickness measured is  $17.8 \mu\text{m}$ . (B) Micrograph of zPDMS cross-section shows that Ag- $\text{Fe}_2\text{O}_3$  particles are coated with EGaln and that liquid bridging between particles can be observed.



non-invasive measurements of heart rate (HR) and arterial blood oxygenation ( $\text{SpO}_2$ ). Referring to Figure 3.7B, the circuit contains an integrated pulse oximetry unit (MAX30100; Maxim Integrated Products, Inc.) that houses a red and IR LED, photodetector and optics, and a low-noise analog signal processor for reflective PPG waveforms (see Section 7.2). A flex PCB with Cu traces is used as an interface board that connects the circuit to a battery-powered Bluetooth module that transmit signals to a host computer for signal processing<sup>[100]</sup>. The device is configured to collect the PPG waveforms at 200 Hz using LED pulse widths of 400  $\mu\text{s}$  and a current of 20.8 mA (Figure 3.7C). With appropriate filtering and calibration, the waveforms can be used to obtain HR from spacing of Systolic peaks and  $\text{SpO}_2$  by comparing the amplitude (i.e. optical reflection) of IR and red light, which are absorbed differently by oxygenated or deoxygenated hemoglobin within

Figure 3.7: Soft-matter printed circuit board implementation. (A) Top and bottom of a circuit containing a circular array of LEDs; (A) inset, bottom left: close up of interface between resistor and EGaln trace; (A) inset, bottom right: soft-matter LED array undergoing deformation during operation. (B) Top and bottom of soft-matter pulse oximeter circuit. (C) PPG waveform recorded from soft-matter pulse oximeter shown in (B); (C) inset: magnified view of single cardiac beat from the measured PPG waveform. (D) Possible implementation of soft-matter pulse oximeter worn as wristband. PPG waveform can be recorded by placing finger on top of wristband while applying light pressure.

arterial blood<sup>[115]</sup>. Because the circuit board is intrinsically soft and deformable, the pulse oximetry band can wrap around the wrist and form intimate contact with skin with limited interfacial pressure (Figure 3.7D).

### 3.4 Outlook

Here, in collaboration with Dr. Tong Lu and Yichu Jin, I report a novel layout and processing technique using UV laser micromachining to produce soft and deformable circuits with liquid metal interconnects. In order to match the mechanical properties of soft natural tissue, the relatively stiff materials typically used in existing PCBs (metal wiring, soldered connections, and glassy polymer substrate) are replaced with liquid-phase metal alloy and elastomer. This biomechanically compatible “soft-matter” PCB is rapidly produced ( $\sim 3$ h) using the same commercial UVLM system (Protolaser U<sub>3</sub>) used for conventional electronics prototyping. Since the circuit is composed entirely of soft and deformable materials, fabrication does not depend on a limited selection of geometric patterns or the specialized microfabrication techniques required for thin-film metal circuits with deterministic architectures. In this respect, the proposed approach represents a relatively inexpensive, scalable, and user-accessible alternative that complements previous achievements in stretchable and thin-film electronics based on cleanroom lithography.

The intrinsic compliance of the soft-matter PCB is of particular importance in wearable bioelectronics and computing. For these applications, mechanical impedance mismatch can constrain natural body motion or cause irritation, discomfort, or tissue damage due to interfacial stress concentrations. Impedance matching is especially critical in optical or electrode-based bioelectronics applications, such as pulse oximetry, that depend on intimate contact with the skin for accurate physiological measurements. Incorporating soft materials, solid-state microelectronics, and processing steps into a single UVLM-based fabrication method enables the rapid production of customizable wearables. Such systems could be user/patient-specific and capable of physiological sensing for activity, fitness, and health monitoring.

While UVLM provides a method to rapidly create soft-matter PCBs, there remain plenty of opportunities for further exploration and improvement. In this study, characterization was limited to the z-axis elastomer substrate. Additional studies are required to understand the influence of substrate material on EGaIn wetting and ablation. It is also worthwhile to examine non-subtractive fabrication techniques that are compatible with conventional circuit printing. While UVLM processing is well established for PCB prototyping, it has considerably

higher material waste than ink-jet printing and other additive techniques. Lastly, LM-based PCBs provide significant improvements in device functionality as a function of stretch, however their compliance make the circuits more susceptible to damage. Therefore, progress requires addressing this paradox of electronics that are soft and deformable but also resilient to tearing or puncture to produce devices that have practical use for wearable computing, soft robotics, and long-term health monitoring.



## 4

# *Autonomously Self-Healing Soft-Matter Electronics and Robotics*

**E.J. Markvicka, M.D. Bartlett, et al., Nature Materials, 2018<sup>[101]</sup>**

Recent advances in mechanics and materials have made it possible to produce soft and deformable circuits that exhibit the electronic functionality of conventional, rigid printed circuit boards but match the mechanical properties of soft, natural biological tissue. However, these soft-matter counterparts are increasingly susceptible (as compared to their rigid counterparts) to varying forms of mechanical damage such as cutting, tearing, or puncture that can result in operational failure. This limitation greatly prohibits the use of soft electronics in applications such as remote teleoperation, autonomous field robotics, or medical implants where repair is challenging or impossible. While rigid substrates and packaging can be used to mitigate damaging stress concentrations in traditional electronics, such encapsulation will interfere with the elasticity of soft circuits. Instead, further advancements within these emerging fields depends on new classes of soft electronic materials that, like natural skin or nervous tissue, are self-healing and remain functional even as material is torn, ruptured, or removed.

This work was completed in collaboration with Prof. Michael Bartlett (equal contribution) and Xiaonan Huang, under the supervision of Prof. Carmel Majidi.

### *4.1 Background*

In recent years, there has been exciting progress in the development of soft electronics that are capable of self-healing or that can be repaired when damaged to restore electrical functionality. These include semiconducting polymers<sup>[120]</sup>, conductive polymer networks<sup>[151,168,179]</sup>, ionic hydrogels<sup>[13]</sup>, LM microcapsules patterned on gold lines<sup>[8]</sup>, and LM microfluidics<sup>[125,83]</sup>. Although promising, these existing methods have at least one of several limitations: (i) extended period of functional loss during self-repair, (ii) need for manual reassembly, (iii) dependency on external or redundant electronics for damage detection and circuit restoration, (iv) need for external energy sources such as heat, light,

or mechanical energy, and (v) dependency on non-ambient conditions such as increased relative humidity or temperature. Overcoming these limitations has the potential to dramatically improve longevity, performance, and functionality of deformable electronic materials.

## 4.2 Fabrication Methodology

Here, in collaboration with Prof. Michael Bartlett and Xiaonan Huang, I introduce a material architecture and framework for creating circuit interconnects that are capable of autonomous, electrical self-healing. The soft and highly deformable material is composed of droplets of Ga-based liquid metal (LM) alloy (gallium-indium, eutectic; EGaIn) embedded in a soft, silicone elastomer. In its natural (original) state following synthesis, this composite is electrically insulating, even for high LM volume fractions ( $\phi \geq 50\%$ ). However, application of extreme local pressure causes the LM droplets to rupture and coalesce to form locally conductive pathways with high electrical conductivity ( $\sigma = 1.37 \times 10^3 \text{ S}\cdot\text{cm}^{-1}$  for  $\phi = 50\%$ ; Figure 4.1a,b). This mechanically-controlled response enables circuits to both be created and subsequently reconfigured when damage is induced, through the autonomous, in-situ formation of new electrical pathways. This self-repairing property is demonstrated in Figure 4.1c, which shows how a 4-channel serial clock display continues to operate as the power, data, and clock lines undergo extreme mechanical damage, including cutting, tearing, and the complete removal of material. This extraordinary resilience is possible through the mechanism illustrated in Figure 4.1b, which shows how damage induces the formation of new droplet-droplet connections that reroutes the electrical conductor around the damaged region.

Previous LM-elastomer systems have focused on microfluidic circuits and liquid metal embedded elastomers (LMEEs) through dispersions of LM droplets, drop-casted LM films, or backfilled cellular structures<sup>[125,83,10,113,87,33,6,128,156,5,86,159]</sup>. For the case of microfluidic circuits, self-healing has been demonstrated but conductivity is temporarily lost and may require manual intervention to restore function<sup>[125,83]</sup>. Previous efforts in LMEE synthesis<sup>[10,113,87,33,156,5,86,56]</sup> resulted in material compositions and microstructures that only achieved electrical conductivity at very high volume loadings  $\phi \geq 50\%$  (if at all) and did not exhibit autonomous self-repair. In addition, light pressure ( $<100 \text{ kPa}$ ) could form conductive networks by “mechanical sintering” LM nanoparticle films, and general handling may lead to unintended activation between neighboring traces, resulting in electrical failure.<sup>[113]</sup> Although not soft or stretchable, autonomous self-healing had been previously demonstrated using LM droplets embedded in

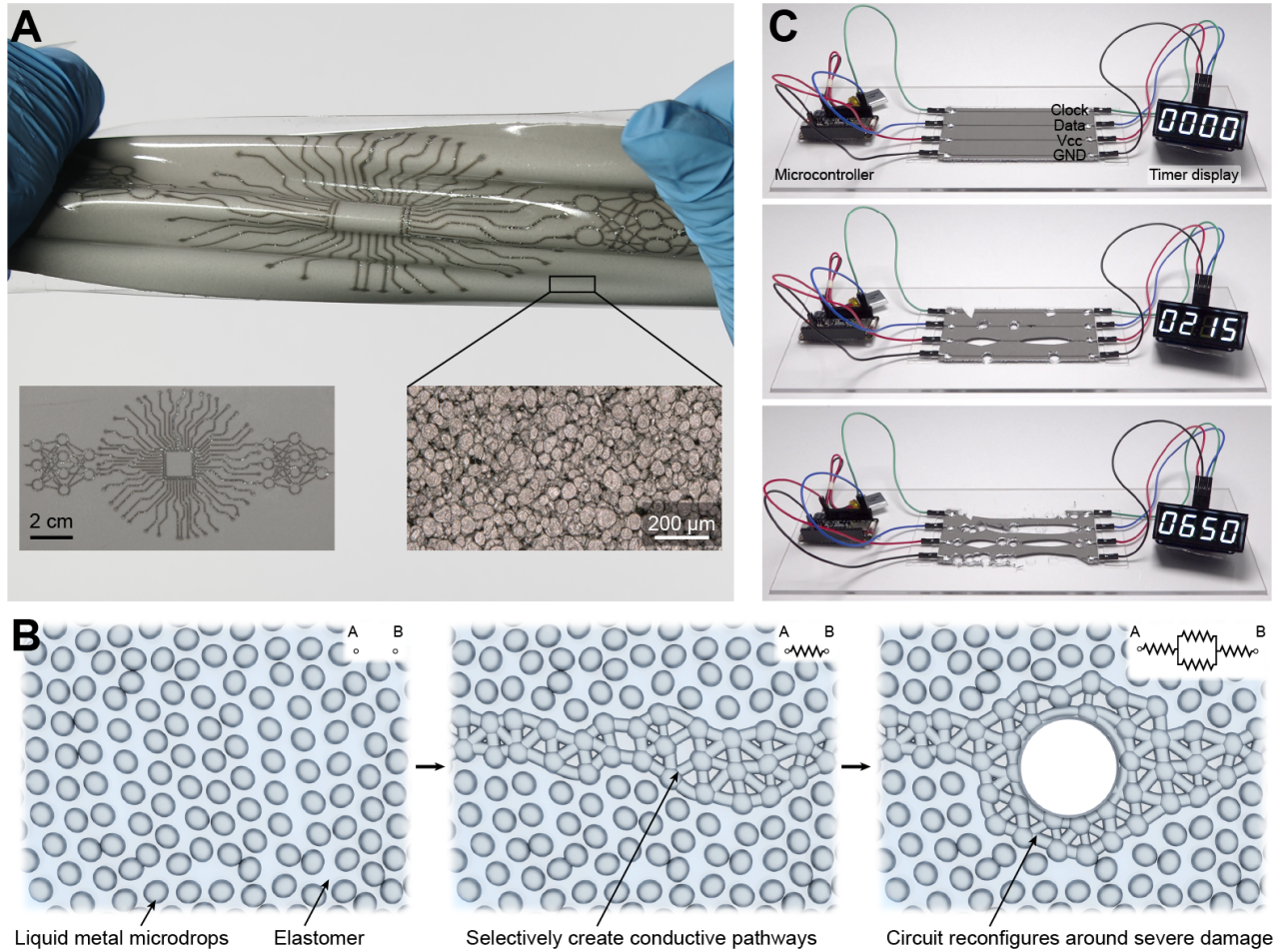
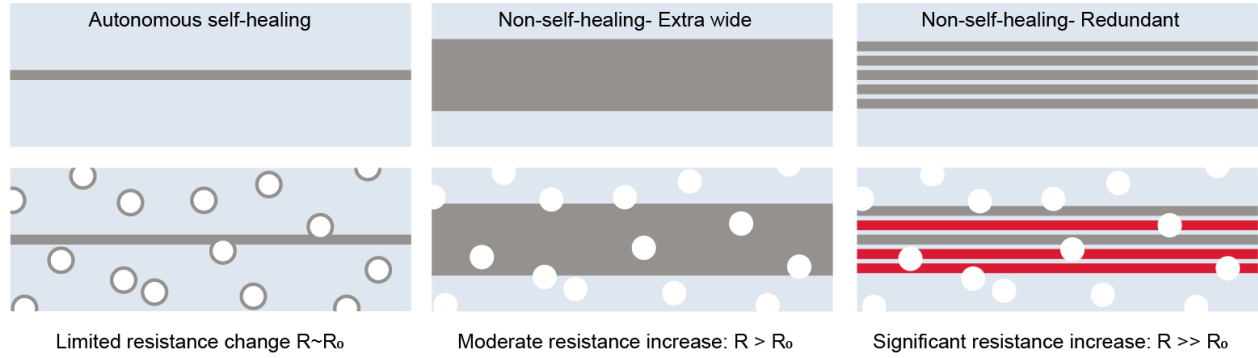


Figure 4.1: Self healing soft matter composite. (A) A LM-elastomer composite being stretched and twisted with an intricate design of electrically conductive traces. Lower left is the undeformed sample and lower right is an optical micrograph showing the LM microdroplets in elastomer at  $\phi = 50\%$ . (B) Schematic illustration of the self-healing mechanism where an initially insulating composite is selectively compressed to create electrically conductive LM traces. Upon damage, the LM trace autonomously reconfigures and maintains electrical conductivity. (inset) Equivalent electrical circuit schematic. (C) Example of the reconfigurable material ( $\phi = 50\%$ ) transmitting DC power (Vcc, GND) and digital communication signals to operate a counter display. As severe damage is induced the counter maintains operation, which requires all four traces to constantly maintain electrical conductivity.

rigid materials ( $E > 2.8$  GPa), however conductivity is initially interrupted after damage and self-healing was limited to a single event as the LM is depleted during healing<sup>[8]</sup>.

By combining recent work on liquid metal, fluidic self-healing, and mechanical sintering, I was able to demonstrate a soft, stretchable circuit that is electrically stable under typical operational loading conditions but capable of instantaneous electrical self-healing under multiple, extreme damage events. In contrast to previous work, the material composition and LM microstructure presented here is naturally robust to inadvertent activation that could lead to electrical shorting. Since the LM droplets are dispersed in an elastomeric phase instead of a continuous particle film, significant stress shielding is provided that protects the circuit from unintended activation. Furthermore, by exhibiting an autonomous and instantaneous response, our electrical wiring is uniquely capable of continuous functionality when subject to



the sparse and localized but spatially random damage that frequently occurs in real-world applications. When compared to non-self-healing circuits with redundant or extra-wide traces, this self-healing architecture provides circuit interconnects that have a smaller footprint, which is statistically less likely to be damaged, and exhibit a limited drop in electrical conductivity even when damage has occurred (Figure 4.2). Furthermore, the addition of a thin elastomer sealing layer after fabrication (Figure 4.10) or selective patterning (Figure 4.3) can be used to protect the underlying circuit and help alleviate unintended activation between neighboring traces.

Figure 4.2: Schematic of various damage mitigation strategies. From left to right: (i) the new autonomous self-healing damage mitigation strategy presented here. (ii) A non-self-healing trace that is significantly wider than the expected damage size to prevent failure. (iii) Redundant non-self-healing traces to reduce the probability of failure.

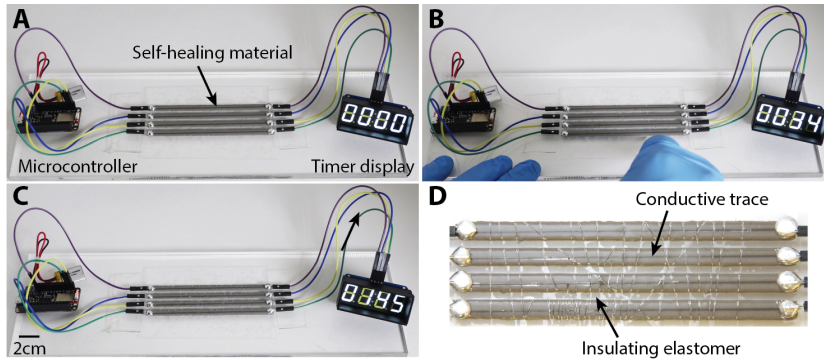


Figure 4.3: Self-healing of close-neighboring traces,  $\phi = 50\%$ . (A)-(C) Photograph sequence of the selectively patterned LMEE composite (8 mm trace spacing, 2 mm insulating spacing between selectively patterned composite) undergoing mechanical damage from a razor blade. The material is selectively reconfigured and maintains operation under extreme damage without shorting. (D) Top-down photograph of selectively patterned LMEE after damage.

### 4.3 Liquid Metal-Elastomer Composite

The self-healing material is composed of EGaIn microdroplets (75% Ga, 25% In by weight; Solution Materials, LLC) dispersed in a soft silicone elastomer (Sylgard 184; Dow Corning). EGaIn is selected as the liquid filler due to the combination of high electrical conductivity, low viscosity, and non-toxic characteristics<sup>[29,17]</sup>. The composite is fabricated by mechanically mixing a range of LM loadings from  $\phi =$

20 to 50% with uncured elastomer, creating a dispersion of generally ellipsoidal particles on the order of  $50 \mu\text{m}$  (Figure 4.4). After initial fabrication, the solid-liquid hybrid composite is electrically insulating due to a lack of percolating networks and the presence of an insulating oxide skin that develops on the surface of the LM droplets.

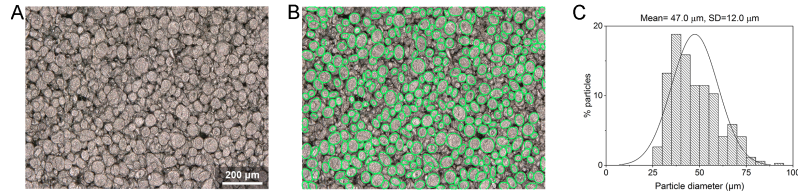


Figure 4.4: Particle size analysis of LMEE composite,  $\phi = 50\%$ . Optical micrograph (A) and overlay of ellipses fit to the particles (B). (C) Histogram of the percent of analyzed particles versus major radii.

#### 4.4 Trace Patterning

Application of local pressure induces the formation of conductive pathways, which are created as LM droplets rupture to form percolated networks. These pathways are internal to the composite and can function as traces for power and data transmission within elastomer-embedded soft circuits. Since the remaining material is unaffected, multiple traces can be constructed that are electrically insulated from each other. To create a patterned circuit, I utilize a X-Y pen plotter (Explore, Cricut) that enables intricate circuit designs to be digitally created and implemented rapidly in a maskless fabrication approach (see Appendix 7.3). For the current approach, circuit designs require a 2.5 mm center-to-center spacing to prevent unintended shorting between adjacent,  $500 \mu\text{m}$  wide traces (Figure 4.5). The goal of this material architecture and framework is not to create high-density electrical interconnects between closely spaced microelectronic chips. That is because extreme material damage would likely lead to the permanent destruction or removal of these components. Instead, the purpose is to introduce electrical wiring (e.g. power, data, clock lines) that extends  $\sim 0.01$ -1 meters and maintains conductivity when the host material is damaged by randomly distributed tears, cuts, or punctures.

#### 4.5 Electromechanical Characterization

The electrical resistance as a function of trace length was characterized for LM volume loadings of  $\phi = 20$  to  $50\%$ . The  $\phi = 50\%$  sample exhibits the highest electrical conductivity (conductivity:  $\sigma = 1.37 \times 10^3 \text{ S}\cdot\text{cm}^{-1}$ , resistivity:  $\rho_0 = 9.23 \times 10^{-6} \Omega \cdot \text{m}$ ) across this range and maintains a constant conductivity (assuming a constant cross-sectional area)

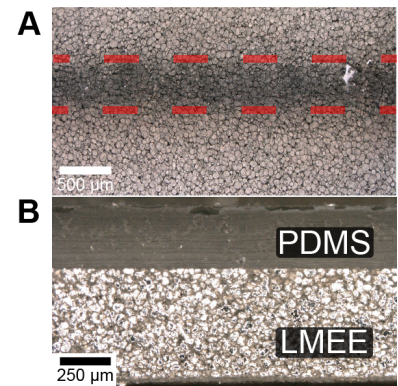


Figure 4.5: Conductive trace dimensions. Micrographs of a representative sample that was used to measure the area of the conductive trace to calculate volumetric electrical conductivity. (A) Top-down micrograph of a conductive trace drawn on the LMEE composite  $\phi = 50\%$ . The red lines indicate the boundaries of the trace width ( $w = 500 \mu\text{m}$ ). (B) Micrograph of the cross section of the LMEE composite  $\phi = 50\%$  ( $t = 550 \mu\text{m}$ ).

making it useful for various functions within electronic circuits (Figure 4.8a). The voltage across a conductive trace was then monitored as current was sourced. The material exhibits a linear I-V response (constant resistance) up to 1 V for all volume loadings of liquid metal (Figure 4.8b). As the applied power is increased (up to 5 amps), Figure 4.8b inset shows a small increase in absolute resistance as a function of applied power for a  $\phi = 50\%$  sample. This deviation in absolute resistance is likely due to the decrease in volumetric conductivity as the local temperature of LM (temperature coefficient of gallium,  $\alpha = 0.004$ ) increases due to Joule heating, where  $\Delta\rho = 1.63 \times 10^{-6} \omega \cdot \text{m}$  corresponding to a relative change of  $44^\circ\text{C}$ ,

$$\Delta T = \Delta\rho / \alpha\rho_0.$$

The LM-elastomer composite is shown to be soft (elastic modulus  $\simeq 0.8$  MPa) and exhibits low hysteresis elasticity after the first loading cycle when loaded up to 50% strain for 1,000 loading cycles (Figure 4.8c). Extended cyclical loading was performed for 1 million cycles up to 40% tensile strain, which is below the strain limit of the composite. Prior to mechanical failure, there is no loss in electrical conductivity (Figure 4.6). As shown in Figure 4.7, the trace exhibits little change in electrical resistance over the course of the 1 million loading cycles.

Electro-mechanical coupling is examined by measuring the electrical resistance as a function of uniaxial strain. Each volume loading is cycled to 50% strain for 1,000 loading cycles. As shown in Figure 4.8e, a small increase in normalized resistance is evident in the initial extension for the first loading cycle for all volume loadings. However, when returning to the undeformed length, the resistance decreases below the original, undeformed value for all samples. Upon subsequent loadings, the 50% sample exhibits a stable response for 1,000 loading cycles, while the 20-40% samples actually show a reduction in normalized resistance. In all cases, upon stretching to 50% strain the maximum increase in resistance is less than 10% (Figure 4.8d). I hypothesize that when the material is strained, the liquid metal within the droplets flows into the connecting pathways between droplets, reducing the electro-mechanical coupling effects. This behavior contrasts sharply from traditional incompressible, stretchable conductors, where the normalized trace resistance ( $\Delta R/R_0$ ) should increase as  $\lambda^2 - 1$ , or  $1.25\times$  at 50% strain, where stretch ( $\lambda$ ) is defined as the ratio of the final length and the initial length ( $\lambda = L/L_0$ )<sup>[73]</sup>. Such a characteristic increase in circuit resistance is undesirable for most circuit applications, where even more extreme increases are observed in soft-matter systems that utilize conductive particle-filled elastomers and soft copolymer blends. These results show the robust and reliable nature of the self-healing composite, displaying high electrical conductivity and

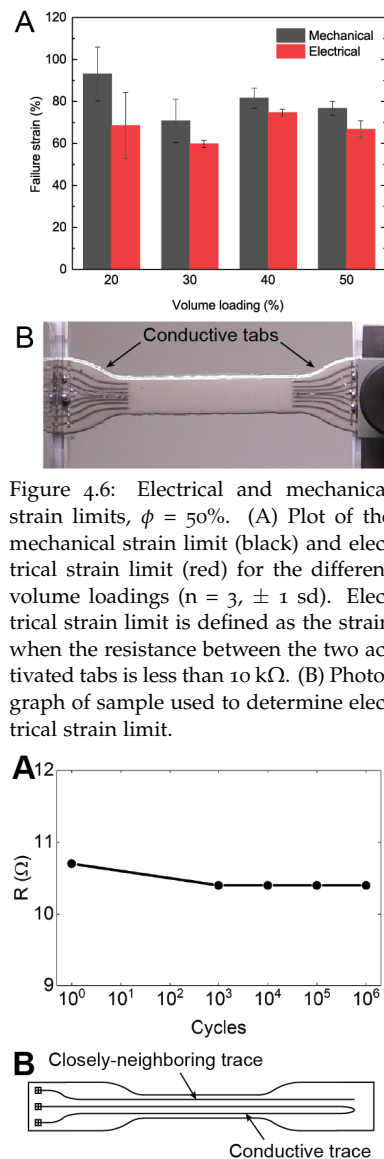


Figure 4.6: Electrical and mechanical strain limits,  $\phi = 50\%$ . (A) Plot of the mechanical strain limit (black) and electrical strain limit (red) for the different volume loadings ( $n = 3$ ,  $\pm 1$  sd). Electrical strain limit is defined as the strain when the resistance between the two activated tabs is less than 10 k $\Omega$ . (B) Photograph of sample used to determine electrical strain limit.

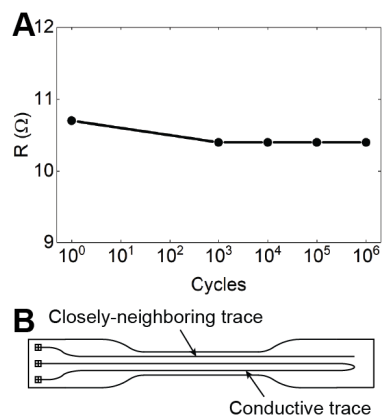


Figure 4.7: Extended cyclic loading up to 1 million cycles (A) Schematic illustration of the ASTM D412 die A dogbone sample and the conductive and closely-neighboring trace. (B) The resistance of the conductive trace for each decade as a function of loading cycle.

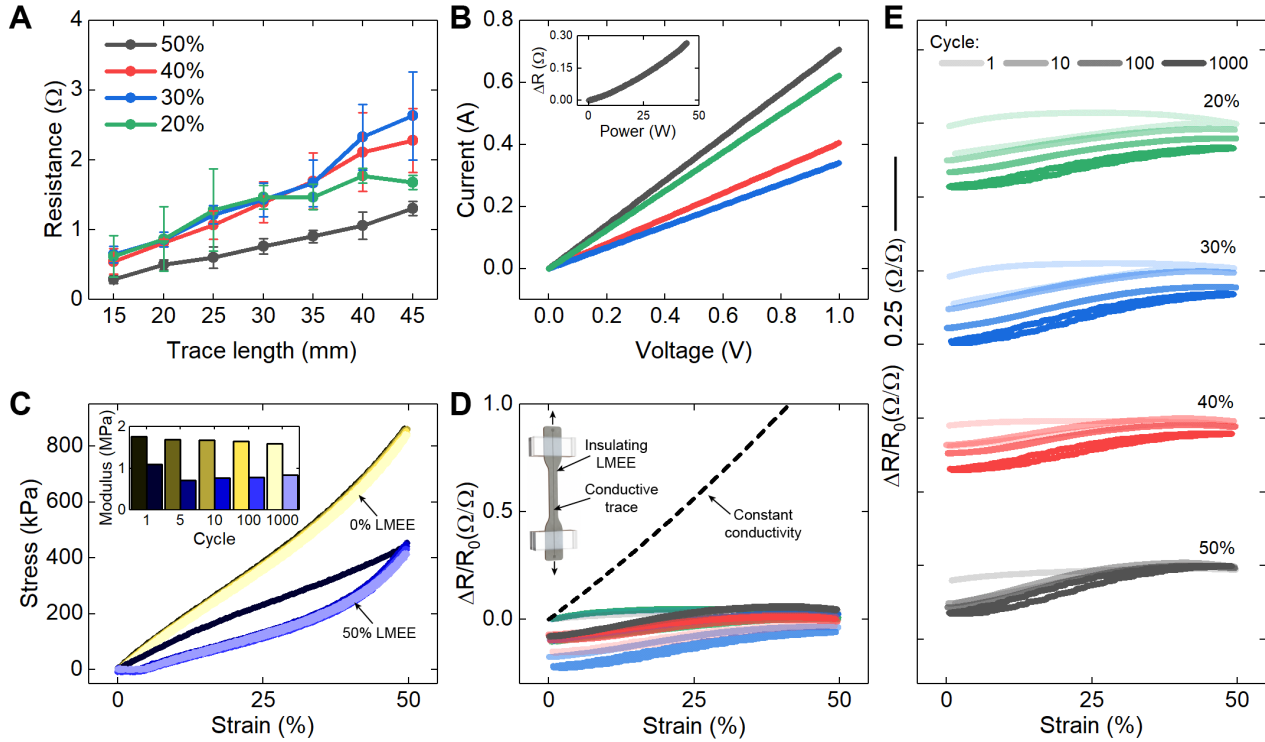


Figure 4.8: Electrical and mechanical characterization. (A) Resistance as a function of trace length for four different volume loadings ( $\phi = 50, 40, 30, 20\%$ ). The error bars are the standard deviation ( $N = 3$ ). (B) Current-voltage curves up to 1 volt for a 45 mm trace ( $\phi = 50, 40, 30, 20\%$ ) and (inset) absolute change in resistance as a function of applied power as 5 amps is sourced to the  $\phi = 50\%$  sample; refer to legend in (A). (C) Stress versus strain under uniaxial cyclic loading to 50% strain for  $\phi = 0\%$  and  $\phi = 50\%$ , up to 1,000 cycles. (inset) Modulus as a function of loading cycle. (D) Normalized resistance as a function of strain ( $\phi = 50, 40, 30, 20\%$ ) and theoretical prediction using ohm's law for an incompressible solid with fixed volumetric resistivity; refer to legend in (A) for volume loading and (E) for cycle. (E) Normalized resistance as a function of strain ( $\phi = 50, 40, 30, 20\%$ ); note y-axis offset is applied to each volume loading to assist in visualization of data.

mechanically robust functionality over repeated loading cycles.

#### 4.6 Material Encapsulation

To provide further protection from non-damaging, environmental conditions (e.g. contact pressure, shear forces, folding), the composite can be encapsulated within an elastomer sealing layer to help prevent or completely eliminate ( $t \geq 5\text{mm}$ ) further trace formation that results in undesired activation between closely-neighboring traces (Figure 4.10a). To experimentally characterize the electrical stability of the device under contact pressure, a glass cylindrical indenter was positioned across two closely-neighboring traces and pressed into the composite ( $\phi = 50\%$ ,  $t = 500\ \mu\text{m}$ ) until undesired activation occurred (see Appendix 7.3). The thickness of the self-healing composite has a negligible influence on the activation pressure (Figure 4.9). Furthermore, the composite is capable of withstanding repeated compressive loads of 35 N ( $p_{max} = 1.32\ \text{MPa}$ ) for 1,000 loading cycles without unintended activation occurring for a  $\phi = 50\%$  sample with 1 mm encapsulation layer (see Appendix 7.3). Conversely, the highest localized pressure under the foot during walking of young adults is  $\sim 0.33\ \text{MPa}$ <sup>[52]</sup>. This indicates that walking pressure would not be sufficient to activate the

composite in the most vulnerable situation. As experimentally demonstrated with a thin elastomer sealing layer ( $t = 1$  mm), the self-healing circuit ( $\phi = 50\%$ , 2.5 mm trace spacing) is capable of undergoing normal walking conditions for 31 steps with 10 footwear variations without any unintended shorting between traces for a digital clock (Figure 4.10b).

To further investigate unintended trace formation from non-damaging surface tractions, the device was experimentally characterized using a single lap shear joint (Figure 7.4). The device remained electrically stable without an encapsulation layer under a maximum shear stress of  $\sim 0.24$  MPa. The device can also endure surface abrasion when encapsulated with a thin elastomer sealing layer ( $t = 1$  mm; Figure 7.5). Further quantitative shear stress experiments were performed, where a tangential shear force was applied to a spherical indenter that is pressed into the composite. The indenter is sheared across two closely-neighborings traces until undesired activation occurred (see Supplemental Information). The device is approximately twice as resilient to the maximum normal pressure under tangential shear when sealed with a thin elastomer layer ( $P = 0.75$  MPa,  $t = 1$  mm; Figure 7.6). Additionally, I find that the device is electrically stable up to a bend radius of 1 mm ( $1.25\times$  the overall thickness), which is comparable to flexible circuits that have a minimum bend radius of  $6\times$  to  $12\times$  the overall thickness (for 0.1 mm thick flexible circuit,  $R = 0.6$  to 1.2 mm), Figure 4.10c. Lastly, extended cyclic loading was performed to 40% strain for 1 million loading cycles, where no unintended activation occurred between two closely-neighborings traces (Figure 4.7). These results demonstrate that the device is capable of withstanding general handling and the rigors of daily use, where, in practice, conductive networks are only formed under extreme loading conditions associated with tearing, puncturing, and material removal.

#### 4.7 Damage Response

As demonstrated in Figure 4.1, the composite material is capable of being severely damaged while maintaining electrical conductivity. The self-healing response of the material is further investigated with controlled cutting and puncturing experiments. Here, I measure the resistance of a trace while mechanical damage is inflicted. First, straight cuts with a razor blade are investigated. As shown in Figure 4.10d, a minimal increase in absolute resistance ( $< 1 \Omega$ ) is observed with subsequent cuts, furthermore the material continuously maintains electrical conductivity during and after damage has occurred. As the composite is punctured, the LM droplets on the damaged surface are ruptured and a stabilizing oxide layer is formed when the gallium-based LM is

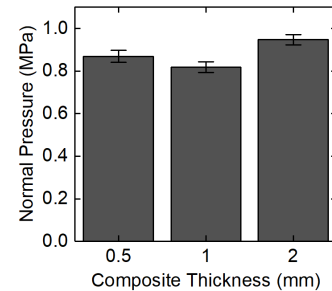


Figure 4.9: Activation pressure as a function of composite thickness. A negligible difference in activation pressure is shown for different thicknesses of the self-healing composite.

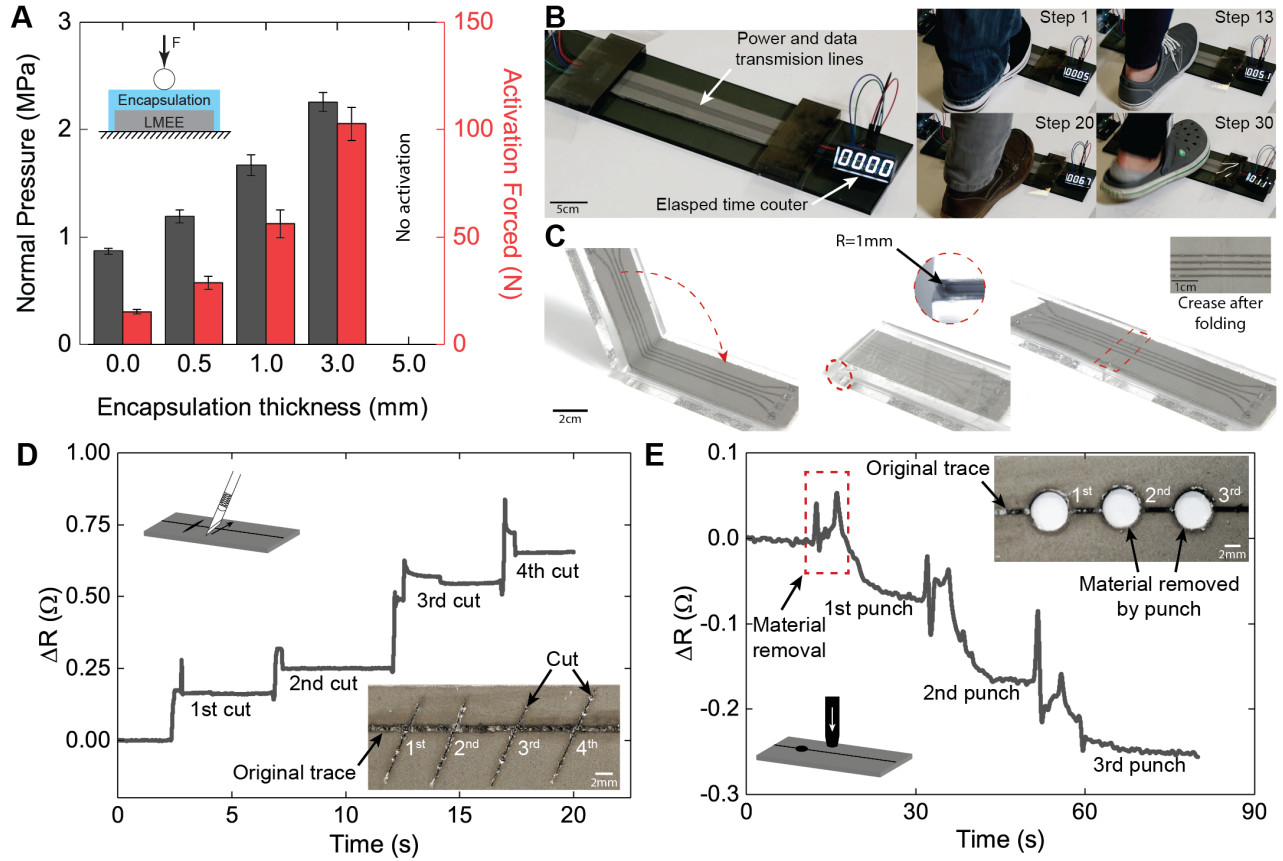


Figure 4.10: Autonomous self-healing response ( $\phi = 50\%$ ). (A) Critical activation pressure/force required to induce unintentional activation of closely-neighboring traces (5 mm trace spacing) for different encapsulation thicknesses ( $t = 0, 0.5, 1, 3,$  and  $5$  mm). The error bars are the standard deviation ( $N = 5$ ). (B) The robust nature of the material to everyday loading is demonstrated by walking across the traces of a digital clock in various types of footwear without any unintended activation. (C) Closely-neighboring traces (2.5 mm trace spacing) are electrically stable under folding up to 180 degrees with a bend radius of 1 mm. Resistance as a function of time for high aspect ratio damage from a razor blade (D) and low aspect ratio damage from a hole punch (E). Depending on the aspect ratio of the damage, the resistance of the trace can increase or decrease. During damage, the circuit is autonomously reconfigured without intervention or loss of conductivity.

exposed to oxygen, preventing unwanted flow of LM<sup>[27]</sup>. Next, a series of circular holes with perimeter  $P$  are created along the length of the trace, Figure 4.10e. Remarkably, the resistance is observed to decrease as subsequent holes are created. This counterintuitive response is due to the electrical reconfiguration of the damaged circuit (Figure 4.1b). When a piece of material with trace length  $L_t$  is removed from the circuit the original trace is replaced by two traces of length  $\alpha\pi L_t$  and  $(1 - \alpha)\pi L_t$ , where  $0 < \alpha < 1$  is the ratio of the perimeter on one side of the trace. If I assume constant resistivity and  $\alpha P(1 - \alpha) < L_t$ , the overall resistance of the circuit will be reduced, where maximum reduction occurs when the length of the perimeter is symmetric about the trace ( $\alpha = 0.5$ ). This model also predicts a rise in resistance for high aspect ratio damage, which is observed for the linear cuts in Figure 4.10e (see Appendix 7.3).

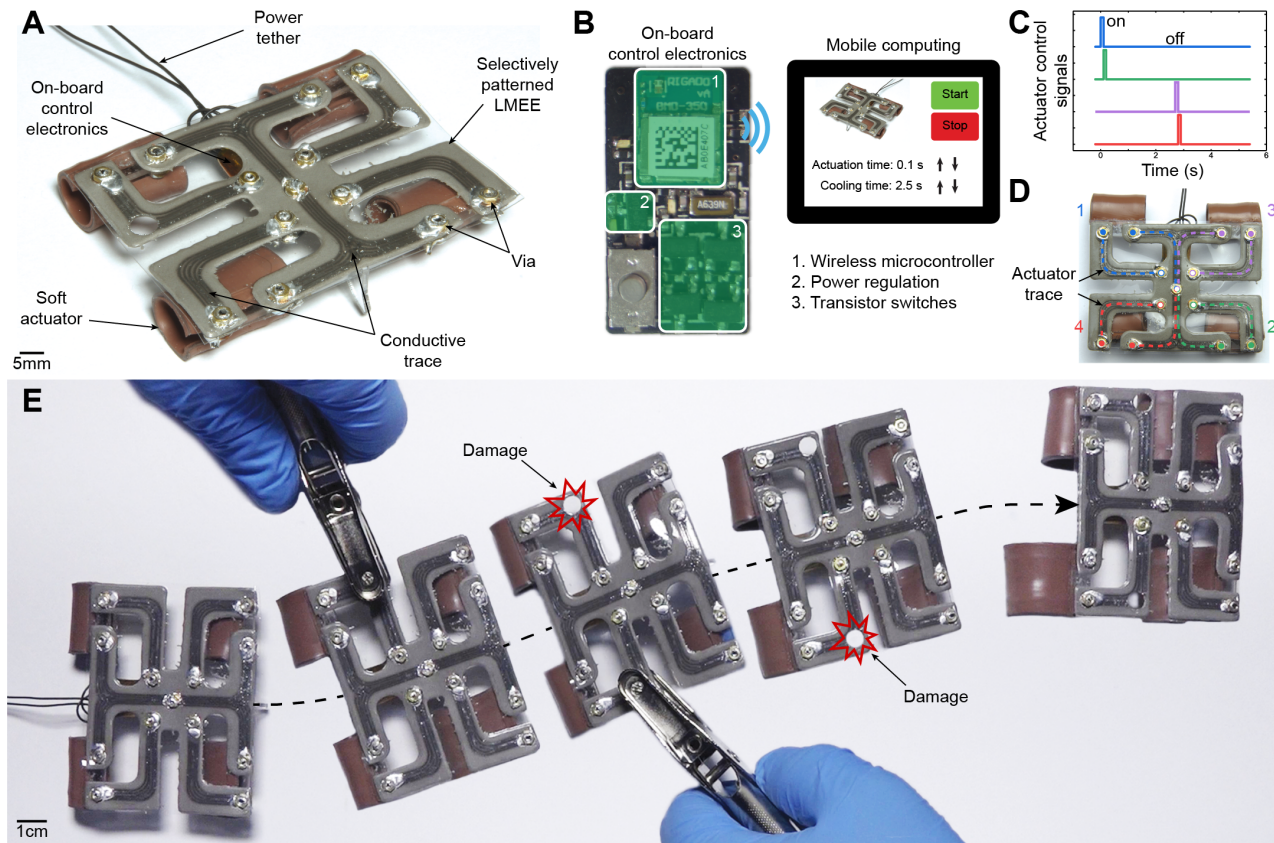


Figure 4.11: Autonomously self-healing soft robot ( $\phi = 50\%$ ). (A) A soft quadruped with autonomously self-healing soft-matter electronics. (B) The robot is controlled using a mobile computing platform that wirelessly transmits high and low level commands to on-board control electronics. (C) Actuation sequence for the soft quadruped. (D) Schematic of high-power signal routing, connecting the on-board control electronics (white filled circles) to the soft actuators (color filled circles); trace color coded with reference to (C). (E) Video frame sequence from top-down view of the soft robot traversing smooth terrain. The robot encounters puncture damage from a hole punch and the electrical pathway is autonomously re-configured around the damaged region without loss of electrical conductivity. There is no apparent change in the gait of the soft robot after damage, as the robot continues traversing smooth terrain as before without manual intervention, use of external energy sources, or redundant electronics.

#### 4.8 Soft Robotics Demonstration

This electronically self-healing material is particularly enabling for wearable electronics, soft robotics, and inflatable technologies when combined with advanced integrated circuits. To demonstrate the capabilities of the self-healing material for demanding applications, I produce a soft robotic quadruped with autonomously self-healing electrical wiring to route the power signals from the on-board control electronics to the soft actuators (Figure 4.11a). While not shown here, mechanical (structural) self-healing has been previously demonstrated within pneumatic robotic grippers<sup>[153,146]</sup>. The soft actuators used here are composed of shape memory alloy (SMA) wires embedded within thermal tape and are sequentially actuated (Figure 4.11c-d) through direct Joule heating to enable robot locomotion (see Appendix 7.3). The soft robot is powered using a lightweight tether and is wirelessly controlled from a mobile computing platform (Figure 4.11b, see Appendix 7.3). To ensure the desired actuation power signal is efficiently transported to the actuator, the effective trace width is increased by

patterning five parallel traces to each actuator. Furthermore, the soft robot is powered with a lightweight tether and is controlled from a mobile computing platform using the 4.0 Bluetooth Low Energy (BLE) wireless protocol to communicate with the on-board electronics (Figure 4.11b). Figure 4.11e shows that the resulting quadruped is capable of traversing smooth terrain and is resilient to puncture damage with no apparent change in the gait of the soft quadruped. Remarkably, the robot is able to continue traversing the smooth terrain as before without manual intervention, use of external energy sources, redundant electronics, or changes to the environmental conditions. This is especially surprising since over 50% of the width of the power trace is removed when damaged and any drastic changes in the resistance ( $\sim 5 \Omega$ ) of the circuit wiring would prevent the limb from continuing its powered actuation due to local heating of the damaged region instead of the thermal actuator. This implementation highlights the versatility of the autonomously self-healing soft-matter composite, ease of integration with complex systems, and ability to handle high currents for high power/energy demanding applications even when damage occurs.

#### 4.9 Outlook

In collaboration with Prof. Michael Bartlett and Xiaonan Huang, I have introduced a soft-matter composite for mechanically robust, electrically self-healing circuit interconnects for power and data transmission that instantaneously repairs itself under extreme mechanical damage. Circuits produced with conductive traces of this material remain fully and continuously operational even when the traces are severed, torn, or punctured or material is removed. Furthermore, if not initially activated, the composite remains electrically insulating under non-damaging environmental conditions when sealed with a thin elastomer layer. This unprecedented level of robust functionality has the potential to enable soft-matter electronics and machines to exhibit the extraordinary resilience of soft biological tissue and organisms. In addition to the self-healing response, this material exhibits a high electrical conductivity that does not change with stretch and is ideally suited for stretchable electronics with strain-invariant circuit properties and transmission of power. Moreover, it is uniquely suited as 0.01-0.1 m scale wiring (e.g. power, data, and clock lines) for applications where the damaged regions are small and sparse but randomly distributed over a large area. The circuit achieves “effective redundancy” or “widening” in an autonomous manner and only in locations where damage occurs (Figure 4.2). Such responses correspond to a limited change in overall conductivity of the electrical conductor. This

continuous and stable electrical conductivity is especially critical for power transmission but can also be important for certain types of data transmission. Lastly, the relatively simple and versatile circuit patterning approach allows for implementation in diverse applications. Nonetheless, development in the precise control of particle size, arrangement, use of surfactants to modify oxide layer properties, and composition could potentially allow for additional capabilities, such as transparency and electrical or mechanical tunability.

The electrically self-healing LM-elastomer composite provides a method for increasing the life span of stretchable electronic circuits by maintaining electrical conductivity when damage occurs. To further promote longevity, materials should be capable of electrically registering and communicating mechanical damage to enable rapid repair, before reaching an irrecoverable state. Several systems and devices have been developed for signaling or reporting damage within polymer systems at a molecular level (e.g. mechanophores<sup>[26]</sup>). However, for integration with existing control systems, new multi-functional materials are needed that exhibit an electrical response to damage. Furthermore, these materials must maintain functionality during and after extreme damage has occurred. Ultimately, next generation material systems will exhibit inherent properties to regain electrical and mechanical functionality. In practice, mechanical performance could be regained by regenerating the lost material, reforming covalent bonds, or releasing repair agents contained within embedded microcapsules<sup>[131]</sup>.

## *Damage Sensing Soft-Matter Composite*

**E.J. Markvicka et al., Under review, 2018<sup>[102]</sup>**

As mentioned in the introduction, soft-matter technologies are essential for emerging applications in wearable computing, human-machine interaction, and soft robotics. However, as these technologies leave the laboratory and interact with dynamic and unstructured environments, material and structural damage is inevitable. Current systems that detect or self-report damage depend on rigid materials to electrically, visually, or mechanically identify issues. In contrast, biological organisms use soft tissue to autonomously detect, communicate, and respond to damage and this presents an intriguing opportunity for compliant, engineered systems.

This work was completed in collaboration with Ravi Tutika, under the supervision of Prof. Michael Bartlett and Prof. Carmel Majidi.

### *5.1 Background*

In the case of damage monitoring in soft materials, where emerging applications take advantage of their soft and highly deformable nature, damage detection schemes must be mechanically compatible. Human nervous tissue provides an example of a soft material system that is capable of detecting, communicating, and responding to harmful external stimuli (Figure 5.1A). The detection of adverse stimuli is initiated from an extensive network of cutaneous and subcutaneous receptors called nociceptors<sup>[133]</sup>. The nociceptors are responsible for firing action potentials to directly relay this information to the cortex of the brain. The human body responds by activating motor pathways to move the endangered appendage away from the external stimuli. This interconnected response in biological systems has inspired a wide range of stimuli-responsive materials that adapt or respond to environmental changes including temperature, mechanical or physical, optical, and chemical<sup>[148,149,154,75]</sup>. However, these systems often lack the ability to communicate these environmental changes with other existing technologies, as these responses often occur at a molecular level.

Integrated soft materials provide a path forward to enable intel-

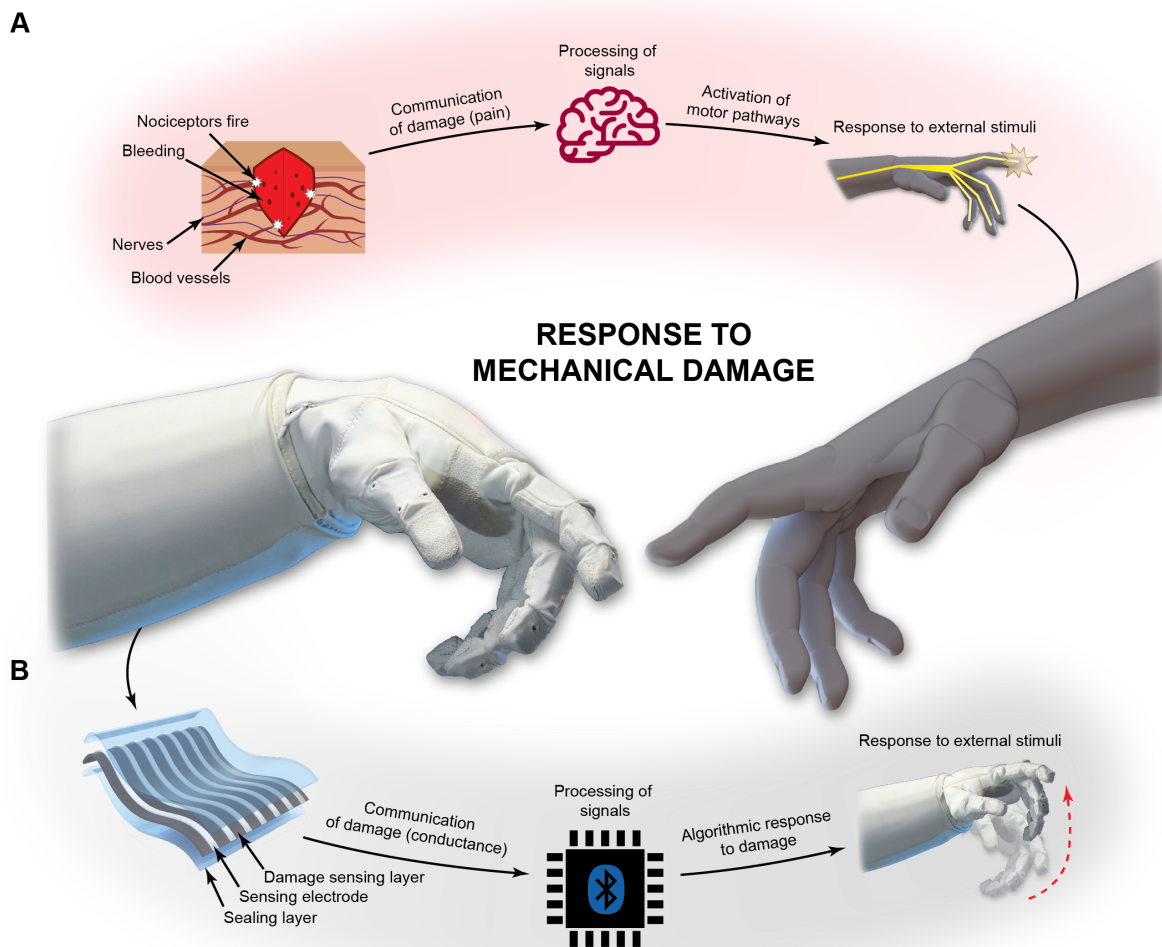
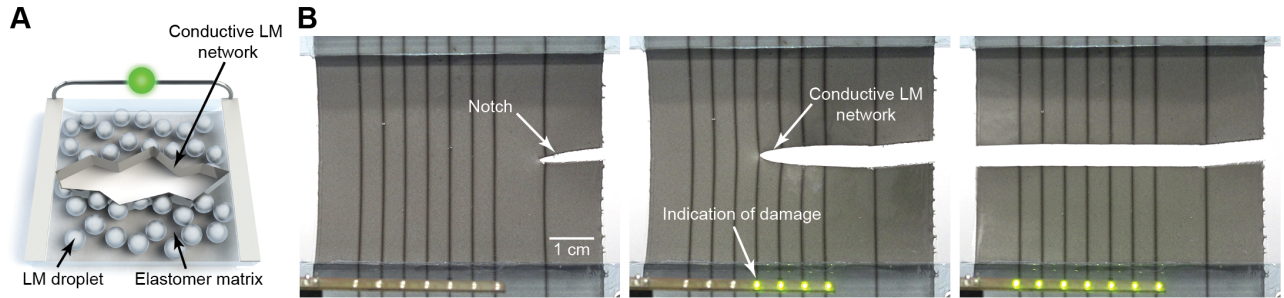


Figure 5.1: Response to mechanical damage. (A) Illustration of the human body's response to harmful external stimuli: detection (firing of nociceptors), communication (firing of action potentials), and response (activation of motor pathways). (B) Illustration of the artificial nervous tissue's response to mechanical damage: detection (local change in conductivity), communication (flow of electrical current), and response (algorithmic response).

ligent, programmable interactions between external stimuli and dynamic material properties<sup>[105]</sup>. Recently, autonomy has been incorporated in soft-matter systems through intelligent mechanical design with preplanned tasks and on-board actuation, power, and computation<sup>[164,34,121,97,7,138]</sup>. While promising, these systems lack the necessary hardware and sensing to provide critical runtime feedback to modify the preplanned task. The comprehensive system-level integration of components to enable soft-matter robotic materials to be fully self-aware of their current state still remains a significant challenge.



## 5.2 Fabrication Methodology

Here, in collaboration with Ravi Tutika and Prof. Michael Bartlett, I describe a compliant, artificial nervous tissue that can detect and localize damage (Figure 5.1B). The artificial nervous tissue is composed of liquid metal (LM) microdroplets embedded within a soft silicone elastomer matrix. In a similar manner to human skin, the underlying fluidic structures (LM microdroplets) within the synthetic tissue rupture in response to mechanical damage—compression, fracture, or puncture (Figure 5.2 A,B). Additionally, similar optical clues such as bruising or bleeding occur depending on the severity of damage. When the LM microdroplets rupture, *in situ* conductive pathways between neighboring droplets are formed. The damage initiated change in electrical conductivity can be actively detected and localized, as indicated by the illumination of the LEDs as a notch propagates through the specimen (Figure 5.2 B). This material structure provides a method for actively detecting and localizing damage within a soft-matter system, ultimately providing a path forward for achieving the longevity that is exhibited in natural, biological systems. The electrical communication of damage enables direct integration with existing control systems, providing a method for soft-matter robotic systems to initiate an algorithmic response to recover from a detrimental, external event. To demonstrate the ability to detect, communicate, and respond to a potentially detrimental event, I integrate this material structure with an inflatable soft humanoid structure, where multiple puncture events are rapidly detected, computed, and utilized in a control loop to prevent deflation and loss of functionality.

Liquid metal droplets dispersed in elastomeric systems have demonstrated extraordinary properties, including extreme toughening<sup>[63]</sup>, exceptional electrical and thermal properties,<sup>[125,83,5,6]</sup> and selective sintering for electrical trace formation<sup>[101,10,113,87,33]</sup>. The LM composite is fabricated by shear mixing LM with uncured silicone elastomer at a 1:1 volume ratio, forming a suspension of LM microdroplets (~45

Figure 5.2: Active detection of damage. (A) The damage sensing composite is composed of microdroplets of LM embedded within a hyperelastic material that rupture upon induced mechanical damage, creating a percolating or continuous conductive network of LM. (B) Photograph sequence of a notched sample that is strained until mechanical failure. The propagation of the notch creates a conductive network, as indicated by the illumination of the green LEDs.

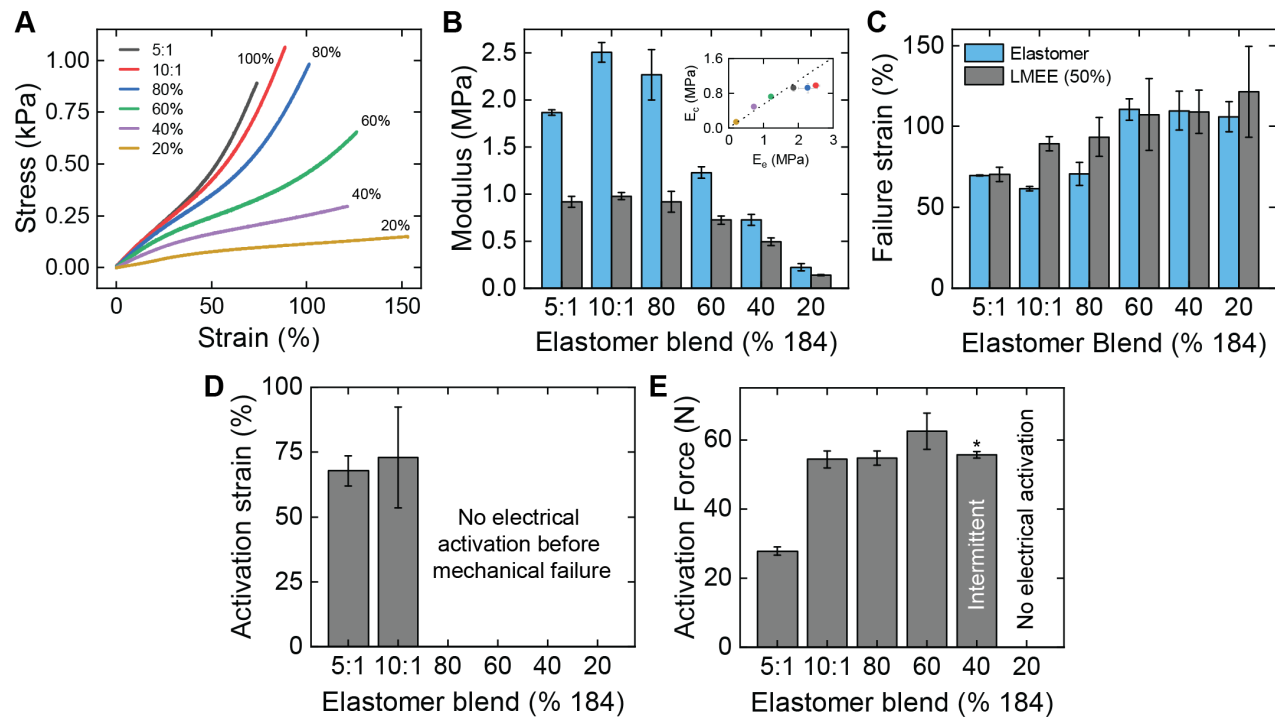


Figure 5.3: Mechanical and electrical characterization. (A) Stress-strain response under uniaxial extension to mechanical failure for two oligomer/curing agent ratios (5:1, 10:1;  $\alpha = 100\%$ ) and four different blends of Sylgard 184 and Sylgard 527 ( $\alpha = 80, 60, 40, 20\%$ , where  $\alpha$  is the ratio of Sylgard 184 to Sylgard 527). (B) Modulus as a function of elastomer blend ( $\phi = 50, 0\%$ ). Inset: Composite modulus,  $E_c$ , as a function of elastomer modulus,  $E_e$ , and Eshelby's inclusion theory (dashed line), assuming incompressible fluidic inclusions,  $E_i = 0$  Pa. (C) Mechanical failure strain as a function of elastomer blend ( $\phi = 50, 0\%$ ). (D) Uniaxial extension strain upon which an electrical network is formed. For samples blended with Sylgard 527, an electrical network did not form before mechanical failure. (E) Compression force required to cause the formation of an electrical network. Electrical activation was intermittent for the  $\alpha = 40\%$  blend and did not occur for approximately half of the samples tested ( $N = 12$ ). All error bars are the standard deviation. (B,C,D)  $N = 3$ , (E)  $N = 5$ .

$\mu\text{m}$  particles, Figure 7.8, 7.9). Eutectic gallium-indium (75% Ga, 25% In; EGaIn) is selected as the LM filler due to its favorable properties including high electrical conductivity, low viscosity, low melting point, and negligible toxicity (as compared to Hg)<sup>[29]</sup>. In the presence of oxygen, the LM will form an insulating  $\sim 0.5\text{-}3$  nm oxide skin<sup>[11,134]</sup>. I use an elastomer blend<sup>[124]</sup> of Sylgard 184 and Sylgard 527 to tailor the mechanical characteristics of the solid-liquid hybrid composite and its sensitivity to mechanical damage.

### 5.3 Mechanical Characterization

The mechanical behavior of the LM-elastomer composite ( $\phi = 50\%$ ) is studied under tensile loading for two oligomer/curing agent ratios (5:1, 10:1;  $\alpha = 100\%$ ) and four different blends of Sylgard 184 and Sylgard 527 ( $\alpha = 80, 60, 40, 20\%$ , where  $\alpha$  is the ratio of Sylgard 184 to Sylgard 527). Figure 5.3A presents the stress-strain curves for the different LM-elastomer composites. From this data, the influence of the liquid inclusions is studied by measuring the tensile modulus of the filled,  $E_c$ , and unfilled,  $E_e$ , elastomer. Figure 5.3B shows that the LM inclusions soften the compliant-matrix. These results generally agree with Eshelby's inclusion theory<sup>[32]</sup>,  $E_c = E_e / (1 + 5\phi/3)$ , assuming incompressible fluidic inclusions ( $E_i = 0$  Pa). Referring to the Figure 5.3B

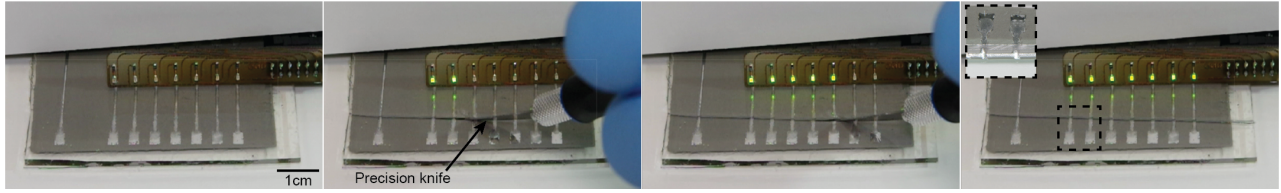


Figure 5.4: Photograph sequence of mechanical damage induced by a precision knife. The propagation of damage is indicated by the green LEDs. Inset: photograph of the cut surface.

inset, both the experimental and theory suggest an approximately 50% decrease in the stiffness with the addition of LM inclusions ( $\phi = 50\%$ ). As shown in Figure 5.3C, the elastic strain limit of the elastomer and composite generally increases with increasing compliance. While, the LM inclusions have a negligible influence on the strain limit of the elastomer composite, they can significantly increase the toughness of the host elastomer by resisting fracture propagation<sup>[63]</sup>. Here, I observe that LM inclusions increase the compliance of the soft, silicone rubber, while maintaining the elastic strain limit. This desirable combination of properties is uniquely enabled by the inclusion of liquid metal droplets, which preserve the properties of the host material and enable electronic damage detection and localization.

#### 5.4 Formation of Electrical Networks

The LM-elastomer composite is (naturally) electrically insulating after curing due to the presence of an insulating oxide skin and lack of droplet-droplet interactions (or percolating networks). However, the application of local pressure or various modes of mechanical damage (e.g. cutting, puncture, large strain deformation) can cause the LM inclusions to rupture, forming a conductive percolating network (conductance,  $G > 0.003$  S) that is internal to the composite. The damage initiated change in electrical conductivity was systematically studied for the different elastomer blends and various modes of mechanical damage. First, the electrical conductivity was monitored between two conductive tabs of a dogbone specimen under uniaxial deformation. As shown in Figure 5.3D, only the Sylgard 184 specimens ( $\alpha = 100\%$ ) formed an electrical network before mechanical failure occurred. The composite was then subjected to mechanical compression. A glass cylindrical indenter (3 mm diameter, 10 mm length) was pressed into the composite across two conductive traces until an electrical network was formed. As shown in Figure 5.3E, a large compressive force is required to form an electrical network. The softer LM-elastomer composites either did not form an electrical network under compression ( $\alpha = 20\%$ ) or only achieved intermittent activation (6 of 12,  $\alpha = 40\%$ ) that was typically not permanent (Figure 7.10). Lastly, all elastomer blend

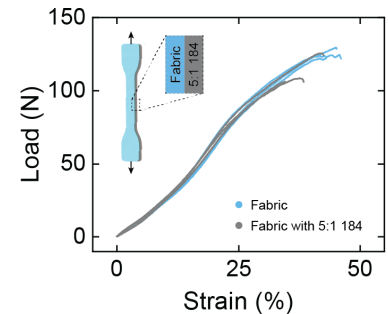


Figure 5.5: Stress-strain response of rip-stop nylon fabric coated with the LM-elastomer composite.

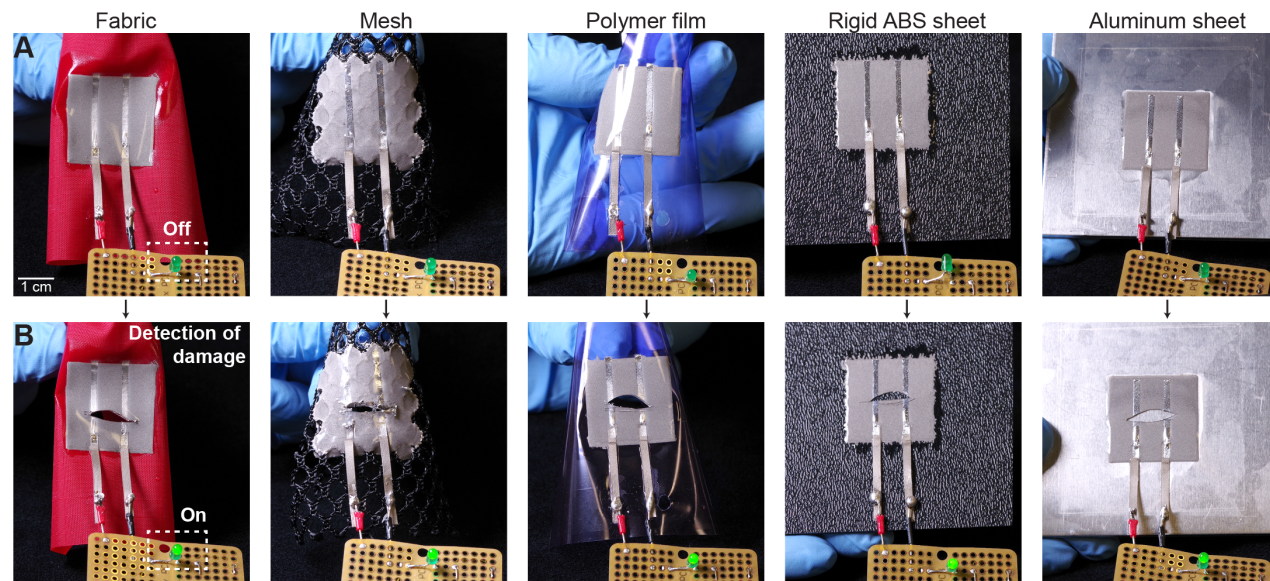


Figure 5.6: Damage detection substrate versatility. **(A)** The damage sensing composite is fabricated on a variety of substrates while maintaining electrical insulation. **(B)** Upon cutting the substrate, the material activates on all substrates (bottom row), as indicated by the illuminated LED.

composites were observed to form an electrical network when cut with a precision knife. Figure 5.4 shows the formation of a permanent electrical network as indicated by the illumination of the green LEDs as the knife passes through the material. During puncture events, such as cutting, the LM droplets on the damaged surface are severed in addition to the formation of an internal percolating network (Figure 5.4 inset). In the presence of oxygen, an oxide skin is formed on the exposed LM, preventing unwanted flow of LM. These results demonstrate that the composite is stable under typical operational conditions and that the mechanical properties of the composite can be easily tuned without increasing the overall thickness of the device to achieve damage initiated conductivity only when puncture occurs.

### 5.5 Integration with Host Substrates

To demonstrate the ability to integrate the active damage layer with existing structures, the composite was coated on a variety of commonly used materials including fabric (nylon, polyester), plastic (Polyethylene terephthalate (PET), acrylonitrile butadiene styrene (ABS)), and metal (aluminum). As shown in Figure 5.6, the composite can be directly coated and cured on a variety of materials or attached using a silicone glue (Sil-poxy, Smooth-On). When coated on flexible substrates (fabric, thin plastic film), the soft and highly compliant LM-elastomer composite is electrically stable and does not restrict the general kinematic motion of the flexible substrate (Figure 5.6 top) and has

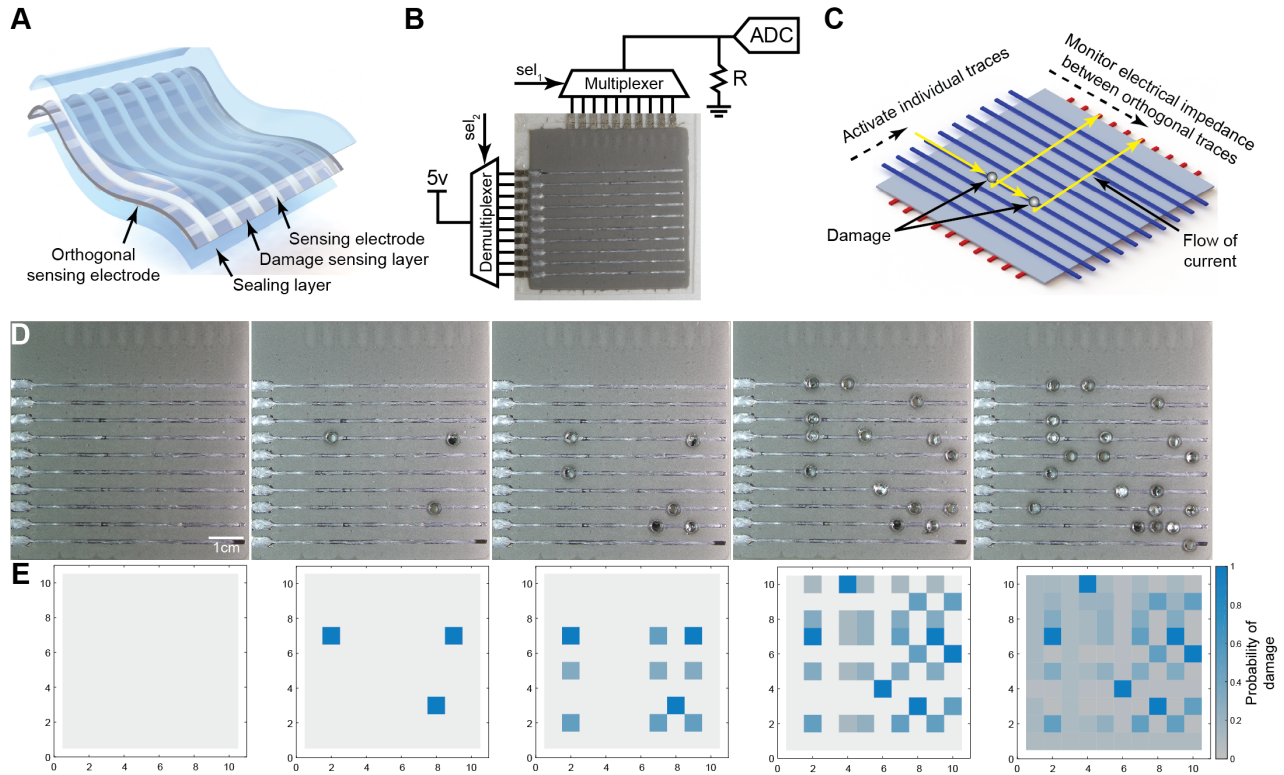


Figure 5.7: Damage detection and 2D localization. (A) Illustration of the damage detection composite with spray deposited 2D grid of LM. (B) Electrical circuit used to detect and localize changes in conductivity (damage). (C) Current flows through the thickness of the composite when mechanical damage occurs. (D) A random sequence of 19 damage events and (E) the estimated probability of damage. The height of each node is proportional to the probability of damage at that location.

a negligible influence on the stress-strain response (Figure 5.5). Additionally, similar to the stand-alone device, when used as a coating, the LM-elastomer composite is able to detect damage as indicated by the illuminated LED (Figure 5.6 bottom). These results demonstrate that the composite can be used as a coating to detect damage on a variety of substrates, ranging from flexible to rigid, polymeric to metallic, and porous to continuous.

### 5.6 Detection and Localization of Damage

The LM-elastomer composite reports changes in structural health through local changes in electrical conductivity. To actively detect and localize changes in electrical conductivity, a highly deformable active-matrix grid of LM is spray deposited<sup>[57]</sup> onto the composite and sealed in a thin elastomer layer ( $t = 0.5$  mm) to prevent smearing. Mechanical damage is detected in 1D samples (Figure 5.1D, 5.3G) by measuring the electrical impedance between adjacent LM traces (5 mm center-to-center spacing). For 2D detection and localization, a second array is spray deposited on the opposite side, forming a 10x10 active-matrix grid that monitors through-thickness conductivity (Figure 5.7A). A

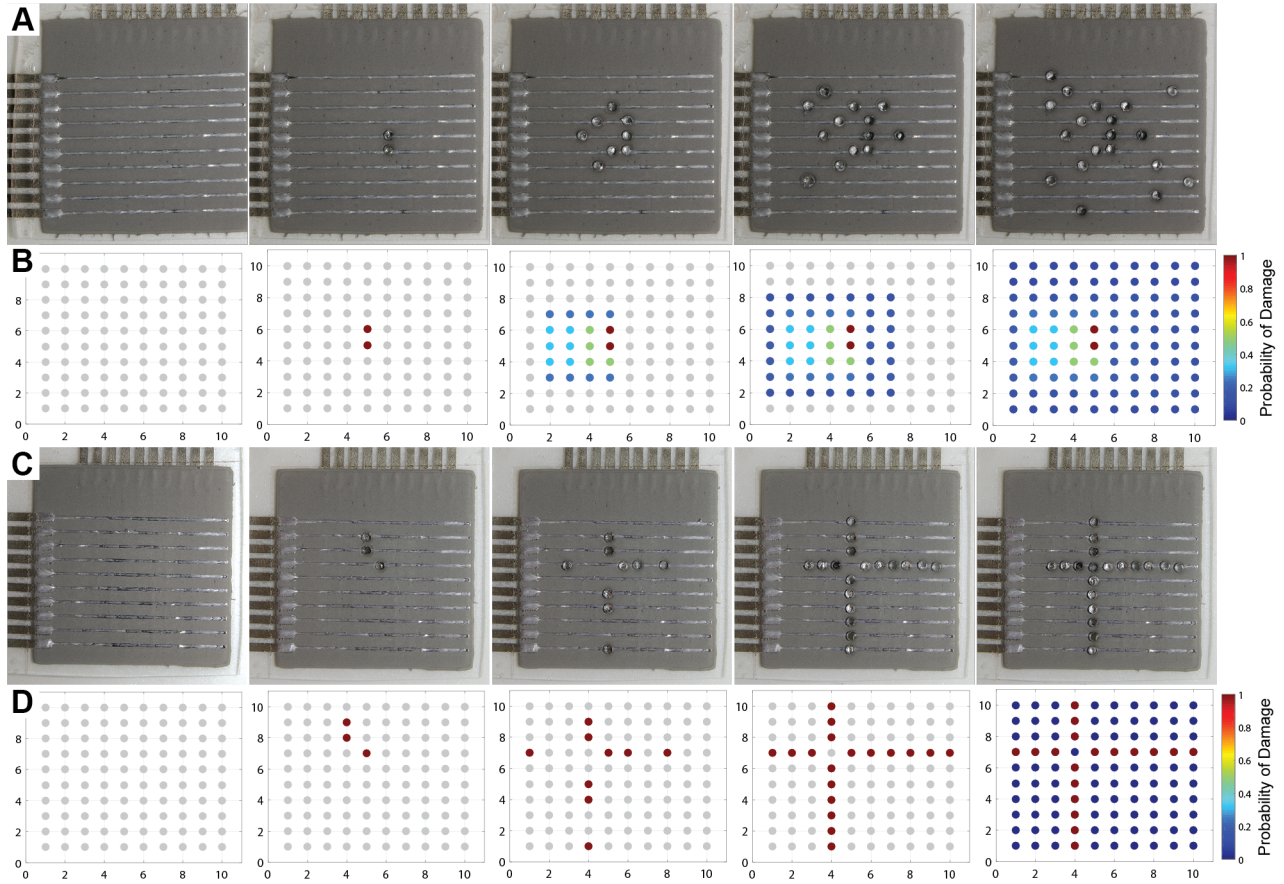


Figure 5.8: Bounds of damage detection and localization. (A) A sequence of 19 damage events with (B) 2 events localized with 100% probability. (C) A sequence of 19 damage events with (D) 18 events localized with 100% probability.

pair of electronic switches and microcontroller with an analog to digital converter (ATmega 328, Atmel) was used to monitor the impedance at each of the nodes within the grid (Figure 5.7B). First, the demultiplexer applies a voltage potential to an individual trace. The multiplexer then scans all the orthogonal traces. If a voltage is sensed on an orthogonal trace, damage has occurred at the intersection of the two traces, as illustrated in Figure 5.7C. The demultiplexer is then indexed to the next trace and the orthogonal traces are scanned again.

To demonstrate this method for detecting and localizing damage, a random number generator was used to select a sequence of 19 nodes within the grid. A hammer-driven hole punch (3 mm diameter) was then used to induce mechanical damage at the specified node, as shown in Figure 5.7D. The sensed damage is then plotted (Figure 5.7E). The 2D grid can detect multiple locations with 100% probability, however the active matrix grid has inherent limitations that results in ghosting. Here, the probability of damage was calculated as  $1/(\text{number of activated nodes})$ . The calculated probability of damage for the

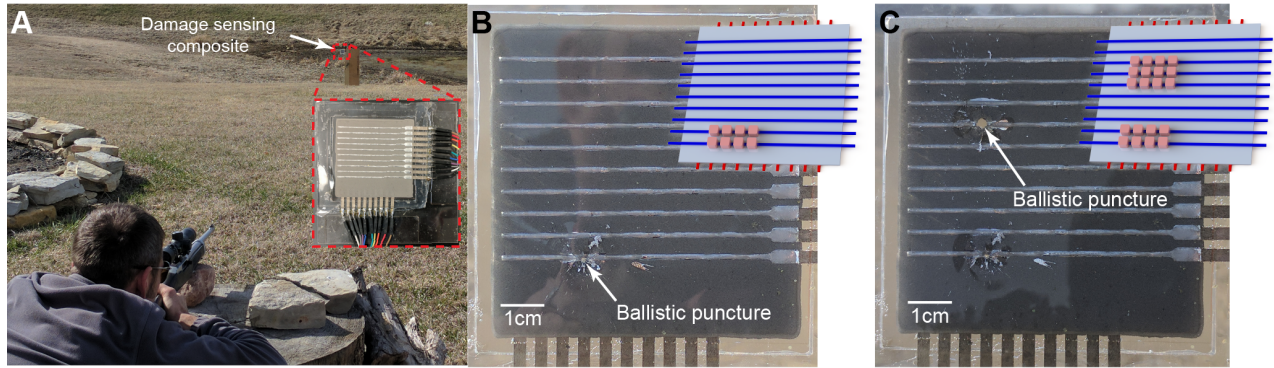


Figure 5.9: Detection and localization of ballistic puncture. (A) Two projectiles were fired at the damage sensing composite using a .22-caliber long rifle. (B & C) (left) The projectile passed through the composite that was supported as a membrane on an acrylic frame. (right) Damage was detected and localized as indicated by the red nodes.

random sequence is shown in Figure 5.7E. The hue of each of the nodes is proportional to the probability of damage at that location. For this study, the probability of damage ranged from 100 to 5%, with 6 locations of 100% probability (random case). In practice, for a grid with  $M$  rows and  $N$  columns, the material will be able to detect and localize at least two nodes with 100% probability (worst case, Figure 5.8 A,B). The maximum number of locations that can be detected and localized with no uncertainty is  $M+N-2$ , or 18 nodes for a  $10 \times 10$  grid as shown in Figure 5.8 C,D (best case). Furthermore, there will be  $M+N-1$  possible independent events, or changes in state where a new damage event is detected and localized. The height of each of the nodes is proportional to the probability of damage at that location. For this study, the probability of damage ranged from 100 to 5%, with 6 locations of 100% probability. For a  $M \times N$  matrix, at least two nodes will have no uncertainty with an upper bound of  $M+N-2$  nodes (Figure 5.8). A  $M \times N$  will have  $M+N-1$  possible independent events, or changes in state. These experiments highlight the composite's unique ability to detect and localize extreme damage events, without experiencing catastrophic failure when the active-matrix grid is severed or portions are completely removed. The goal of the damage sensing composite is not to localize every damage event with no uncertainty, as a large number of damage events would likely lead to an irrecoverable state. Instead, the purpose is to introduce an artificial nervous tissue that extends the longevity of soft-matter systems by reporting that damage has occurred with high probability and calculate the severity to electrically signal the onset of adaptation, self-healing, or regeneration in response to the external stimuli. These experiments highlight the composite's unique ability to detect and localize multiple extreme damage events with high probability, without experiencing catastrophic failure when the active-matrix grid is severed or portions are completely removed.

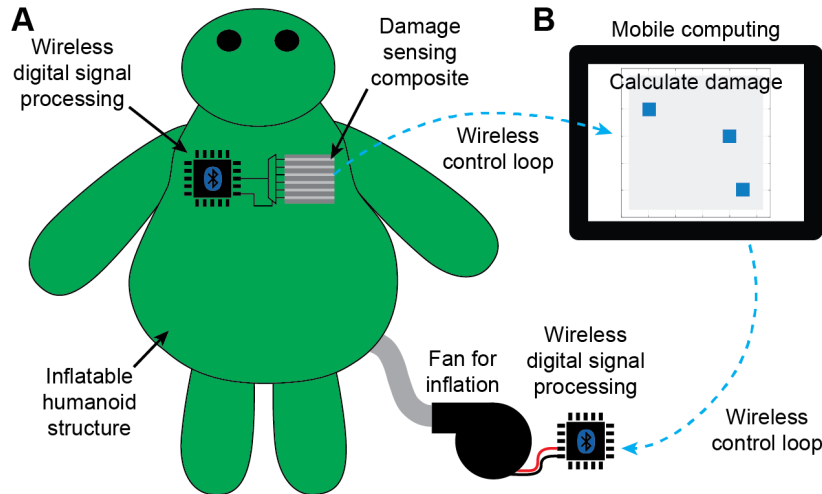


Figure 5.10: Illustration of an inflatable humanoid structure. (A) A soft, untethered inflatable humanoid structure with programmable fan for inflation was augmented with the damage sensing composite. The fan is shown outside the inflatable structure for visualization. (B) A mobile computing platform is used for visualization of damage, recording damage and pressure data, and provides a wireless link between the damage sensing composite and programmable fan.

### 5.7 Ballistic Puncture

To further examine the effects of extreme damage, the 2D composite was subjected to ballistic puncture. The composite was suspended as a membrane on an acrylic frame and two projectiles were fired from a .22-caliber long rifle (10/22, Ruger) at approximately 25 meters (Figure 5.9A). The projectile impact resulted in a fairly large damage zone that is instantaneously activated (Figure 5.9B & 5.9C). The projectile exit is shown in Figure 7.11. The detected damage zone is significantly larger than the entrance or exit hole due to the ballistic shock wave that is generated by the bullets. These results further demonstrate the composite's ability to detect and localize extreme damage in a highly uncontrolled environment.

### 5.8 Soft Robotics Demonstration

The electrical response to damage enables integration with existing control systems and provides unique opportunities to monitor structural health within soft robots or inflatable structures. Here I use the composite to augment the exterior of an inflatable, untethered soft structure intended to mimic a soft humanoid robot (Figure 5.10A). The composite functions as an artificial nervous tissue to detect and respond to external damage. The soft robot mimic is composed of a fabric suit, a fan that continuously runs to compensate for leaks, and a plastic skeleton to support the suit (Figure 7.12). The fan is set to the minimum velocity required to maintain sufficient inflation, as shown in Figure 5.11A & 5.11B (left). Three holes, approximately  $625 \text{ mm}^2$  in size, are cut into the soft robot mimic with a precision knife. In the

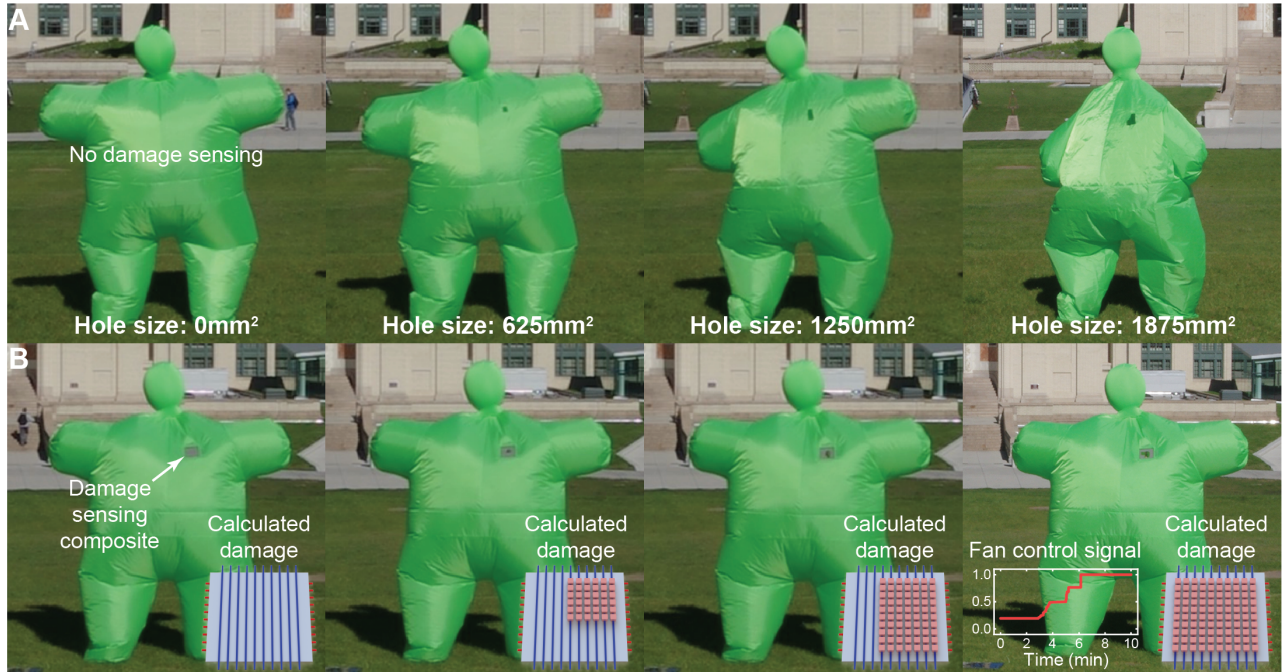


Figure 5.11: Autonomous damage detection for pressure regulation. Damage was induced using a precision knife. (A) The unmodified inflatable humanoid structure was unable to detect any environmental changes and quickly deflated as the area of damage increased. (B) The augmented inflatable humanoid structure was able to detect and respond to the environmental changes by increasing the velocity of the fan based on the estimated area of damage. (inset) Plot of the fan control signal as damage is detected and the velocity of the fan is increased to compensate for the loss in pressure. (A, bottom) Approximate area of damage.

absence of damage detection and closed-loop control, the soft robot mimic quickly deflates as the hole size increases (Figure 5.11A right). This change in state (Figure 5.11A, left to right) corresponds to an almost undetectable change in pressure, as shown in Figure 5.12 (red). In contrast, the soft robot mimic that is augmented with the damage sensing composite is capable of detecting and responding to the external damage (Figure 5.11B). After detection by the microcontroller, the damage signals are wirelessly transmitted to a mobile computing platform and the effective area of damage is calculated (Figure 5.10B). Based on the calculated damage, the on-board control system is able to adjust the velocity of the fan used for inflation to compensate for the loss in pressure caused by the damage (Figure 5.11B inset). Here, a small increase in pressure is observed (Figure 5.12, gray). This demonstration illustrates the ease of integration with existing soft-matter systems and compatibility with on-board control, sensing, and actuation commonly used in existing robotic platforms.

## 5.9 Outlook

In collaboration with Ravi Tutika and Prof. Michael Bartlett, I have presented a soft biomimetic composite for use as an artificial nervous tissue to detect, communicate, and respond to detrimental, mechanical damage events. Mechanical damage—compression, fracture or

puncture—causes the LM droplets suspended in the soft elastomer matrix to rupture, creating local changes in electrical conductivity. By tailoring the compliance of the LM-elastomer composite, changes in electrical conductivity only occur for puncture type events. The local changes in electrical conductivity are actively detected and localized using a highly deformable active-matrix grid of LM. Furthermore, the composite can be coated on a variety of substrates and is observed to operate as expected even under extreme damage events such as ballistic puncture. When tightly coupled with actuation, computation, and communication this system provides a method for structural health monitoring in an inflatable soft robot mimic, enabling algorithmic adaptation to environmental changes. This technology, coupled with methods for self-healing, provides a path forward for continuous structural health monitoring, self-diagnosis, and repair of soft structures to rival the longevity that is exhibited in natural, biological systems.

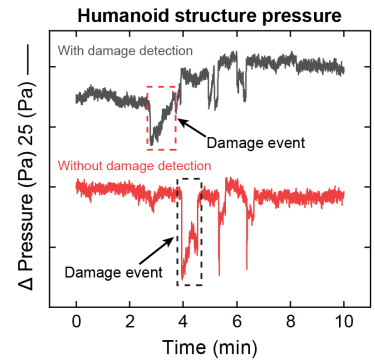


Figure 5.12: Measured change in pressure of the inflatable humanoid structure during puncture damage. (red) The change in pressure of the inflatable humanoid structure is almost undetectable using a high resolution barometer ( $\pm 1$  Pa) when failure occurs (Figure 5.11A). (gray) During response to damage, a slight increase in pressure is observed for the augmented humanoid structure (Figure 5.11B). Note, a y-axis offset is applied to the data to assist in visualization of the data.

# 6

## Conclusion and Future Outlook

In this thesis, I argue that emerging machines and electronics that require intimate physical interaction with humans will increasingly rely on new soft-matter technologies. These technologies overcome the fundamental mismatch in mechanical compliance with natural biological tissue by using intrinsically soft materials—elastomers, gels, and fluids—enabling applications that are impossible to achieve with rigid, boxy, and bulky devices that exist today.

### 6.1 Closing Remarks

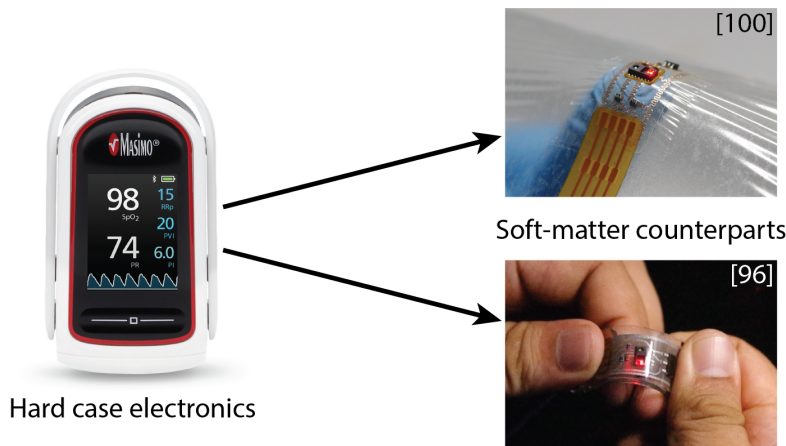


Figure 6.1: Electronics are removed from hard plastic or metal casing to create soft-matter counterparts, enabling intimate interactions with the human body.

Figure 6.1 shows two soft-matter counterparts of a commonly used portable medical monitoring device (pulse oximeter). The use of intrinsically soft materials enables the device to be comfortably worn on the body for long-term patient monitoring without interfering with daily activities. Furthermore the soft-matter counterpart allows access to additional locations on the human body that were previously inaccessible, while enhanced conformal skin contact promises reduced

motion artifacts and improved signal quality. To allow use outside of a controlled laboratory environment, new unifying fabrication methodologies that address challenges in material compatibility, multi-scale fabrication, and electrical and mechanical interfacing were developed to provide a method for integrating electrical components for signal processing, wireless communication, and power regulation with soft-matter circuit interconnects<sup>[100,96]</sup>. These methods provide a path forward for the design and optimization of devices for diverse applications, including soft robotics, electronic skins, and human-machine interfaces.

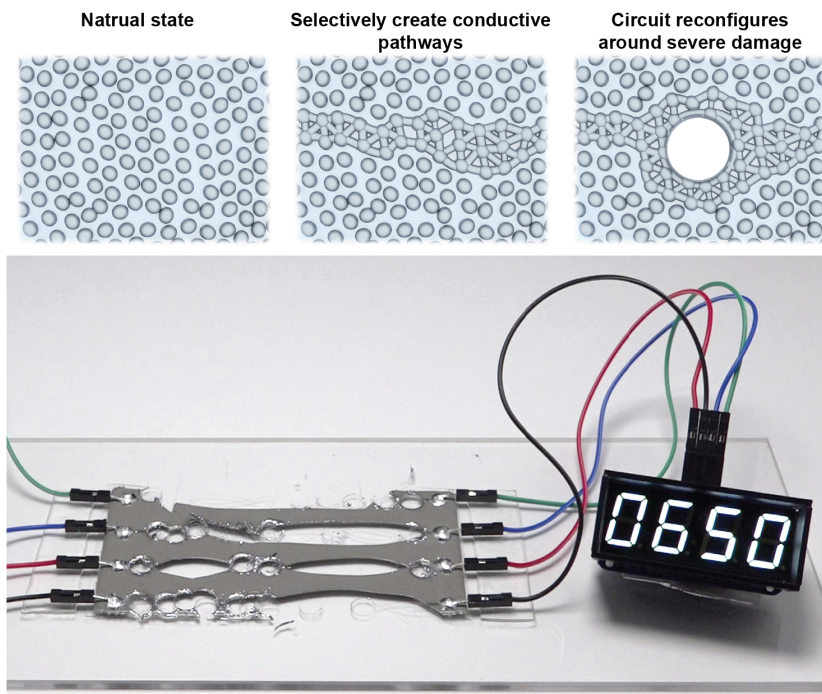


Figure 6.2: New material architecture enables soft, stretchable circuits to be created that instantaneously reroute the electrical network when damage occurs.

While hard case electronics use rigid substrates and packaging to mitigate damaging stress concentrations, such encapsulation will interfere with the elasticity of soft circuits. Consequently, as these soft-matter counterparts enter natural, unstructured environments, damage is inevitable. Figure 6.2 illustrates a new material architecture that is capable of instantaneously rerouting the electrical network to maintain functionality when damage occurs<sup>[101]</sup>. The material is composed of liquid metal droplets suspended in a soft elastomer; when damaged, the droplets rupture to form new connections with neighbours and re-route electrical signals without interruption. Since self-healing occurs spontaneously, these materials do not require manual repair or external heat. This unprecedented electronic robustness will be criti-

cal in applications such as remote teleoperation or autonomous field robotics where repair is challenging or impossible.

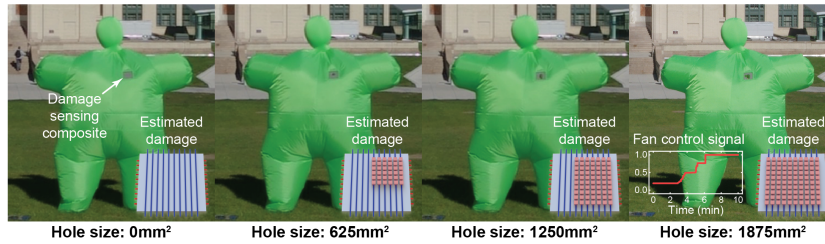


Figure 6.3: New material architecture enables detection, communication, and response to damage using only soft materials.

Self-healing provides a method to maintain or recover functionality when damage occurs. However, these soft-matter counterparts will inevitably reach an irrecoverable state. To provide active management of soft-matter technologies, the LM-elastomer composite can be used as an artificial nervous tissue to electrically detect, localize, and respond to detrimental damage events using only soft materials (Figure 6.3)<sup>[102]</sup>. The damage initiated change in electrical conductivity can be actively detected and localized using LM electrodes that are patterned onto the composite. When coupled with actuation, communication, and computation, this soft and highly deformable biomimetic composite presents new opportunities to autonomously identify damage, calculate severity, and respond to prevent failure within robotic systems.

## 6.2 Future Outlook

I conclude this dissertation by extrapolating the current evolution to future clinical and robotics translations. I also discuss the next steps to engineering machines and electronics that match the extraordinary resilience of natural biological tissue—i.e. a soft conductive material that is capable of both electrical and mechanical self-healing without requiring manual intervention.

### 6.2.1 Clinical Translation

The global market for wearable medical monitoring devices is projected to reach \$14.41 billion by 2022<sup>[98]</sup>. Arguably, the next big push is towards personalized health care that provides the right data, from the right patient, at the right time. Existing portable technologies are bulky and intrusive and cannot be comfortably worn on the body during sleep or daily activities. Furthermore, many patient populations with complicating physical factors (e.g. edema) are not able use standard, commercially available sensors. Combining the soft sensing

Work related to 3D printing of soft materials is in collaboration with Dr. Sara Abdollahi, under the supervision of Prof. Adam Feinberg and Prof. Carmel Majidi.

elements presented within this thesis with soft-matter additive manufacturing provides a path forward for creating highly customizable wearable devices. An illustration of the proposed vision is shown in Figure 6.4. A custom-fit wearable device would enable real-time continuous vital monitoring for preventive care for early detection of disease progression and ultimately enable predictive modeling prior to disease onset.

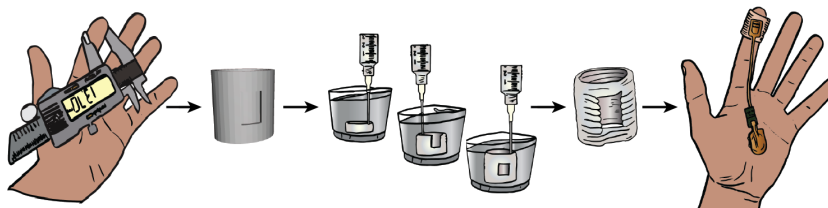


Figure 6.4: To provide personalized medical monitoring solutions, soft-matter 3D printing provides a method to rapidly create patient specific medical monitoring devices. Image drawn by Dr. Sara Abdollahi.

We are at the verge of a major revolution in the way our health and wellbeing is managed. The miniaturization of physiological sensors has enabled the development of commercial technologies that provide continuous monitoring of detailed information about daily activity, sleep, and biometric data that is user-friendly and unobtrusive. I envision a future where humans will be wearing dozens of sensors as accessories or implants that will monitor a multitude of physiologic indicators. The above-mentioned revolution will be manifested as a paradigm shift to preventive care/medicine, resulting in improved health and reduced financial burdens associated with chronic disease.

Looking forward, new computational methods are needed to understand these large data sets and sensor streams. The low-level sensor data provided by current commercial technologies, often provides little insight. The most advanced technologies can provide a history of biometric data, however without interpretation from a medical professional, this data almost useless. There is great opportunity to develop new algorithms for general-purpose physiological monitoring to gain high-level context-sensitive insight from low-level sensor data (Figure 6.5).

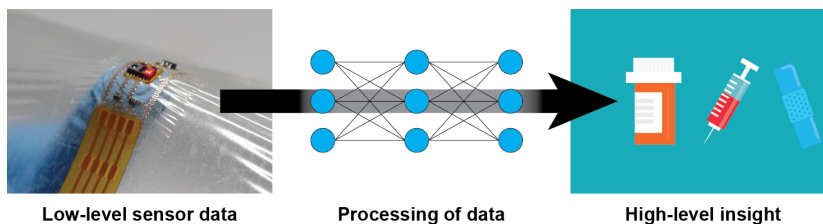


Figure 6.5: New algorithms are needed for general-purpose physiological monitoring to gain high-level context-sensitive insight from low-level sensor data.

### 6.2.2 Robotics Translation

Electronic sensing skins provide information about physical contact, external stimulation, and environmental conditions. In manipulation, sensors located within the hand, can measure when contact occurs (force, position) and also provide information about physical properties (hardness, shape, texture) of the object that the robot is manipulating. These signals can be used as control parameters within manipulation algorithms to provide online grasp adjustment, contact estimation, slip detection, or object recognition. Several researchers have developed sensors for robotic manipulators to measure contact force based on different transduction mechanisms, including resistive<sup>[35]</sup>, piezoresistive<sup>[152]</sup>, capacitive<sup>[15]</sup>, mechanical displacement<sup>[77]</sup>, and optical<sup>[130,53]</sup>. While contact sensors in unstructured environments would provide valuable information about the uncertainty of contact or material properties, they are rarely integrated with robotic manipulators. Nonetheless, since the 1970s there has been continued interest in developing new and innovative tactile sensors<sup>[118]</sup>, including efforts to introduce commercial products<sup>[35,152]</sup>.

While tactile sensors are imperative for dexterous manipulation, proximity sensors can be used to provide the critical “last centimeter” sensing between object detection (data from long range sensors) and contact. One limitation of many previously reported proximity sensors is the dependence on bulk material or surface properties, making it difficult to calculate absolute distance from the sensor. The response of light reflectance sensors are highly non-linear and depend on surface reflectivity, orientation, and texture<sup>[130,53]</sup>. Capacitive and inductive proximity sensing depends on the bulk material properties (conductivity)<sup>[43]</sup>. Mechanical displacement can also be used to detect proximity but this approach requires contact and therefore is also dependent on material properties (stiffness)<sup>[77]</sup>.

Recently, researchers have placed cameras at the point of manipulation to provide rich information about the object such as force, texture, or hardness using specialized lighting and reflective coatings<sup>[84,177]</sup>. Similarly, transparent films with markers provide information before and after contact for highly textured objects<sup>[173]</sup>. While these approaches provide rich information during manipulation they are computationally expensive and sacrifice dexterity because of the overall size of the sensor.

A key limitation in the integration of sensing arrays is the amount of wiring required to read and transmit data<sup>[61]</sup>. A serial communication bus (e.g. I<sup>2</sup>C) can be used to reduce the number of wires. However, serial (as compared to parallel) data access results in slower data acquisition rates. One possible approach to reduce wired connections without

This work is in collaboration with Jonathan Rogers at NASA Johnson Space Center, under the supervision of Prof. Carmel Majidi.

slowing data acquisition includes wireless data and power transmission. I see several promising directions for future work in augmenting everyday objects and robotics with the stretchable electronic circuits presented within this thesis. A flexible version of a multi-modal tactile sensor that includes a short-range time of flight, Piezo-resistive pressure sensor, and pulse oximeter is shown in Figure 6.6. To eliminate wiring constraints, a wireless Bluetooth low energy (BLE) module is used for data communication, while a coin cell battery is used to provide power.

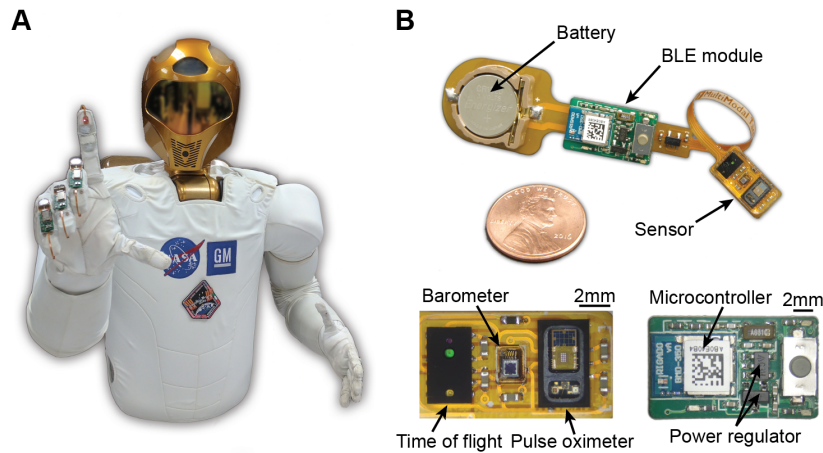


Figure 6.6: Wireless multi-modal tactile sensor. (A) The tactile sensors are shown integrated with an existing robotic platform, Robonaut 2. (B) Photograph of the multi-modal tactile sensor that includes a short-range time of flight, Piezo-resistive pressure sensor, and pulse oximeter. A microcontroller with wireless Bluetooth low energy (BLE) transceiver is used for data communication, while a coin cell battery provides power.

### 6.2.3 Next Generation Materials

Biological systems exhibit extraordinary resilience and adaptation in widely changing environments. By learning from nature, I hope to design systems that exhibit similar robustness without requiring manual intervention and the ability to adapt to a wide variety of failures. A next step to developing machines and electronics that exhibit the extraordinary resilience of natural biological tissue is the development of soft, stretchable conductive materials that are capable of both electrical and mechanical self-healing without requiring manual intervention or elevated temperatures. One possible direction would be to create a LM-elastomer composite with a polymer network that exhibits intrinsic self-healing characteristics. There are two possible strategies for developing an artificial mechanically self-healing system: i) the composite can be embedded with microcapsules that rupture when damage occurs to release healing agents<sup>[166]</sup> or ii) the polymer has dynamic, reversible bonds that reform after damage<sup>[153]</sup>. Despite the intriguing opportunity, several challenges exist to find a polymer network that exhibits intrinsic mechanical self-healing characteristics and

enables controlled rupturing and interaction between neighboring LM droplets forming local percolating networks to facilitate electrical self-healing.

Alternatively, highly porous, conductive networks (scaffolds) can be backfilled with polymer networks that exhibits intrinsic self-healing characteristics. The conductive networks provide a skeleton for the polymer network and facilitates mechanical and electrical self-healing that recovers most of the original strength and electrical conductivity of the composite. Figure 6.7 shows an example of a next generation soft robot that is capable of both mechanically and electrically self-healing at room-temperature. Here the soft robot is cut in half using a razor blade. The two halves of the robot are then manually rejoined to facilitate mechanical healing through the reconfiguration of dynamic bonds and the percolating electrical network is reformed at the damaged surface.



Figure 6.7: Example of a next generation soft robot that is capable of both mechanically and electrically self-healing. (A) Original state of the soft robot. (B) The soft robot is cut in half using a razor blade. (C) The two halves of the soft robot are manually rejoined to facilitate both mechanical and electrical self-healing.

Dynamic bonds and microcapsules provide a method for healing microcracks or deep scratches to recover the original mechanical properties of the material. However, when larger, puncture type damage occurs that results in physical displacement of material, new material must be transported to the damage site to fully restore performance of the composite. Regeneration is the ultimate challenge of replicating the ability of living systems to respond to damage. Methods based on microfluidic networks have been proposed to slowly regenerate the polymer network<sup>[167]</sup>. However, these methods require the use of external pumps and fluid reservoirs to facilitate regeneration. The human body's ability to regenerate material after displacement without tethers presents an intriguing opportunity for compliant, engineered systems. Such a technology provides a path forward to increase the longevity of soft-matter systems, while reducing waste and increasing reliability. Robust soft-matter technologies are critical for future applications such as field robotics, medical implants, and space exploration where repair is costly, challenging, or impossible.

The ability of soft-matter technologies to withstand general wear and tear and to autonomously (without human intervention) adapt, sense, and respond to detrimental damage events will be critical for

commercialization and life outside of a controlled laboratory environment.

# Bibliography

- [1] Morteza Amjadi, Ki-Uk Kyung, Inkyu Park, and Metin Sitti. Stretchable, skin-mountable, and wearable strain sensors and their potential applications: A review. *Advanced Functional Materials*, 26(11):1678–1698, 2016.
- [2] T Araki, M Nogi, M Suganuma, K andKogure, and O Kirihara. Printable and stretchable conductive wirings comprising silver flakes and elastomers. *IEEE Electron Device Letters*, 32:1424–1426, 2011.
- [3] Michael D Bartlett and Alfred J Crosby. Scaling normal adhesion force capacity with a generalized parameter. *Langmuir*, 29(35): 11022–11027, 2013.
- [4] Michael D Bartlett and Alfred J Crosby. Material transfer controlled by elastomeric layer thickness. *Materials Horizons*, 1(5): 507–512, 2014.
- [5] Michael D Bartlett, Andrew Fassler, Navid Kazem, Eric J Markvicka, Pratiti Mandal, and Carmel Majidi. Stretchable, high-k dielectric elastomers through liquid-metal inclusions. *Advanced Materials*, 28(19):3726–3731, 2016.
- [6] Michael D Bartlett, Navid Kazem, Matthew J Powell-Palm, Xiaonan Huang, Wenhuan Sun, Jonathan A Malen, and Carmel Majidi. High thermal conductivity in soft elastomers with elongated liquid metal inclusions. *Proc. Natl Acad Sci. USA*, page 201616377, 2017.
- [7] Nicholas W Bartlett, Michael T Tolley, Johannes TB Overvelde, James C Weaver, Bobak Mosadegh, Katia Bertoldi, George M Whitesides, and Robert J Wood. A 3d-printed, functionally graded soft robot powered by combustion. *Science*, 349(6244): 161–165, 2015.
- [8] Benjamin J Blaiszik, Sharlotte LB Kramer, Martha E Grady, David A McIlroy, Jeffrey S Moore, Nancy R Sottos, and Scott R

- White. Autonomic restoration of electrical conductivity. *Adv. Mater.*, 24(3):398–401, 2012.
- [9] J William Boley, Edward L White, George T-C Chiu, and Rebecca K Kramer. Direct writing of gallium-indium alloy for stretchable electronics. *Advanced Functional Materials*, 24(23): 3501–3507, 2014.
- [10] John William Boley, Edward L White, and Rebecca K Kramer. Mechanically sintered gallium–indium nanoparticles. *Adv. Mater.*, 27(14):2355–2360, 2015.
- [11] Ludovico Cademartiri, Martin M Thuo, Christian A Nijhuis, William F Reus, Simon Tricard, Jabulani R Barber, Rana NS Sodhi, Peter Brodersen, Choongik Kim, Ryan C Chiechi, et al. Electrical resistance of agts–s (ch2) n- 1ch3//ga2o3/egain tunneling junctions. *The Journal of Physical Chemistry C*, 116(20): 10848–10860, 2012.
- [12] Qing Cao, Hoon-sik Kim, Ninad Pimparkar, Jaydeep P Kulkarni, Congjun Wang, Moonsub Shim, Kaushik Roy, Muhammad A Alam, and John A Rogers. Medium-scale carbon nanotube thin-film integrated circuits on flexible plastic substrates. *Nature*, 454 (7203):495–500, 2008.
- [13] Yue Cao, Timothy G Morrissey, Eric Acome, Sarah I Allec, Bryan M Wong, Christoph Keplinger, and Chao Wang. A transparent, self-healing, highly stretchable ionic conductor. *Advanced Materials*, 29(10), 2017.
- [14] Louis Cartz. Nondestructive testing. 1995.
- [15] Alexi Charalambides and Sarah Bergbreiter. Rapid manufacturing of mechanoreceptive skins for slip detection in robotic grasping. *Advanced Materials Technologies*, 2(1), 2017.
- [16] Shi Cheng and Zhigang Wu. Microfluidic electronics. *Lab on a Chip*, 12(16):2782–2791, 2012.
- [17] Ryan C Chiechi, Emily A Weiss, Michael D Dickey, and George M Whitesides. Eutectic gallium–indium (egain): A moldable liquid metal for electrical characterization of self-assembled monolayers. *Angewandte Chemie*, 120(1):148–150, 2008.
- [18] William R Childs and Ralph G Nuzzo. Decal transfer microlithography: a new soft-lithographic patterning method. *Journal of the American Chemical Society*, 124(45):13583–13596, 2002.

- [19] Jungkeun Choi, Seokbeom Kim, Jungchul Lee, and Bumkyoo Choi. Improved capacitive pressure sensors based on liquid alloy and silicone elastomer. *IEEE Sensors Journal*, 15(8):4180–4181, 2015.
- [20] Alex Chortos, Jia Liu, and Zhenan Bao. Pursuing prosthetic electronic skin. *Nature Materials*, 15:937–950, 2016.
- [21] Jean-Baptiste Chossat, Yong-Lae Park, Robert J Wood, and Vincent Duchaine. A soft strain sensor based on ionic and metal liquids. *IEEE Sensors Journal*, 13(9):3405–3414, 2013.
- [22] Han-Sheng Chuang and Steven T Wereley. Rapid patterning of slurry-like elastomer composites using a laser-cut tape. *Journal of Micromechanics and Microengineering*, 19(9):097001, 2009.
- [23] Kyoung-Yong Chun, Youngseok Oh, Jonghyun Rho, Jong-Hyun Ahn, Young-Jin Kim, Hyouk Ryeol Choi, and Seunghyun Baik. Highly conductive, printable and stretchable composite films of carbon nanotubes and silver. *Nature nanotechnology*, 5(12):853–857, 2010.
- [24] Patrick J Codd, Arabagi Veaceslav, Andrew H Gosline, and Pierre E Dupont. Novel pressure-sensing skin for detecting impending tissue damage during neuroendoscopy: Laboratory investigation. *Journal of Neurosurgery: Pediatrics*, 13(1):114–121, 2014.
- [25] Martin L Culpepper. Design of quasi-kinematic couplings. *Precision Engineering*, 28(3):338–357, 2004.
- [26] Douglas A Davis, Andrew Hamilton, Jinglei Yang, Lee D Cremer, Dara Van Gough, Stephanie L Potisek, Mitchell T Ong, Paul V Braun, Todd J Martínez, Scott R White, et al. Force-induced activation of covalent bonds in mechanoresponsive polymeric materials. *Nature*, 459(7243):68–72, 2009.
- [27] Michael D Dickey. Emerging applications of liquid metals featuring surface oxides. *ACS applied materials & interfaces*, 6(21):18369–18379, 2014.
- [28] Michael D Dickey. Stretchable and soft electronics using liquid metals. *Adv. Mater.*, 29(27):1606425, 2017.
- [29] Michael D Dickey, Ryan C Chiechi, Ryan J Larsen, Emily A Weiss, David A Weitz, and George M Whitesides. Eutectic gallium-indium (egain): a liquid metal alloy for the formation of stable structures in microchannels at room temperature. *Advanced Functional Materials*, 18(7):1097–1104, 2008.

- [30] Kyle Doudrick, Shanliangzi Liu, Eva M Mutunga, Kate L Klein, Viraj Damle, Kripa K Varanasi, and Konrad Rykaczewski. Different shades of oxide: From nanoscale wetting mechanisms to contact printing of gallium-based liquid metals. *Langmuir*, 30(23):6867–6877, 2014.
- [31] Harold Ebneht. Metallized textile material, May 6 1980. US Patent 4,201,825.
- [32] John D Eshelby. The determination of the elastic field of an ellipsoidal inclusion, and related problems. *Proc. R. Soc. Lond. A*, 241(1226):376–396, 1957.
- [33] Andrew Fassler and Carmel Majidi. Liquid-phase metal inclusions for a conductive polymer composite. *Advanced Materials*, 27(11):1928–1932, 2015.
- [34] S Felton, M Tolley, E Demaine, D Rus, and R Wood. A method for building self-folding machines. *Science*, 345(6197):644–646, 2014.
- [35] Jeremy A Fishel and Gerald E Loeb. Sensing tactile microvibrations with the biotac—comparison with human sensitivity. In *Biomedical Robotics and Biomechatronics (BioRob), 2012 4th IEEE RAS & EMBS International Conference on*, pages 1122–1127. IEEE, 2012.
- [36] Abhishek Gannarapu and Bulent Arda Gozen. Freeze-printing of liquid metal alloys for manufacturing of 3d, conductive, and flexible networks. *Advanced Materials Technologies*, 1:1600047, 2016.
- [37] Li Gao, Yihui Zhang, Viktor Malyarchuk, Lin Jia, Kyung-In Jang, R Chad Webb, Haoran Fu, Yan Shi, Guoyan Zhou, and Luke Shi. Epidermal photonic devices for quantitative imaging of temperature and thermal transport characteristics of the skin. *Nature communications*, 5:4938, 2014.
- [38] Francine Gemperle, Chris Kasabach, John Stivoric, Malcolm Bauer, and Richard Martin. Design for wearability. In *Wearable Computers, 1998. Digest of Papers. Second International Symposium on*, pages 116–122. IEEE, 1998.
- [39] S Gevorgian, T Martinsson, and PLJ Linner. Cad models for multilayered substrate interdigital capacitors. *IEEE Transactions on Microwave Theory and Techniques*, 44(6), 1996.
- [40] Spartak S Gevorgian, Torsten Martinsson, Peter LJ Linner, and Erik Ludvig Kollberg. Cad models for multilayered substrate

- interdigital capacitors. *IEEE Transactions on microwave theory and techniques*, 44(6):896–904, 1996.
- [41] Animangsu Ghatak, Katherine Vorvolakos, Hongquan She, David L Malotky, and Manoj K Chaudhury. Interfacial rate processes in adhesion and friction, 2000.
- [42] Ken Gilleo and LLC ET-Trends. The first 105 years of flexible circuitry, 2007.
- [43] Dirk Göger, Hosam Alagi, and Heinz Wörn. Tactile proximity sensors for robotic applications. In *Industrial Technology (ICIT), 2013 IEEE International Conference on*, pages 978–983. IEEE, 2013.
- [44] Julian M Goldman, Michael T Petterson, Robert J Kopotic, and Steven J Barker. Masimo signal extraction pulse oximetry. *Journal of clinical monitoring and computing*, 16(7):475–483, 2000.
- [45] Carles Gomez, Joaquim Oller, and Josep Paradells. Overview and evaluation of bluetooth low energy: An emerging low-power wireless technology. *Sensors*, 12(9):11734–11753, 2012.
- [46] Ryan C Gough, Andy M Morishita, Jonathan H Dang, Wenqi Hu, Wayne A Shiroma, and Aaron T Ohta. Continuous electrowetting of non-toxic liquid metal for rf applications. *IEEE Access*, 2:874–882, 2014.
- [47] B Arda Gozen, Arya Tabatabai, O Burak Ozdoganlar, and Carmel Majidi. High-density soft-matter electronics with micron-scale line width. *Advanced Materials*, 26(30):5211–5216, 2014.
- [48] RV Gregory, WC Kimbrell, and HH Kuhn. Conductive textiles. *Synthetic Metals*, 28(1-2):823–835, 1989.
- [49] Mallory L Hammock, Alex Chortos, Benjamin C-K Tee, Jeffrey B-H Tok, and Zhenan Bao. 25th anniversary article: The evolution of electronic skin (e-skin): A brief history, design considerations, and recent progress. *Advanced Materials*, 25(42):5997–6038, 2013.
- [50] Frank L. Hammond, Rebecca K. Kramer, Qian Wan, Robert D. Howe, Robert J. Wood, Frank L Hammond Iii, Rebecca K. Kramer, Qian Wan, Robert D. Howe, and Robert J. Wood. Soft tactile sensor arrays for micromanipulation. *IEEE International Conference on Intelligent Robots and Systems*, 14(5):1443–1452, 2014. ISSN 21530858. doi: 10.1109/IROS.2012.6386224.
- [51] Gerard J. Hayes, Ying Liu, Jan Genzer, Gianluca Lazzi, and Michael D. Dickey. Self-folding origami microstrip antennas.

- IEEE Transactions on Antennas and Propagation*, 62(10):5416–5419, 2014. ISSN 0018926X. doi: 10.1109/TAP.2014.2346188.
- [52] Mary Josephine Hessert, Mitul Vyas, Jason Leach, Kun Hu, Lewis A Lipsitz, and Vera Novak. Foot pressure distribution during walking in young and old adults. *BMC geriatrics*, 5(1):8, 2005.
- [53] Kaijen Hsiao, Paul Nangeroni, Manfred Huber, Ashutosh Saxena, and Andrew Y Ng. Reactive grasping using optical proximity sensors. In *Robotics and Automation, 2009. ICRA'09. IEEE International Conference on*, pages 2098–2105. IEEE, 2009.
- [54] Dana Hughes and Nikolaus Correll. A soft, amorphous skin that can sense and localize textures. In *Robotics and Automation (ICRA), 2014 IEEE International Conference on*, pages 1844–1851. IEEE, 2014.
- [55] Seung Hee Jeong, Anton Hagman, Klas Hjort, Magnus Jobs, Johan Sundqvist, and Zhigang Wu. Liquid alloy printing of microfluidic stretchable electronics. *Lab on a Chip*, 12(22):4657–4664, 2012.
- [56] Seung Hee Jeong, Si Chen, Jinxing Huo, Erik Kristofer Gamstedt, Johan Liu, Shi-Li Zhang, Zhi-Bin Zhang, Klas Hjort, and Zhigang Wu. Mechanically stretchable and electrically insulating thermal elastomer composite by liquid alloy droplet embedment. *Scientific reports*, 5:18257, 2015.
- [57] Seung Hee Jeong, Klas Hjort, and Zhigang Wu. Tape transfer atomization patterning of liquid alloys for microfluidic stretchable wireless power transfer. *Scientific reports*, 5:8419, 2015.
- [58] Kenneth Langstreth Johnson et al. Contact mechanics, 1985.
- [59] Ishan D Joshipura, Hudson R Ayers, Carmel Majidi, and Michael D Dickey. Methods to pattern liquid metals. *Journal of Materials Chemistry C*, 3(16):3834–3841, 2015.
- [60] Taekeon Jung and Sung Yang. Highly stable liquid metal-based pressure sensor integrated with a microfluidic channel. *Sensors*, 15(5):11823–11835, 2015.
- [61] Zhanat Kappassov, Juan-Antonio Corrales, and Véronique Perdereau. Tactile sensing in dexterous robot hands. *Robotics and Autonomous Systems*, 74:195–220, 2015.
- [62] Navid Kazem, Tess Hellebrekers, and Carmel Majidi. Soft multifunctional composites and emulsions with liquid metals. *Advanced Materials*, 29(27), 2017.

- [63] Navid Kazem, Michael D Bartlett, and Carmel Majidi. Extreme toughening of soft materials with liquid metal. *Advanced Materials*, 30(22):1706594, 2018.
- [64] Christoph Keplinger, Jeong-Yun Sun, Choon Chiang Foo, Philipp Rothmund, George M Whitesides, and Zhigang Suo. Stretchable, transparent, ionic conductors. *Science*, 341(6149):984–987, 2013.
- [65] Seth S Kessler, S Mark Spearing, and Constantinos Soutis. Damage detection in composite materials using lamb wave methods. *Smart Materials and Structures*, 11(2):269, 2002.
- [66] Mohammad Rashed Khan, John Bell, and Michael D Dickey. Localized instabilities of liquid metal films via in-plane recapillarity. *Advanced Materials Interfaces*, 3(23):1600546, 2016.
- [67] MAH Khondoker and D Sameoto. Fabrication methods and applications of microstructured gallium based liquid metal alloys. *Smart Materials and Structures*, 25(9):093001, 2016.
- [68] Chong-Chan Kim, Hyun-Hee Lee, Kyu Hwan Oh, and Jeong-Yun Sun. Highly stretchable, transparent ionic touch panel. *Science*, 353(6300):682–687, 2016.
- [69] Dae-Hyeong Kim and John A Rogers. Stretchable electronics: materials strategies and devices. *Advanced Materials*, 20(24):4887–4892, 2008.
- [70] Dae-Hyeong Kim, Yun-Soung Kim, Jian Wu, Zhuangjian Liu, Jizhou Song, Hoon-Sik Kim, Yonggang Y Huang, Keh-Chih Hwang, and John A Rogers. Ultrathin silicon circuits with strain-isolation layers and mesh layouts for high-performance electronics on fabric, vinyl, leather, and paper. *Advanced Materials*, 21(36):3703–3707, 2009.
- [71] Dae-Hyeong Kim, Nanshu Lu, Rui Ma, Yun-Soung Kim, Rak-Hwan Kim, Shuodao Wang, Jian Wu, Sang Min Won, Hu Tao, Ahmad Islam, Ki J. Yu<sup>1</sup>, Tae-il Kim, Raees Chowdhury, Ming Ying, Lizhi Xu, Ming Li, Hyun-Joong Chung, Hohyun Keum, Martin McCormick, Ping Liu, Yong-Wei Zhang, Fiorenzo G. Omenetto, Yonggang Huang, Todd Coleman, and John A. Rogers. Epidermal electronics. *Science*, 333(6044):838–843, 2011.
- [72] Daeyoung Kim, Jun Hyeon Yoo, and Jeong-Bong Lee. Liquid metal-based reconfigurable and stretchable photolithography. *Journal of Micromechanics and Microengineering*, 26(4):045004, 2016. ISSN 0960-1317. doi: 10.1088/0960-1317/26/

4/045004. URL <http://stacks.iop.org/0960-1317/26/i=4/a=045004?key=crossref.b223ef9a5c41ae769a821319532caa33>.

- [73] Hyun-Joong Kim, Chulwoo Son, and Babak Ziaie. A multi-axial stretchable interconnect using liquid-alloy-filled elastomeric microchannels. *Appl. Phys. Lett.*, 92(1):011904, 2008.
- [74] Seokbeom Kim, Jungchul Lee, and Bumkyoo Choi. Stretching and twisting sensing with liquid-metal strain gauges printed on silicone elastomers. *IEEE Sensors Journal*, 15(11):6077–6078, 2015. ISSN 1530437X. doi: 10.1109/JSEN.2015.2462314.
- [75] Yeongin Kim, Alex Chortos, Wentao Xu, Yuxin Liu, Jin Young Oh, Donghee Son, Jiheong Kang, Amir M Foudeh, Chenxin Zhu, Yeongjun Lee, et al. A bioinspired flexible organic artificial afferent nerve. *Science*, 360(6392):998–1003, 2018.
- [76] U. Klueh, V. Wagner, S. Kelly, A. Johnson, and JD. Bryers. Efficacy of silver-coated fabric to prevent bacterial colonization and subsequent device-based biofilm formation. *J. Biomed. Mater. Res.*, 53(6):621–631, 2000.
- [77] Jelizaveta Konstantinova, Agostino Stilli, and Kaspar Althoefer. Force and proximity fingertip sensor to enhance grasping perception. In *Intelligent Robots and Systems (IROS), 2015 IEEE/RSJ International Conference on*, pages 2118–2123. IEEE, 2015.
- [78] Chiwan Koo, Brittany E. LeBlanc, Michael Kelley, Hannah E. Fitzgerald, Gregory H. Huff, and Arum Han. Manipulating Liquid Metal Droplets in Microfluidic Channels With Minimized Skin Residues Toward Tunable RF Applications. *Journal of Microelectromechanical Systems*, 24(4):1069–1076, 2014. ISSN 10577157. doi: 10.1109/JMEMS.2014.2381555.
- [79] Rebecca K Kramer, Carmel Majidi, and Robert J Wood. Masked deposition of gallium-indium alloys for liquid-embedded elastomer conductors. *Advanced Functional Materials*, 23(42):5292–5296, 2013.
- [80] Collin Ladd, Ju-Hee So, John Muth, and Michael D Dickey. 3d printing of free standing liquid metal microstructures. *Advanced Materials*, 25(36):5081–5085, 2013.
- [81] Alexandre Larmagnac, Samuel Eggenberger, Hanna Janossy, and Janos Vörös. Stretchable electronics based on ag-pdms composites. *Scientific reports*, 4, 2014.

- [82] Guangyong Li, Xuan Wu, and Dong-Weon Lee. Selectively plated stretchable liquid metal wires for transparent electronics. *Sensors and Actuators B: Chemical*, 221:1114–1119, 2015.
- [83] Guangyong Li, Xuan Wu, and Dong-Weon Lee. A galinstan-based inkjet printing system for highly stretchable electronics with self-healing capability. *Lab Chip*, 16(8):1366–1373, 2016.
- [84] Rui Li, Robert Platt, Wenzhen Yuan, Andreas ten Pas, Nathan Roscup, Mandayam A Srinivasan, and Edward Adelson. Localization and manipulation of small parts using GelSight tactile sensing. In *Intelligent Robots and Systems (IROS 2014), 2014 IEEE/RSJ International Conference on*, pages 3988–3993. IEEE, 2014.
- [85] Wenle Li, Christopher C Matthews, Ke Yang, Michael T Odarzenko, Scott R White, and Nancy R Sottos. Autonomous indication of mechanical damage in polymeric coatings. *Advanced Materials*, 2016.
- [86] Suqing Liang, Yaoyao Li, Yuzhen Chen, Jinbin Yang, Taipeng Zhu, Deyong Zhu, Chuanxin He, Yizhen Liu, Stephan Handschuh-Wang, and Xuechang Zhou. Liquid metal sponges for mechanically durable, all-soft, electrical conductors. *J. Mater. Chem. C*, 5(7):1586–1590, 2017.
- [87] Yiliang Lin, Christopher Cooper, Meng Wang, Jacob J Adams, Jan Genzer, and Michael D Dickey. Handwritten, soft circuit boards and antennas using liquid metal nanoparticles. *Small*, 11(48):6397–6403, 2015.
- [88] Kenyu Ling, Hyung Ki Kim, Minyeong Yoo, and Sungjoon Lim. Frequency-switchable metamaterial absorber injecting eutectic gallium-indium (EGaIn) liquid metal alloy. *Sensors*, 15(11):28154–28165, 2015. ISSN 14248220. doi: 10.3390/s151128154.
- [89] DJ Lipomi, M Vosgueritchian, BCK Tee, SL Hellstrom, JA Lee, CH Fox, and Z Bao. Skin-like pressure and strain sensors based on transparent elastic films of carbon nanotubes. *Nature Nanotechnology*, 6(6):788–792, 2011.
- [90] Hod Lipson and Melba Kurman. *Fabricated: The new world of 3D printing*. John Wiley & Sons, 2013.
- [91] Chao-Xuan Liu and Jin-Woo Choi. Embedding conductive patterns of elastomer nanocomposite with the assist of laser ablation. *Microsystem technologies*, 18(3):365–371, 2012.

- [92] Peng Liu, Siming Yang, Aditya Jain, Qiugu Wang, Huawei Jiang, Jiming Song, Thomas Koschny, Costas M Soukoulis, and Liang Dong. Tunable meta-atom using liquid metal embedded in stretchable polymer. *Journal of Applied Physics*, 118(1):014504, 2015.
- [93] T Liu, P Sen, and CJ Kim. Characterization of nontoxic liquid-metal alloy galinstan for applications in microdevices. *Journal of Microelectromechanical Systems*, 21(2):443–450, 2012.
- [94] Tong Lu, Lauren Finkenauer, James Wissman, and Carmel Majidi. Rapid prototyping for soft-matter electronics. *Advanced Functional Materials*, 24(22):3351–3356, 2014.
- [95] Tong Lu, James Wissman, and Carmel Majidi. Soft anisotropic conductors as electric vias for ga-based liquid metal circuits. *ACS Applied Materials & Interfaces*, 7(48):26923–26929, 2015.
- [96] Tong Lu, Eric Markvicka, Yichu Jin, and Carmel Majidi. Soft-matter printed circuit board with uv laser micropatterning. *ACS Applied Materials & Interfaces*, 9(26):22055–22062, 2017.
- [97] Andrew D Marchese, Cagdas D Onal, and Daniela Rus. Autonomous soft robotic fish capable of escape maneuvers using fluidic elastomer actuators. *Soft Robotics*, 1(1):75–87, 2014.
- [98] MarketsandMarkets. Wearable medical devices market: Global forecast until 2022, 2018.
- [99] E. Markvicka, S. Rich, J. Liao, H. Zaini, and C. Majidi. Low-cost wearable human-computer interface with conductive fabric for steam education. In *2018 IEEE Integrated STEM Education Conference (ISEC)*, pages 161–166, March 2018. doi: 10.1109/ISECon.2018.8340469.
- [100] Eric J Markvicka, Michael D Bartlett, and Carmel Majidi. Rapid fabrication of soft, multilayered electronics for wearable biomonitoring. *Advanced Functional Materials*, 26(46):8496–8504, 2016.
- [101] Eric J Markvicka, Michael D Bartlett, Xiaonan Huang, and Carmel Majidi. An autonomously electrically self-healing liquid metal–elastomer composite for robust soft-matter robotics and electronics. *Nature materials*, 17(7):618–624, 2018.
- [102] Eric J Markvicka, Ravi Tutika, Michael D Bartlett, and Carmel Majidi. Multi-site damage detection and localization for health monitoring of soft-matter electronics and structures. *Under review*, 2018.

- [103] N Matsuhisa, M Kaltenbrunner, T Yokota, Hi Jinno, K Kuribara, T Sekitani, and T Someya. Printable elastic conductors with a high conductivity for electronic textile applications. *Nature Communications*, 6(7461):7461, 2015.
- [104] Ryosuke Matsuzaki and Kosuke Tabayashi. Highly stretchable, global, and distributed local strain sensing line using gainsn electrodes for wearable electronics. *Advanced Functional Materials*, 25(25):3806–3813, 2015.
- [105] Michael Andrew McEvoy and Nikolaus Correll. Materials that couple sensing, actuation, computation, and communication. *Science*, 347(6228):1261689, 2015.
- [106] DR McKenzie and RC McPhedran. Exact modelling of cubic lattice permittivity and conductivity. *Nature*, 265:128–129, 1977.
- [107] Matthew A Meitl, Zheng-Tao Zhu, Vipin Kumar, Keon Jae Lee, Xue Feng, Yonggang Y Huang, Ilesanmi Adesida, Ralph G Nuzzo, and John A Rogers. Transfer printing by kinetic control of adhesion to an elastomeric stamp. *Nature materials*, 5(1):33–38, 2006.
- [108] Muhammad Usman Memon, Kenyu Ling, Yunsik Seo, and Sungjoon Lim. Frequency-switchable half-mode substrate-integrated waveguide antenna injecting eutectic gallium indium (EGaIn) liquid metal alloy. *Journal of Electromagnetic Waves and Applications*, 29(16):2207–2215, 2015. doi: 10.1080/09205071.2015.1087347. URL <http://dx.doi.org/10.1080/09205071.2015.1087347>.
- [109] Yitzhak Mendelson. Pulse oximetry: theory and applications for noninvasive monitoring. *Clinical chemistry*, 38(9):1601–1607, 1992.
- [110] Y. Menguc, Y.-L. Park, H. Pei, D. Vogt, P. M. Aubin, E. Winchell, L. Fluke, L. Stirling, R. J. Wood, and C. J. Walsh. Wearable soft sensing suit for human gait measurement. *The International Journal of Robotics Research*, 33(14):1748–1764, 2014. ISSN 0278-3649. doi: 10.1177/0278364914543793. URL <http://ijr.sagepub.com/content/early/2014/11/13/0278364914543793.abstract>.
- [111] Frederick N Meyers, Kenneth J Loh, John S Dodds, and Arturo Baltazar. Active sensing and damage detection using piezoelectric zinc oxide-based nanocomposites. *Nanotechnology*, 24(18):185501, 2013.

- [112] Hadrien O Michaud, Joan Teixidor, and Stéphanie P Lacour. Soft flexion sensors integrating stretchable metal conductors on a silicone substrate for smart glove applications. In *2015 28th IEEE International Conference on Micro Electro Mechanical Systems (MEMS)*, pages 760–763. IEEE, 2015.
- [113] Mohammed G Mohammed and Rebecca Kramer. All-printed flexible and stretchable electronics. *Adv. Mater.*, 29(19), 2017.
- [114] RSC Monkhouse, PD Wilcox, and P Cawley. Flexible interdigital pvdF transducers for the generation of lamb waves in structures. *Ultrasonics*, 35(7):489–498, 1997.
- [115] Willie Bosseau Murray and Patrick Anthony Foster. The peripheral pulse wave: information overlooked. *Journal of clinical monitoring*, 12(5):365–377, 1996.
- [116] Joseph T Muth, Daniel M Vogt, Ryan L Truby, Yiğit Mengüç, David B Kolesky, Robert J Wood, and Jennifer A Lewis. Embedded 3d printing of strain sensors within highly stretchable elastomers. *Advanced Materials*, 26(36):6307–6312, 2014.
- [117] R. Neelakandan and M. Madhusoothanan. Electrical resistivity studies on polyaniline coated polyester fabrics. *Journal of Engineered Fibers and Fabrics*, 5:25–29, 2010.
- [118] Howard R Nicholls and Mark H Lee. A survey of robot tactile sensing technology. *The International Journal of Robotics Research*, 8(3):3–30, 1989.
- [119] X Niu, S Peng, L Liu, W Wen, and P Sheng. Characterizing and patterning of PDMS-based conducting composites. *Advanced Materials*, 19(19):2682–2686, 2007.
- [120] Jin Young Oh, Simon Rondeau-Gagné, Yu-Cheng Chiu, Alex Chortos, Franziska Lissel, Ging-Ji Nathan Wang, Bob C Schroeder, Tadanori Kurosawa, Jeffrey Lopez, Toru Katsumata, Jie Xu, Chenxin Zhu, Xiaodan Gu, Won-Gyu Bae, Yeongin Kim, Lihua Jin, Jong Won Chung, Jeffrey B.-H. Tok, and Zhenan Bao. Intrinsically stretchable and healable semiconducting polymer for organic transistors. *Nature*, 539(7629):411–415, 2016.
- [121] Cagdas D Onal and Daniela Rus. Autonomous undulatory serpentine locomotion utilizing body dynamics of a fluidic soft robot. *Bioinspiration & biomimetics*, 8(2):026003, 2013.
- [122] Johannes T B Overvelde, Yiğit Mengüç, Panagiotis Polygerinos, Yunjie Wang, Zheng Wang, Conor J. Walsh, Robert J. Wood,

- and Katia Bertoldi. Mechanical and electrical numerical analysis of soft liquid-embedded deformation sensors analysis. *Extreme Mechanics Letters*, 1:42–46, 2014. ISSN 23524316. doi: 10.1016/j.eml.2014.11.003.
- [123] Kadri Bugra Ozutemiz, James Wissman, Osman Burak Ozdoganlar, and Carmel Majidi. E-gain–metal interfacing for liquid metal circuitry and microelectronics integration. *Advanced Materials Interfaces*, 5(10):1701596, 2018.
- [124] Rachele N Palchesko, Ling Zhang, Yan Sun, and Adam W Feinberg. Development of polydimethylsiloxane substrates with tunable elastic modulus to study cell mechanobiology in muscle and nerve. *PloS one*, 7(12):e51499, 2012.
- [125] Etienne Palleau, Stephen Reece, Sharvil C Desai, Michael E Smith, and Michael D Dickey. Self-healing stretchable wires for reconfigurable circuit wiring and 3d microfluidics. *Adv. Mater.*, 25(11):1589–1592, 2013.
- [126] Chengfeng Pan, Kitty Kumar, Jianzhao Li, Eric J Markvicka, Peter R Herman, and Carmel Majidi. Visually imperceptible liquid-metal circuits for transparent, stretchable electronics with direct laser writing. *Advanced Materials*, 30(12):1706937, 2018.
- [127] JWC Pang and IP Bond. “Bleeding composites” damage detection and self-repair using a biomimetic approach. *Composites Part A: Applied Science and Manufacturing*, 36(2):183–188, 2005.
- [128] Junyong Park, Shuodao Wang, Ming Li, Changui Ahn, Jerome K Hyun, Dong Seok Kim, Do Kyung Kim, John A Rogers, Yonggang Huang, and Seokwoo Jeon. Three-dimensional nanonetworks for giant stretchability in dielectrics and conductors. *Nat. Commun.*, 3:916, 2012.
- [129] Yong-Lae Park, Carmel Majidi, Rebecca Kramer, Phillippe Bérard, and Robert J Wood. Hyperelastic pressure sensing with a liquid-embedded elastomer. *Journal of Micromechanics and Microengineering*, 20(12):125029, 2010. ISSN 0960-1317. doi: 10.1088/0960-1317/20/12/125029.
- [130] Radhen Patel and Nikolaus Correll. Integrated force and distance sensing using elastomer-embedded commodity proximity sensors. In *Robotics: Science and Systems*, 2016.
- [131] Jason F Patrick, Maxwell J Robb, Nancy R Sottos, Jeffrey S Moore, and Scott R White. Polymers with autonomous life-cycle control. *Nature*, 540(7633):363–370, 2016.

- [132] Samuel A Pendergraph, Michael D Bartlett, Kenneth R Carter, and Alfred J Crosby. Opportunities with fabric composites as unique flexible substrates. *ACS applied materials & interfaces*, 4(12):6640–6645, 2012.
- [133] D Purves, GJ Augustine, D Fitzpatrick, LC Katz, AS LaMantia, JO McNamara, and SM Williams. Neuroscience sinauer associates inc, 2001.
- [134] MJ Regan, H Tostmann, Peter S Pershan, OM Magnussen, E DiMasi, BM Ocko, and M Deutsch. X-ray study of the oxidation of liquid-gallium surfaces. *Physical Review B*, 55(16):10786, 1997.
- [135] Steven Rich, Robert J. Wood, and Carmel Majidi. Untethered soft robotics. *Nature Electronics*, page in press, 2018.
- [136] Omar Rifaie-Graham, Edward A Apebende, Livia K Bast, and Nico Bruns. Self-reporting fiber-reinforced composites that mimic the ability of biological materials to sense and report damage. *Advanced Materials*, 30(19):1705483, 2018.
- [137] John A Rogers, Takao Someya, and Yonggang Huang. Materials and mechanics for stretchable electronics. *Science*, 327(5973):1603–1607, 2010.
- [138] Philipp Rothmund, Alar Ainla, Lee Belding, Daniel J Preston, Sarah Kurihara, Zhigang Suo, and George M Whitesides. A soft, bistable valve for autonomous control of soft actuators. *Science Robotics*, 3(16):eaar7986, 2018.
- [139] Loring B Rowell, Henry L Taylor, Yang Wang, and Walter S Carlson. Saturation of arterial blood with oxygen during maximal exercise. *Journal of Applied Physiology*, 19(2):284–286, 1964.
- [140] Debashish Roy, Jennifer N Cambre, and Brent S Sumerlin. Future perspectives and recent advances in stimuli-responsive materials. *Progress in Polymer Science*, 35(1):278–301, 2010.
- [141] Daniela Rus and Michael T Tolley. Design, fabrication and control of soft robots. *Nature*, 521(7553):467–475, 2015.
- [142] Loren Russell, James Wissman, and Carmel Majidi. Liquid metal actuator driven by electrochemical manipulation of surface tension. *Applied Physics Letters*, 111(25):254101, 2017.
- [143] Donghyeon Ryu and Kenneth J Loh. Strain sensing using photocurrent generated by photoactive p3ht-based nanocomposites. *Smart Materials and Structures*, 21(6):065016, 2012.

- [144] Alireza Pourghorban Saghati, Jaskirat Singh Batra, Jun Kameoka, and Kamran Entesari. Miniature and reconfigurable cpw folded slot antennas employing liquid-metal capacitive loading. *IEEE Transactions on Antennas and Propagation*, 63(9): 3798–3807, 2015.
- [145] Gregor Schwartz, Benjamin C-K Tee, Jianguo Mei, Anthony L Appleton, Do Hwan Kim, Huiliang Wang, and Zhenan Bao. Flexible polymer transistors with high pressure sensitivity for application in electronic skin and health monitoring. *Nature communications*, 4:1859, 2013.
- [146] Robert F Shepherd, Adam A Stokes, Rui Nunes, and George M Whitesides. Soft machines that are resistant to puncture and that self seal. *Advanced Materials*, 25(46):6709–6713, 2013.
- [147] Hristiyan Stoyanov, Matthias Kollosche, Sebastian Risse, Rémi Waché, and Guggi Kofod. Soft conductive elastomer materials for stretchable electronics and voltage controlled artificial muscles. *Advanced Materials*, 25(4):578–583, 2013.
- [148] Martien A Cohen Stuart, Wilhelm TS Huck, Jan Genzer, Marcus Müller, Christopher Ober, Manfred Stamm, Gleb B Sukhorukov, Igal Szleifer, Vladimir V Tsukruk, Marek Urban, et al. Emerging applications of stimuli-responsive polymer materials. *Nature materials*, 9(2):101–113, 2010.
- [149] Y Sun and J. A. Rogers. Structural forms of single crystal semiconductor nanoribbons for highperformance stretchable electronics. *Journal of Materials Chemistry*, 17:832–840, 2007.
- [150] Arya Tabatabai, Andrew Fassler, Claire Usiak, and Carmel Majidi. Liquid-phase gallium–indium alloy electronics with micro-contact printing. *Langmuir*, 29(20):6194–6200, 2013.
- [151] Benjamin CK Tee, Chao Wang, Ranulfo Allen, and Zhenan Bao. An electrically and mechanically self-healing composite with pressure-and flexion-sensitive properties for electronic skin applications. *Nat. Nanotechnol.*, 7(12):825–832, 2012.
- [152] Yaroslav Tenzer, Leif P Jentoft, and Robert D Howe. The feel of MEMS barometers: Inexpensive and easily customized tactile array sensors. *IEEE Robotics & Automation Magazine*, 21(3):89–95, 2014.
- [153] Seppe Terryn, Joost Brancart, Dirk Lefeber, Guy Van Assche, and Bram Vanderborght. Self-healing soft pneumatic robots. *Science Robotics*, 2(9):eaan4268, 2017.

- [154] Patrick Theato, Brent S Sumerlin, Rachel K O'Reilly, and Thomas H Epps III. Stimuli responsive materials. *Chemical Society Reviews*, 42(17):7055–7056, 2013.
- [155] Kevin K Tseng and Liangsheng Wang. Smart piezoelectric transducers for in situ health monitoring of concrete. *Smart Materials and Structures*, 13(5):1017, 2004.
- [156] Ilse M Van Meerbeek, Benjamin C Mac Murray, Jae Woo Kim, Sanlin S Robinson, Perry X Zou, Meredith N Silberstein, and Robert F Shepherd. Morphing metal and elastomer bicontinuous foams for reversible stiffness, shape memory, and self-healing soft machines. *Adv. Mater.*, 28(14):2801–2806, 2016.
- [157] Daniel M Vogt and Robert J Wood. Wrist angle measurements using soft sensors. In *SENSORS, 2014 IEEE*, pages 1631–1634. IEEE, 2014.
- [158] Hongzhang Wang, Bo Yuan, Shuting Liang, Rui Guo, Wei Rao, Xuelin Wang, Hao Chang, Yujie Ding, Jing Liu, and Lei Wang. Plus-m: a porous liquid-metal enabled ubiquitous soft material. *Materials Horizons*, 2018.
- [159] Jiangxin Wang, Guofa Cai, Shaohui Li, Dace Gao, Jiaqing Xiong, and Pooi See Lee. Printable superelastic conductors with extreme stretchability and robust cycling endurance enabled by liquid metal particles. *Advanced Materials*, page in press, 2018.
- [160] M. Wang, C. Trlica, M. R. Khan, M. D. Dickey, and J. J. Adams. A reconfigurable liquid metal antenna driven by electrochemically controlled capillarity. *Journal of Applied Physics*, 117(19):194901, 2015. ISSN 10897550. doi: 10.1063/1.4919605. URL <http://dx.doi.org/10.1063/1.4919605>.
- [161] Qian Wang, Yang Yu, Jun Yang, and Jing Liu. Fast fabrication of flexible functional circuits based on liquid metal dual-trans printing. *Advanced Materials*, 27(44):7109–7116, 2015. ISSN 1521-4095. doi: 10.1002/adma.201502200. URL <http://dx.doi.org/10.1002/adma.201502200>.
- [162] Xiandi Wang, Lin Dong, Hanlu Zhang, Ruomeng Yu, Caofeng Pan, and Zhong Lin Wang. Recent progress in electronic skin. *Advanced Science*, 2(10):1500169, 2015.
- [163] Xuwen Wang, Yang Gu, Zuoping Xiong, Zheng Cui, and Ting Zhang. Silk-molded flexible, ultrasensitive, and highly stable electronic skin for monitoring human physiological signals. *Advanced Materials*, 26(9):1336–1342, 2014.

- [164] Michael Wehner, Ryan L Truby, Daniel J Fitzgerald, Bobak Mosadegh, George M Whitesides, Jennifer A Lewis, and Robert J Wood. An integrated design and fabrication strategy for entirely soft, autonomous robots. *Nature*, 536(7617):451–455, 2016.
- [165] Martin Weigel, Tong Lu, Gilles Bailly, Antti Oulasvirta, Carmel Majidi, and Jürgen Steimle. Iskin: flexible, stretchable and visually customizable on-body touch sensors for mobile computing. In *Proceedings of the 33rd Annual ACM Conference on Human Factors in Computing Systems*, pages 2991–3000. ACM, 2015.
- [166] Scott R White, NR Sottos, PH Geubelle, JS Moore, M\_R Kessler, SR Sriram, EN Brown, and S Viswanathan. Autonomic healing of polymer composites. *Nature*, 409(6822):794, 2001.
- [167] SR White, JS Moore, NR Sottos, BP Krull, WA Santa Cruz, and RCR Gergely. Restoration of large damage volumes in polymers. *Science*, 344(6184):620–623, 2014.
- [168] Kyle A Williams, Andrew J Boydston, and Christopher W Bielawski. Towards electrically conductive, self-healing materials. *J. Royal Soc. Interface*, 4(13):359–362, 2007.
- [169] James Wissman, Michael D Dickey, and Carmel Majidi. Field-controlled electrical switch with liquid metal. *Advanced Science*, 4(12), 2017.
- [170] Zhigang Wu, Klas Hjort, and Seung Hee Jeong. Microfluidic stretchable radio-frequency devices. *Proceedings of the IEEE*, 103(7):1211–1225, 2015.
- [171] Michael W Wukitsch, Michael T Petterson, David R Tobler, and Jonas A Pologe. Pulse oximetry: analysis of theory, technology, and practice. *Journal of clinical monitoring*, 4(4):290–301, 1988.
- [172] Y Xia and J Ouyang. PEDOT:PSS films with significantly enhanced conductivities induced by preferential solvation with cosolvents and their application in polymer photovoltaic cells. *Journal of Materials Chemistry*, 21:4927–4936, 2011.
- [173] Akihiko Yamaguchi and Christopher G Atkeson. Combining finger vision and optical tactile sensing: Reducing and handling errors while cutting vegetables. In *Humanoid Robots (Humanoids), 2016 IEEE-RAS 16th International Conference on*, pages 1045–1051. IEEE, 2016.
- [174] Shanshan Yao and Yong Zhu. Nanomaterial-enabled stretchable conductors: strategies, materials and devices. *Advanced Materials*, 27(9):1480–1511, 2015.

- [175] Tomoyuki Yokota, Peter Zalar, Martin Kaltenbrunner, Hiroaki Jinno, Naoji Matsuhisa, Hiroki Kitanosako, Yutaro Tachibana, Wakako Yukita, Mari Koizumi, and Takao Someya. Ultraflexible organic photonic skin. *Science advances*, 2(4):e1501856, 2016.
- [176] Bin Yu, Lisheng Xu, and Yongxu Li. Bluetooth low energy (ble) based mobile electrocardiogram monitoring system. In *Information and Automation (ICIA), 2012 International Conference on*, pages 763–767. IEEE, 2012.
- [177] Wenzhen Yuan, Chenzhuo Zhu, Andrew Owens, Mandayam A Srinivasan, and Edward H Adelson. Shape-independent hardness estimation using deep learning and a GelSight tactile sensor. *arXiv preprint arXiv:1704.03955*, 2017.
- [178] Hyunwoo Yuk, Teng Zhang, German Alberto Parada, Xinyue Liu, and Xuanhe Zhao. Skin-inspired hydrogel–elastomer hybrids with robust interfaces and functional microstructures. *Nature communications*, 7:12028, 2016.
- [179] Shiming Zhang and Fabio Cicoira. Water-enabled healing of conducting polymer films. *Adv. Mater.*, 2017.
- [180] Yi Zheng, Zhizhu He, Yunxia Gao, and Jing Liu. Direct desktop printed-circuits-on-paper flexible electronics. *Scientific reports*, 3: 1786, 2013.

# 7

## Appendix

### 7.1 *Experimental: Precision Assembly of Multi-Layer Stretchable Electronic Circuits*

**Strain Sensor (CO<sub>2</sub> Laser) Fabrication and Characterization.** A VLS 3.50 30 Watt CO<sub>2</sub> laser system is outfitted with a custom alignment platform (see Figure 2.2 for details) which supports PDMS (Dow Corning Sylgard 184) substrates for laser machining. PDMS is mixed at oligomer-to-curing agent ratios of 5:1, 10:1, 20:1, and 30:1 and are cured at room temperature on a flat, level surface for 48 hours and then post cured in an oven at 70°C for four hours. Sensor material is laminated onto the PDMS substrates and then laser cut with a predefined pattern. When placing the conductive eCAP layers the microfiber direction is orientated orthogonal to the intended primary stretching direction. After laser cutting, excess material is stripped off and any release liners are removed by cleaning the surface with IPA and then adhesive tape is used to remove all release liners simultaneously. Layers are then assembled on alignment pegs that interface with a hole and slot in the substrate. Pressure is applied with a roller to ensure adhesive contact between layers and then the upper substrate is peeled off to transfer the patterned elements. Specific laser cutting conditions are provided in Table 7.1.

Strain sensors were evaluated on a materials testing machine (Instron 5969) with custom 3D printed grips to hold the sample and provide electrical contact between the sample and external leads. The sensors were  $18 \pm 1$  mm long, 6.5 mm wide, and 1.8 mm thick. Capacitance is measured with a benchtop LCR/ESR meter (BK Precision 889B) at a frequency of 200 KHz and a voltage of 1 V through the remote interface mode. Extension rates were  $20 \text{ mm}\cdot\text{min}^{-1}$ ,  $10 \text{ mm}\cdot\text{min}^{-1}$ , and  $5 \text{ mm}\cdot\text{min}^{-1}$  for the 100% strain cyclic testing, hysteresis testing, and strain and hold testing respectively. High cycle testing was performed on an orbital jigsaw (Black and Decker BDEJS600C) at 5 Hz on a setup previously described<sup>[132]</sup>.

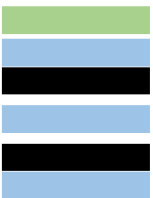
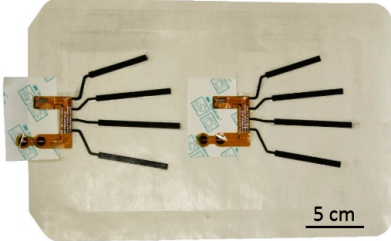
Strain sensors	Substrate	Films	Laser Conditions (Power/speed)	Completed image
	5:1	VHB, eCAP	(100/10)	
	5:1	VHB	(100/40)	
	30:1	VHB, eCAP	(100/10)	
Sensor glove	Substrate	Films	Laser Conditions (Power/speed)	Completed image
	20:1	Component Stencil, Blaze Orange	(100/50)	
	5:1	eCAP	(100/40)	
	5:1	Tegaderm	(60/100)	
	30:1	Tegaderm, eCAP	(80/15)	

Table 7.1: CO<sub>2</sub> fabrication conditions- (top) Sensor array, (bottom) Integrated sensor skin

**Transfer Printing Adhesion Characterization.** Adhesion behavior of the soft transfer printing process was investigated under 90° peel adhesion experiments. The samples consisted of a 0.5 mm thick VHB acrylic tape with a bonded eCAP layer to match the laser cutting conditions for the assembly process. The samples were 0.65 mm thick, had a width of 5.5 mm, and an inextensible film was bonded after laser cutting for testing. The samples were examined with a materials testing machine (Instron 5969) at an extension rate of 50 mm/min on a linear bearing to maintain a 90° angle while peeling. The test was conducted on four different PDMS (Dow Corning Sylgard 184) substrates with oligomer-to-curing agent ratios of 5:1, 10:1, 20:1, and 30:1 with the number of laser cutting passes varying from 0 to 4 as described in Section 2.3.

**Integrated Sensor Skin and Capacitance Measurement.** Based on the operation of the capacitance to digital converter (CDC), both electrodes of the strain sensor were routed to different channels on the CDC to provide redundancy. The raw capacitance for each channel is transmitted wirelessly at 10 Hz to the host computer using the BLE protocol. The integrated sensing skin is powered from a CR1220 Lithium coin cell battery (3V 40mAh). The charge/discharge current and frequency for each channel was set to 16  $\mu$ A and 500 kHz respectively.

A baseline subtraction function is first applied to the raw capacitance signal (window size: 500, step size: 100), grounding the signal

and exposing the dominant peaks. The MATLAB peak finding function is used to find the local maxima and minima. A local maximum is considered to be an actuation point if the nearest local minimum on both sides of the local maximum are below zero. A Gaussian curve is then fit to all points surrounding the local maximum that are greater than 5 pF.

**Skin Mountable Pulse Oximeter and Photoplethysmogram Signal Measurement.** The skin mountable device was designed using a fully integrated pulse oximeter sensor solution (Maxim MAX30100), which combines two LEDs, a photodetector, optics, and low-noise analog signal processing. To minimize the number of bus wires, the supply voltage is regulated on the skin mountable device. The pull-up resistors for the I<sup>2</sup>C bus are also included on the device. Due to the small pad area, the pulse oximeter and voltage regulator was populated on a flexible carrier board to increase the overlap area between the device and interconnects. Decoupling capacitors were added to both carrier boards to ensure a steady voltage supply. The pulse oximeter was digitally interfaced to the Bluetooth module.

The pulse oximeter was powered from two CR1220 Lithium coin cell batteries (3V 40mAh). Two coin cell batteries were used to ensure 3.3V was supplied to the device. The device was configured to collect data from the IR and red LED at 200 Hz with a pulse width of 400  $\mu$ s, and LED current level of 20.8 mA with 14-bits of resolution. At 15 Hz, the raw PPG signal from the IR and red LED is combined into three 20-byte words and wirelessly transmitted to the host computer using the BLE protocol.

**Bluetooth Module and Wireless Communication.** The Bluetooth module was designed around a BLE system on a chip (SoC) (Nordic nRF51822) that incorporates a 32-bit ARM processor and ultra-low power multi-protocol 2.4GHz RF transceiver. The SoC is interfaced with a pair of 12 channel CDCs (Freescale MPR121) to process the capacitive strain sensors. An ancillary power management circuit is shared across all devices to reduce overall size. A fine-pitch, low-profile board-to-board connector is used to interface to the wearable bio-monitoring devices. The BLE standard, sometimes referred to as Bluetooth Smart, was used to wirelessly transmit the data collected from the wearable bio-monitoring devices. The Bluetooth module uses a Generic Attribute Profile (GATT) with custom Services and Characteristics, which is configured as a peripheral device that can establish a connection with a central device such as a smartphone, tablet, or computer. Depending on the wearable bio-monitoring device, multiple packets are transmitted over BLE between 10-15 Hz.

**Pulse Oximeter (UV Laser) Fabrication.** A LPKF ProtoLaser U3 UV laser micromachining system was used with camera based fiducial recognition to automatically and reliably locate the position of PDMS substrates that have fiducials machined into the substrate. The fiducials are precisely placed relative to the hole and slot that is used for alignment during the adhesive transfer process. PDMS is mixed at oligomer-to-curing agent ratios of 5:1, 10:1, and 20:1 and are cured at room temperature on a flat, level surface for 48 hours and then post cured in an oven at 70°C for 4 hours. Interconnect material is laminated onto the PDMS substrates, the fiducials are automatically located, and the material is laser cut with a predefined pattern. After laser cutting, excess material is stripped off and any release liners are removed. Individual stencils were patterned out of release liner for the transfer of the rigid electrical components. Layers are then assembled on alignment pegs which interfaces with a hole and slot in the substrate. Pressure is applied to the top substrate to ensure adhesive contact between layers and then the upper substrate is peeled off to transfer the patterned elements. Specific laser cutting conditions are provided in Table 7.2.

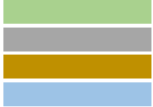
Wearable pulse oximeter	Substrate	Films	Laser Conditions (Power[W]/speed[mm/s]/repetitions)	Completed image
	5:1	Component Stencil, stacked release liner	(5.2/150/50)	
	10:1	Z-film	(5.2/200/48)	
	10:1	Flexible copper-clad	(2/135/18)	
	20:1	Tegaderm	(N/A)	

Table 7.2: UV fabrication conditions- Pulse oximeter

**Pulse Oximeter Experiments.** The wearable pulse oximeter device was laminated onto the index finger of a test subject with medical grade adhesive (3M Tegaderm). Cycling experiments were performed on a stationary trainer (CycleOps Fluid) and pulse oximeter data is collected at 200 Hz and transmitted wirelessly using the BLE protocol at 15 Hz. Power and cadence were measured with a hub based power meter (PowerTap Pro+) and a second, chest strap heart rate monitor (Garmin) was also utilized. These signals are recorded at a frequency of 1 Hz. During the test cycling power starts at 0 W for 30 s and is then stepped up to 100 W for 60 s, increased to 200 W for 180 s, stepped

back to 100 W for 60 s, and then 0 W for 30 s. Heart rate from the pulse oximeter is calculated from the maximum peak between 0.5 and 10 Hz of a FFT at 10 s intervals. SpO<sub>2</sub> is calculated by first normalizing the PPG signals by dividing by the DC offset. The maximum peak-to-peak distance per heart beat is then found and the optical density ratio (R) is calculated (the ratio of the peak-to-peak distance of the red to IR LED)<sup>[17,44]</sup>. The SpO<sub>2</sub> can be calculated based on the empirical calibration of R. For this experiment, the linearization of the standard model for computing SpO<sub>2</sub> that is often used within literature was used<sup>[44]</sup>.



## 7.2 *Experimental: Stretchable Electronics with Liquid Metal Interconnects*

**Soft PCB Fabrication** A layer of PDMS (10:1 base-to-curing agent ratio; Sylgard 184, Dow Corning) is applied on a glass disc substrate by spin coating (KW-4A, SPI) at 1500 RPM for 10s and cured at 100°C for 20 min. Next, a polymer film (Laser-Tape, Ikonics) is placed on top of the PDMS layer and the film is patterned using the UVLM to create placement openings for the rigid integrated circuits (ICs), as well as fiducials for alignment within the UVLM (Figure 3.2A). Surface-mount SSTs are then placed into the openings (Figure 3.2B). The board side of the components are dipped in PVA (5%, Ward's Science), to adhere the components to the glass disc. After PVA curing at 70°C for 5 min on a hotplate, the SSTs are sealed with a second layer of PDMS (10:1). Multiple sealing layers are spin-casted (600 RPM, 5s) and cured (100°C, 20 min) until the surface mount components are covered. The SST-embedded elastomer is then peeled from the substrate and placed on the glass disc with the board side of the components exposed. The exposed components are rinsed with deionized water to remove the PVA (Figure 3.2C). After drying, a layer of zPDMS is deposited on top of the exposed SSTs by spin coating (1500 RPM for 10s; KW-4A, SPI) and cured on top of a flat magnet ( $\sim 1448$  Gauss,  $2 \times 2 \times 0.25$  in. Nd-FeB; K&J Magnetics, Inc.) at 100°C for 20 min (Figure 3.2D). The zPDMS is prepared by mixing 70wt% of 40  $\mu\text{m}$  diameter Ag-coated  $\text{Fe}_2\text{O}_3$  particles (20% Ag by wt.; SM40P20, Potters Industries LLC) with 30 wt% of EGaIn (75 wt% Ga and 25 wt% In; Gallium Source) using a mortar and pestle. The  $\mu$ -sphere/EGaIn mixture is then mixed at 50 wt% with uncured PDMS (10:1). After curing, a film of EGaIn is then deposited onto the cured zPDMS by rolling using a cylinder of PDMS (Figure 3.2E). Lastly, the EGaIn film is patterned with the UVLM system and then coated with a sealing layer of PDMS (10:1) (Figure 3.2F). Multiple sealing layers are spin-casted (600 RPM, 5s) and cured (100°C, 20 min) to match the thickness of the SST-embedded elastomer layer.

**Characterization** A multi-terminal EGaIn resistor was fabricated to determine the influence of trace length on resistance. The trace is made with two different widths (100 and 200  $\mu\text{m}$ , four samples for each trace width) and the measurements are taken between the terminal on the upper left terminal and one of the terminals on the right side by direct contact with the probes of a multimeter. Electrical resistance is measured for the following trace lengths: 5, 14.6, 24.2, 33.8, 43.4, 53, 62.6 mm. Measurements of resistance versus length (Figure 3.5B) show high linearity with  $R^2$  values greater than 0.96. The linear curves fitted for all the measured resistances (in  $\Omega$ ) of 100  $\mu\text{m}$ -wide and 200  $\mu\text{m}$ -

wide traces are  $R_{100} = 0.1615x + 0.3713$  and  $R_{200} = 0.055x + 0.2493$ , respectively, where  $x$  is the length of circuit (in mm).

Capacitors with interdigital electrodes are produced and tested to further examine the electrical properties of the UV laser-patterned traces and zPDMS. One group of the capacitors consist of four pairs of  $250 \mu\text{m}$ -wide and  $150 \mu\text{m}$ -spaced electrodes with different lengths  $\ell$  of overlap (5, 7, 8, 9 mm; nine samples for each electrode length). The electrodes are patterned on a  $120 \mu\text{m}$  thick zPDMS substrate. Similar to the resistance measurements, the capacitance is measured by directly touching the terminals with the probes of an LCR/ESR meter (889B, BK Precision). Measurements of capacitance versus length are presented in Figure 3.5C and fitted to the following theoretical model<sup>[40]</sup>:

$$C \approx \left\{ (n-3)\varepsilon_{en} \frac{K(k_0)}{K(k'_0)} + 4\varepsilon_{e3} \frac{K(k_{03})}{K(k'_{03})} \right\} \varepsilon_0 \ell$$

Here,  $K$  is the complete elliptical integral of the first kind, where  $k_0$  and  $k_{03}$  are calculated based on the dimensions of the interdigitated capacitor and substrate:

$$k_0 = \frac{s}{s+g},$$

$$k_{03} = \frac{s}{s+2g} \sqrt{\frac{1 - \left(\frac{s+2g}{3s+2g}\right)^2}{1 - \left(\frac{s}{3s+2g}\right)^2}},$$

and  $k'_0 = \sqrt{1 - k_0^2}$ ,  $k'_{03} = \sqrt{1 - k_{03}^2}$ . Here,  $g$  is half of the gap space between electrodes, and  $s$  is half of the effective width. The effective width of electrodes is

$$2s = 2s_g + \frac{t}{\pi} \left\{ 1 + \ln \left( \frac{8\pi s_g}{t} \right) \right\},$$

where  $2s_g$  and  $t$  are the geometric (physical) width and thickness, respectively, of the electrodes. The electrode of the capacitors we tested has width of  $250 \mu\text{m}$ , and the thickness is roughly estimated as  $20 \mu\text{m}$  based on the calculation from resistive tests, and this yield an effective width of  $\sim 288 \mu\text{m}$ . The thickness of zPDMS before and after UV laser patterning is  $\sim 120$  and  $100 \mu\text{m}$ . The glass disc has a thickness of  $3.3 \text{ mm}$  with an estimated relative permittivity of 4.6 (Pyrex 7740 Borosilicate Glass, Corning). Based on a slope  $0.21 \text{ pF/mm}$  for the fitted curve ( $0.2065 \text{ pF/mm}$ ), the relative electrical permittivity of zPDMS is estimated to be 5.6. The configuration of the interdigital capacitor is shown in Figure 7.1.

**Circuit Implementation** A fully integrated pulse oximeter sensor solution (MAX30100; Maxim Integrated Products, Inc.) is used to collect the PPG waveforms. Pulse oximetry is performed with a system-on-a-chip (SoC) that contains a red and IR LED, a photodetector, optics,

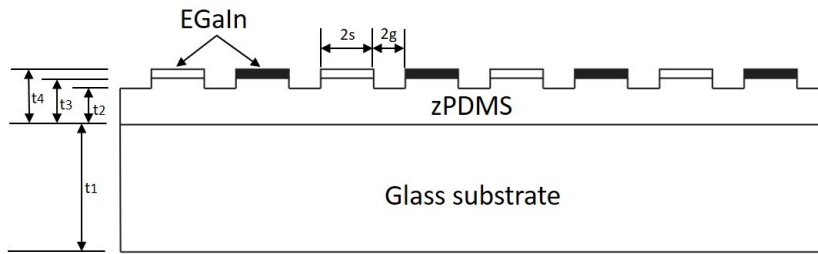


Figure 7.1: Configuration of the interdigitated capacitor. The thickness of the glass substrate is  $t_1 = 3300 \mu\text{m}$ . The thickness of the unablated zPDMS is  $t_3 = 120 \mu\text{m}$ . The thickness of the ablated portions of the zPDMS is  $t_2 = 100 \mu\text{m}$ . The thickness  $t_4 = 140 \mu\text{m}$  corresponds to the sum of thicknesses of  $t_3$  and the EGaln electrodes,  $t_E$  ( $\sim 20 \mu\text{m}$ ). The geometric width of the electrodes is  $2s = 250 \mu\text{m}$  and the gap between the electrodes is  $2g = 150 \mu\text{m}$ .

and low-noise analog signal processing. To minimize the number of bus wires, the supply voltage (1.8 volts) was regulated at the device level. The pull-up resistors for the I<sup>2</sup>C bus and decoupling capacitors were also included within the soft-matter circuit. The pulse oximeter was digitally interfaced to a Bluetooth module to transmit signals to a host computer for signal processing<sup>[100]</sup>. The device was configured to collect the PPG waveforms at 200 Hz with LED pulse width of 400  $\mu\text{s}$  and current of 20.8 mA with 14-bits of resolution. Circuit diagrams of the pulse oximeter and an LED array are presented in Figure 7.2.

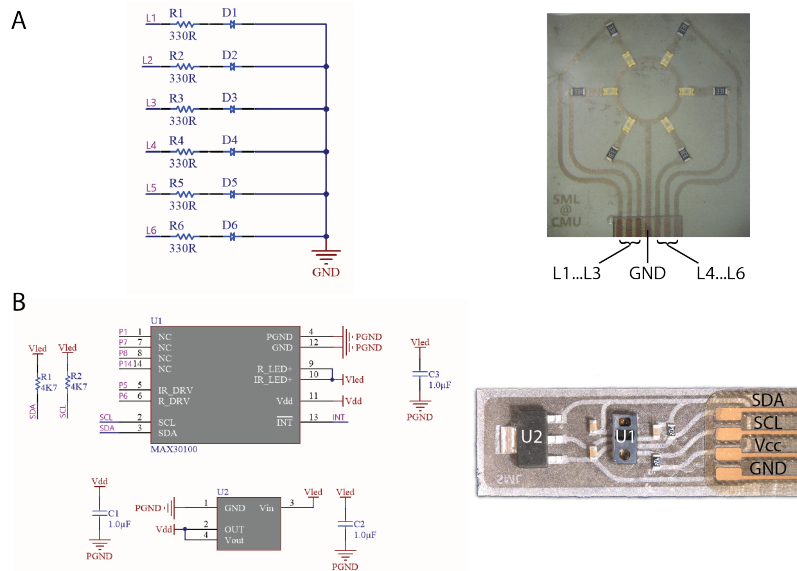


Figure 7.2: Soft-matter printed circuit board schematic. (A) Circuit schematic of LED array. The device consists of a circular array of six LED resistor pairs. (B) Circuit schematic of pulse oximeter. The device consists of a fully integrated pulse oximeter sensor solution (U1, MAX30100, Maxim Integrated Products, Inc.), low dropout regulator (U2, AZ1117CH-1.8TRG1, Diodes Inc.), I<sup>2</sup>C bus pull-up resistors, and decoupling capacitors.



### 7.3 Experimental: Autonomously Self-Healing Soft-Matter Electronics

**Fabrication** PDMS (Sylgard 184, Dow Corning) was prepared at a 5:1 oligomer-to-curing agent ratio using an AR-100 THINKY planetary centrifugal mixer (mixing: 1 min, defoaming: 1 min). Gallium and indium were purchased from Solution Materials, LLC and combined at 75% Ga, 25% In by weight to produce EGaIn. The LMEE was fabricated by combining PDMS and EGaIn at LM loadings  $\phi = 20, 30, 40,$  and  $50\%$ , which corresponds to a LM-to-elastomer mass fraction of 1.61:1, 2.76:1, 4.30:1, and 6.44:1. The emulsion was mixed by hand until no large droplets of EGaIn were visually present and then mixed using the planetary mixer (mixing: 1 min). After mixing, the composite could be cast or molded and subsequently cured. For all materials presented, stencil lithography was used to pattern both bulk sheet and selectively patterned demonstrations (Blazer Orange Laser Mask, IKONICS Imaging). First, a  $300\ \mu\text{m}$  layer of PDMS was cast on the polyethylene substrate and cured at  $100^\circ\text{C}$  for 30 minutes using a thin film applicator (ZUA 2000, Zehntner). The substrate was allowed to cool and a  $550\ \mu\text{m}$  layer of LMEE was cast on top of the PDMS layer using a stencil mask, the mask was removed, and the layer was cured at  $100^\circ\text{C}$  for 1 hour. LM loading of  $\phi = 50\%$  was used for all experiments unless otherwise noted. In practice, a 2D plotter is used to create the circuit on the exposed composite and then the circuit is sealed in insulating rubber (Sylgard 184, Dow Corning; cured at  $100^\circ\text{C}$  for 30 mins) to prevent further trace formation.

**Material activation.** The material was activated using a 2D plotter and scoring stylus by applying local pressure (Cricut Explore, Cricut). The scoring stylus was clamped within the cutting holder approximately 5.6 mm from the base. (Figure 7.3). First, the material was adhered to the standard grip cutting mat, a custom tool (pressure: 150, passes: 5) was used to write the pattern, and the 2D plotter was operated as described within the user manual. See Movie S1 for more details. Any LM residue on the surface was cleaned using a cotton tip applicator and isopropyl alcohol.

**Self-healing response.** The change in resistance of the LMEE trace can be modeled by:  $\Delta R = R_{eq} - R_t$ , where  $R_t$  is the resistance of the trace that was removed and  $R_{eq}$  is the resistance of the hole:

$$R_{eq} = \frac{R_1 R_2}{R_1 + R_2}$$

$$R_1 = \alpha P \left( \frac{\rho}{A} \right) \quad R_2 = (1 - \alpha) P \left( \frac{\rho}{A} \right) \quad 0 < \alpha < 1$$

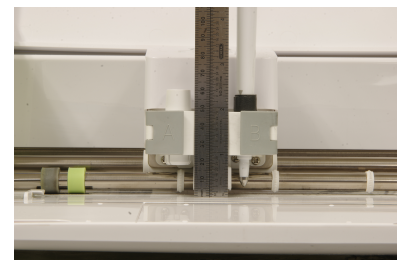


Figure 7.3: Scoring Stylus mounted in X-Y plotter. Photograph of the scoring stylus mounted within the Cricut Explorer. The scoring stylus is placed approximately 5.6 mm from the base.

$$R_t = L_t \left( \frac{\rho}{A} \right)$$

$P$  is the perimeter of the hole,  $\alpha$  is the percentage of the perimeter on one side of the trace, and  $L_t$  is the length of the trace that was removed.

$$\Delta R = \frac{\alpha P \left( \frac{\rho}{A} \right) (1 - \alpha) P \left( \frac{\rho}{A} \right)}{\alpha P \left( \frac{\rho}{A} \right) + (1 - \alpha) P \left( \frac{\rho}{A} \right)} - L_t \left( \frac{\rho}{A} \right)$$

$$\Delta R = \frac{\alpha(1 - \alpha) P^2 \left( \frac{\rho}{A} \right)^2}{P \left( \frac{\rho}{A} \right)} - L_t \left( \frac{\rho}{A} \right)$$

$$\Delta R = \left( \frac{\rho}{A} \right) (\alpha(1 - \alpha) P - L_t) = 0$$

The condition for constant resistance after damage, assuming constant resistivity, is found to be:

$$\alpha P(1 - \alpha) = L_t$$

**Pressure activation.** To experimentally characterize the force required to induce internal rupture, a glass cylindrical indenter ( $R = 1.5\text{mm}$ ;  $L = 10\text{mm}$ ;  $E = 70\text{GPa}$ ) was positioned across two closely-neighboring traces (5 mm trace spacing) and pressed into the composite ( $\phi = 50\%$ ) until undesired activation between neighboring traces was achieved. The experiment was performed on a universal testing machine (5969, Instron) at a compressive rate of  $1\text{mm min}^{-1}$ . The activation between neighboring traces was monitored using a digital to analog converter (USB-6002, NI). The recorded force,  $F$ , at undesired activation was converted to pressure using Hertzian contact mechanics<sup>[45]</sup>, where the maximum pressure is:

$$p = \left( \frac{E^* F}{\pi L R} \right)^{1/2}$$

where

$$\frac{1}{E^*} = \frac{1 - \nu_1^2}{E_1} + \frac{1 - \nu_2^2}{E_2}$$

and

$$\frac{1}{R} = \frac{1}{R_1} + \frac{1}{R_2}, \quad R_2 = \infty, \quad R = R_1$$

**Repeated compressive loading.** To experimentally characterize the composite under repeated compressive loading, a glass cylindrical indenter ( $R = 1.5\text{mm}$ ;  $L = 10\text{mm}$ ;  $E = 70\text{GPa}$ ) was positioned across two closely-neighboring traces (5 mm trace spacing) and pressed into the composite ( $\phi = 50\%$ ) until a force of 35 N was reached for 1 000 loading cycles. Upon completion of cyclic compressive loading, the indenter was indented into the material until unintended activation occurred at 37.3 N.

**Shear activation.** Lap shear experiments were also completed using the universal testing machine. The LMEE composite with closely-neighboring traces (2.5 mm trace spacing) was glued (SilPoxy, Smooth-On) to an acrylic sheet (25x100mm), placed in contact with an opposing acrylic sheet (25x100mm) with an initial overlap of 40mm, and pulled apart at a rate of  $10\text{mm min}^{-1}$ , Supplementary Fig. 7.4. The activation between neighboring traces was monitored using a digital to analog converter (USB-6002, NI). The maximum applied force was used to calculate the applied shear stress:  $F/w \cdot h$ . The applied force is shown in Supplementary Fig. 7.4.

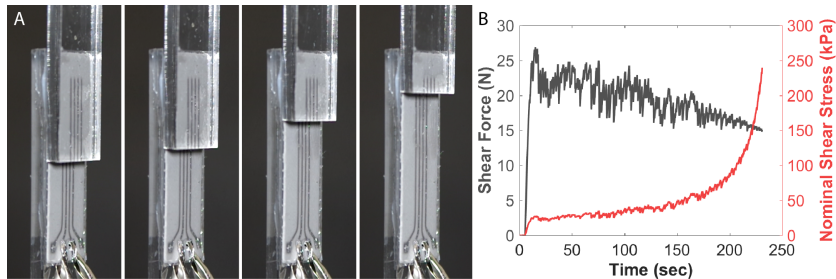


Figure 7.4: Single lap shear. (A) Photograph sequence of a lap shear experiment. (B) Plot of applied shear force and nominal shear stress ( $F/(w \cdot (L - \Delta L))$ ) versus time. No unintended activation occurred between closely-neighboring traces (2.5 mm trace spacing, no elastomer sealing layer).

Four parallel traces with a 2.5mm center-to-center spacing were patterned on the LMEE composite and sealed with a 1mm thick elastomer layer. An abrasive shear force was applied using a scouring pad (86 heavy duty scouring pad, 3M), Supplementary Fig. 7.5. The conductivity between traces was monitored using a hand-held multimeter (TOL-12967, Sparkfun).

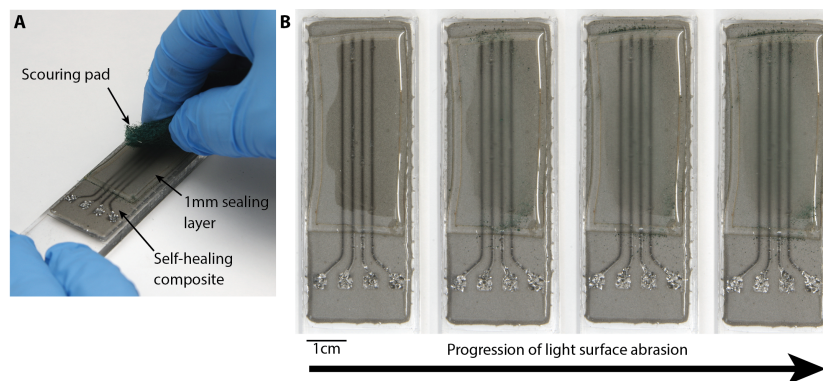


Figure 7.5: Abrasive shear force. From left to right, photograph of varying degrees of applied abrasive shear force using scouring pad. No unintended activation occurred between closely-neighboring traces (2.5 mm trace spacing, 1 mm elastomer sealing layer).

To experimentally characterize the shear force required to induce internal rupture, an indenter with ball-point set screw tip ( $R=2\text{mm}$ ) was pressed into the composite ( $\phi = 50\%$ ) and a tangential shear force was applied manually, shearing the indenter across two closely-neighboring

traces (2.5 mm trace spacing). The indenter was gradually pressed into the composite and tangentially sheared until undesired activation between neighboring traces was achieved, Figure 7.6A-D. The experiment was performed on a universal testing machine (5969, Instron). The activation between neighboring traces was monitored using a digital to analog converter (USB-6002, NI). The material was characterized with a 0, 1, and 3mm elastomer sealing layer, Figure 7.6E. The applied normal force,  $F$ , that resulted in unintentional trace formation was converted to applied stress using Hertzian contact theory<sup>[58]</sup>, where the contact radius,  $a_0$ :

$$a_0 = \left( \frac{3\pi}{4} (k_1 + k_2) RF \right)^{1/3}$$

where  $k_1$  and  $k_2$  are the elastic constants of the material:

$$k_1 = \frac{1 - \nu_1^2}{\pi E_1} \quad \text{and} \quad k_2 = \frac{1 - \nu_2^2}{\pi E_2}$$

where  $\nu$  is the Poisson ratio and  $E$  the Young modulus of each material. The average and maximum contract pressure is given by:

$$p_{avg} = \frac{F}{\pi a_0^2} \quad \text{and} \quad p_{max} = \frac{3F}{2\pi a_0^2}$$

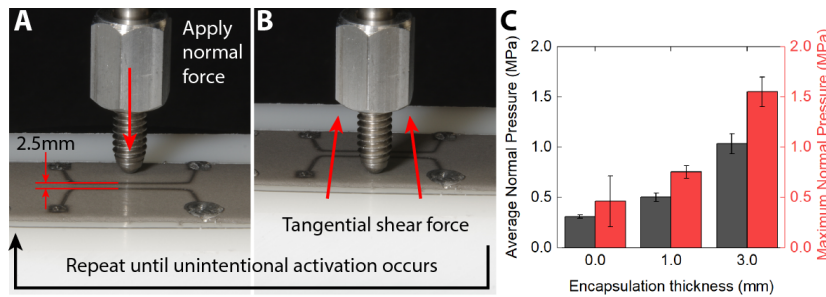


Figure 7.6: Spherical indenter with tangential shear force. (A) Spherical indenter (4mm diameter) is pressed into the LMEE composite. (B) A tangential shear force is manually applied, shearing the spherical indenter across two closely-neighboring traces (2.5 mm trace spacing). If no unintended activation occurs between the neighboring traces, the indenter normal force is increased and a tangential shear force is manually applied in the opposite direction. This is repeated until unintended activation occurs. (C) Plot of applied normal stress for different encapsulation thicknesses ( $t = 0, 1, \text{ and } 3 \text{ mm}$ ) that causes unintended trace formation when the spherical indenter is tangentially sheared across closely-neighboring traces. The applied normal force is measured immediately after activation at the center of the closely-neighboring traces.

**Bending activation** A hinge was created by bonding two acrylic sheets (25x75mm) to a single sided tape (Tegaderm, 3M). The LMEE composite patterned with closely-neighboring traces (2.5 mm trace spacing) was bonded to the elastomer tape using double sided tape (Scotch, 3M). The conductivity between traces was monitored using a hand-held multimeter (TOL-12967, Sparkfun).

**Soft robot fabrication** The limbs of the soft quadruped use a shape memory alloy (SMA) wire (0.3mm diameter, Dynalloy) embedded within thermal tape (H48-2, T-Global). The SMA wire is bent into a U-shape with sharp corners (width=13mm, length=55mm) and bonded to thermal tape (length=55mm, width=22mm, thickness=0.5mm) using a thin

layer ( $200\mu\text{m}$ ) of partially cured silicone elastomer (Ecoflex 00-30, Smooth-On; 7 minutes at  $50^\circ\text{C}$ ). A second layer of silicone elastomer ( $400\mu\text{m}$ ) is applied to the stack and partially cured (7 minutes at  $50^\circ\text{C}$ ). In parallel a  $200\mu\text{m}$  layer of silicone elastomer is partially cured on pre-stretched ( $\lambda = 1.5$ ) thermal tape (length= $70\text{mm}$ , width= $60\text{mm}$ , thickness= $0.5\text{mm}$ ). After curing, the layers are clamped together with binder clips and fully cured at  $50^\circ\text{C}$  for 10 minutes. The excess material is cut off along the outline of the unstretched thermal tape layer. The soft actuator layer stack is shown in Figure 7.7A.

Each of the limbs are glued (All purpose Krazy Glue) to an acrylic frame. Noninsulated wire ferrules are crimped the the ends of the SMA wire and soldered to ring terminals that are mechanically fixed to the acrylic frame using bolt and nut fasteners. The fasteners provide an electrical connection to the LMEE sheet similar to a via within a printed circuit board. The LMEE sheet is placed over the bolts and nuts are used as a clamp to mechanically and electrically connect the LMEE sheet to the acrylic frame, SMA actuators, and control board. A cross-section view of the electrical and mechanical connection and general dimensions of the acrylic frame are shown in Figure 7.7B-C.

**Soft robot control** The soft robot has on-board control electronics with transistor switches to control the power delivered to each of the soft SMA actuators (Figure 4.11B). The control board is built around an ultra-low power Bluetooth Low Energy (BLE) SoC with Cortex-M4F processor (nRF52, Nordic). The control board includes power management circuitry (3v) and transistor switches (NPN, 20v, 6.5A). Power is delivered to the board using a tether from a bench top power supply (DIGI 360, Electro Industries). High (start/stop) and low (actuation and cooling time) level commands are sent using a custom BLE service.

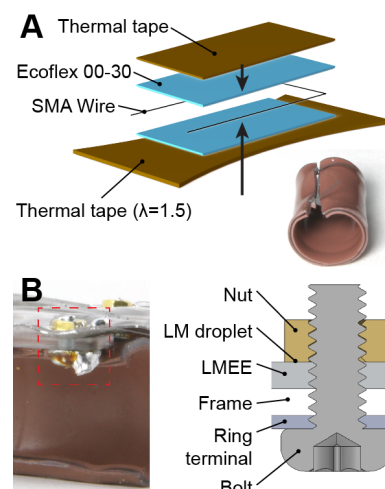


Figure 7.7: Soft robot construction. (A) (top-left) Layer stack of soft actuator construction and (bottom-right) photograph of fabricated limb. (B) (left) Photograph of the mechanical and electrical connection within the soft robot and (right) cross sectional view and description of the layer stack.



#### 7.4 *Experimental: Damage Sensing Soft-Matter Composite*

**Fabrication.** Sylgard 184 (Dow Corning) was prepared per manufacturer's directions by mixing 10:1 oligomer-to-curing agent ratio in a planetary centrifugal mixer, unless otherwise noted. The Sylgard 184 5:1 specimens were prepared by mixing 5:1 oligomer-to-curing agent ratio. Sylgard 527 (Dow Corning) was prepared per manufacturer's directions by mixing equal weights of part A and B in a planetary centrifugal mixer. The elastomer blends were prepared by mixing 80, 60, 40, and 20% weight percent of Sylgard 184 to Sylgard 527 in a planetary centrifugal mixer. Gallium and indium were purchased from Solution Materials, LLC and combined at 75% Ga, 25% In by weight to produce EGaIn. The LM-elastomer composite was fabricated by combining uncured silicone with EGaIn at a 1:1 volume loading. The prepolymer and LM were mixed until an emulsion was formed and no large droplets of LM were visually present. The emulsion was then further mixed using a planetary mixer. After mixing, the composite was cast or molded and subsequently cured (100°C, 1 hour).

**Mechanical characterization.** Samples were cast in acrylic molds ( $t = 1$  mm) using a dogbone specimen geometry (Die B, ASTM D412A) and tested on a materials testing machine (5969, Instron) at a strain rate of  $100 \text{ mm}\cdot\text{min}^{-1}$ . To prevent slipping, the samples were glued (Sil-Poxy, Smooth-On) to 6 mm thick acrylic plates and allowed to cure overnight. The LM-elastomer composite was coated on ripstop Nylon (xprd560961, Jo-Ann Fabrics). A dogbone specimen geometry was cut from the sheet using a UV laser cutter (U3 protolaser, LPKF).

**Electrical characterization.** Activation strain: Samples were cast in acrylic molds ( $t = 1$  mm) using a dogbone specimen geometry (Die B, ASTM D412A) and tested on a materials testing machine (5969, Instron) at a strain rate of  $100 \text{ mm}\cdot\text{min}^{-1}$ . The tabs of the specimen were activated to the gauge by manually applying pressure. The samples were then glued (Sil-Poxy, Smooth-On) to 6 mm thick acrylic plates and allowed to cure overnight, with the electrical contact outside of the clamping area to reduce possible artifacts. The conductivity between the tabs was monitored using a Universal Serial Bus (USB) DAQ (USB-6002, NI).

Activation force: The LM-elastomer composite was cast in square acrylic molds ( $t = 500 \mu\text{m}$ ). Traces were drawn into the material using a ball point pen with a center-to-center spacing of 5 mm. The samples were then encapsulated with a  $500 \mu\text{m}$  layer of 10:1 Sylgard 184 (cured at 100°C for 30 minutes). A glass cylindrical indenter (3 mm diameter) was pressed into the composite at a rate of  $0.01 \text{ mm}\cdot\text{sec}^{-1}$ . For cut activation, a precision knife was used to cut across two adjacent traces. The conductivity between adjacent lines was monitored using an USB

DAQ (USB-6002, NI).

**Active-matrix grid of LM.** For 1D samples, a grid of LM was spray deposited<sup>[57]</sup> onto the LM-elastomer composite using a stencil mask (Blazer Orange Laser Mask, IKONICS Imaging). Conductive fabric tape (CN-3490, 3M) was used to interface the LM traces with hook up wiring. The circuit schematic for 1D damage detection is shown in Figure 7.13.

For 2D samples, a grid of LM was spray deposited<sup>[57]</sup> onto an elastomer sealing layer using a stencil mask (Blazer Orange Laser Mask, IKONICS Imaging). The LM-elastomer layer was deposited on top of the grid using a thin film applicator (ZUA 2000, Zehntner) and cured (100°C, 1 hour). A grid of LM was then spray deposited<sup>[57]</sup> onto the LM-elastomer composite. Conductive fabric tape (CN-3490, 3M) was used to interface the LM traces with hook up wiring. For detecting and localizing damage an electronic switch (CD74HC4067SM96, TI) is used in a Multiplexer/Demultiplexer configuration as shown in Figure 5.7B. A microcontroller (ATMega 328) is used to interface with a computer using the USB. The data was plotted using server-side JavaScript (Node.js).

**Soft robot fabrication.** The soft robot mimic is constructed from a fabric suit (inflatable full body suit, Rubie's), two squirrel cage fans (11270, SparkFun Electronics) that continuously run to compensate for leaks within the fabric suit, and a PVC skeleton to support the fabric suit Figure 7.12. A Bluetooth low energy (BLE) UART module (nRF51, Nordic) is connected to the microcontroller, enabling wireless data transmission to a mobile computing platform (Pixel C, Google). The estimated damage is calculated and sent to a second microcontroller (ATMega 328) with a BLE UART module. A DC motor driver (DRV8871, TI) is used to control the velocity of the fans used for inflation. The circuit is powered using two lithium ion batteries (3.7v, 2000mAh) connected in series. The internal structure pressure is monitored using a high resolution, absolute barometric pressure sensor (BMP280, Bosch).

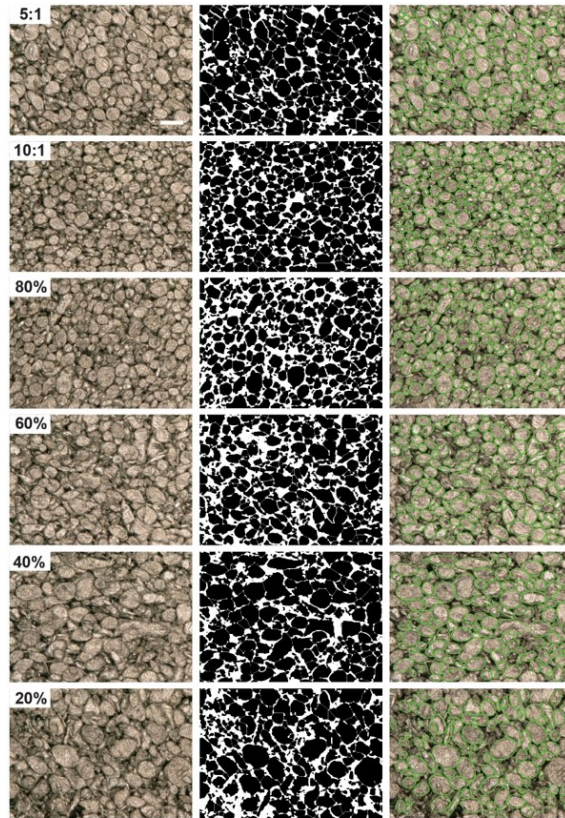


Figure 7.8: Particle analysis of LM-elastomer composite for  $\phi = 50\%$  and two oligomer/curing agent ratios (5:1, 10:1;  $\alpha = 100\%$ ) and four different blends of Sylgard 184 and Sylgard 527 ( $\alpha = 80, 60, 40, 20\%$ ). Column 1, optical micrographs of the composites. The scale bar is  $100 \mu\text{m}$ . Column 2, Thresholded image. Column 3, Ellipses fit to the particles in the thresholded image overlaid on the optical micrographs. The size of the analyzed area is  $800 \times 600 \mu\text{m}^2$  and particles having area  $< 500 \mu\text{m}^2$  are excluded.

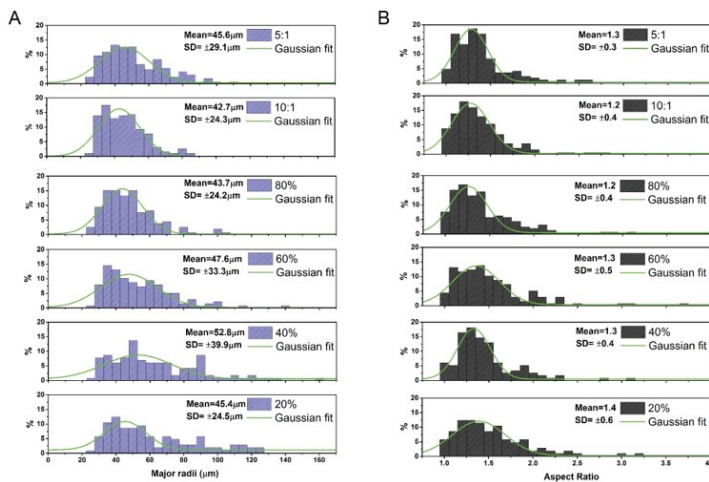


Figure 7.9: Particle analysis histograms. (A) Histogram of the percent of analyzed particles versus major radii with  $\alpha$  ranging from 100 to 20% (B) Histogram of the percent of analyzed particles versus the aspect ratio of the particles. Included is the Gaussian fit of the data with mean and standard deviation. The size of the analyzed area is  $800 \times 600 \mu\text{m}^2$ .

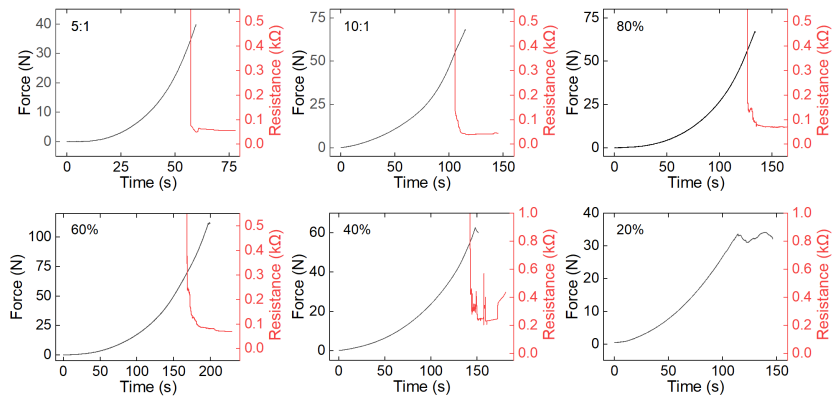


Figure 7.10: Applied compressive (black) and resistance between adjacent traces (red) as a function of time. The softer elastomer blends do not form a percolating network before elastomer failure ( $\alpha = 20\%$ ) or intermittently form an unstable network directly before elastomer failure ( $\alpha = 40\%$ ).

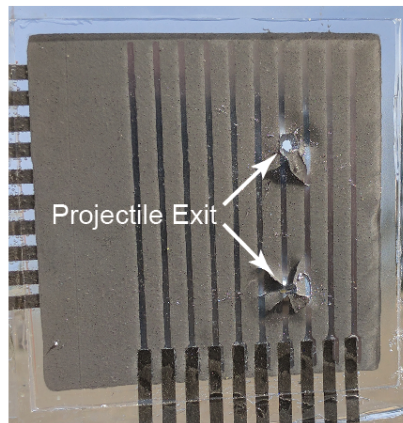


Figure 7.11: Photograph of the projectile exit.

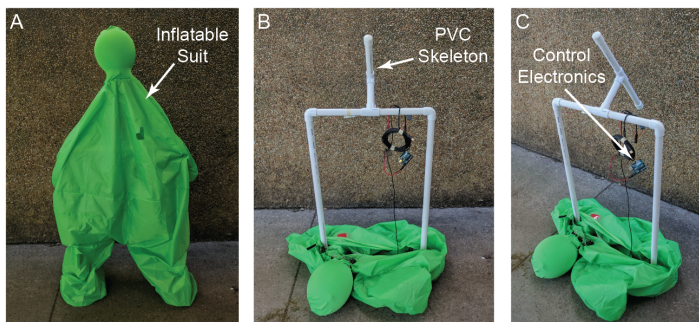


Figure 7.12: Soft robot mimic construction. (A) Completely deflated soft robot mimic. (B) Front view of plastic skeleton to support the inflatable suit. (C) Isometric view of plastic skeleton, control electronics, and battery.

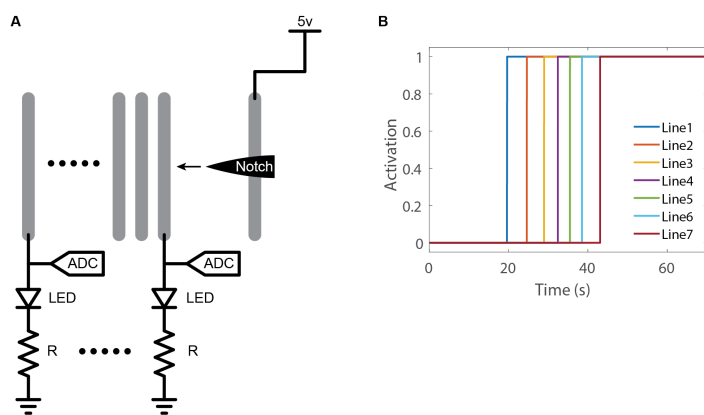


Figure 7.13: Damage detection and localization in 1D. (A) Schematic of detection scheme as a notch propagates through the sample. The notch causes a change in conductivity, completing the LED circuit. (B) Representative activation signals.